REPORT DOCUMENTATION PAGE

Form Approved
OMB No. 0704-0188

Public reporting burden for this collection of information is estimated to average 1 hour per response, including the time for reviewing instructions, searching existing data sources, gathering and maintaining the data needed, and completing and reviewing the collection of information. Send comments regarding this burden estimate or any other aspect of this collection of information, including suggestions for reducing this burden to Washington Headquarters Services, Directorate for Information Operations and Reports, 1215 Jefferson Davis Highway, Suite 1204, Arlington, VA 22202-4302, and to the Office of Management and Budget, Paperwork Reduction Project (0704-0188), Washington, DC 20503.

1. AGENCY USE ONLY *(Leave blank)*	2. REPORT DATE	3. REPORT TYPE AND DATES COVERED
	23 February 1998	Final Technical Report (11/1/90-12/31/96)

4. TITLE AND SUBTITLE
Structural Properties of Ferroelectric Perovskites

5. FUNDING NUMBERS
G:N00014-91-J-1184
PR: fmod 003

6. AUTHOR(S)
David Vanderbilt

7. PERFORMING ORGANIZATION NAMES(S) AND ADDRESS(ES)
Rutgers, The State University of New Jersey
Office of Research and Sponsored Programs
ASB Annex II
PO Box 1179
Piscataway, NJ 08855-1179

8. PERFORMING ORGANIZATION REPORT NUMBER

9. SPONSORING / MONITORING AGENCY NAMES(S) AND ADDRESS(ES)
Office of Naval Research
Ballston Centre Tower One
800 N. Quincy Street
Arlington, VA 22217-5660

10. SPONSORING / MONITORING AGENCY REPORT NUMBER

11. SUPPLEMENTARY NOTES

a. DISTRIBUTION / AVAILABILITY STATEMENT
Approved for Public Release

19980225 046

13. ABSTRACT *(Maximum 200 words)*

Under this research grant, we carried out realistic first-principles computer calculations of the ground-state and finite-temperature structural and dielectric properties of cubic perovskite materials such as $BaTiO_3$, $SrTiO_3$, $KNbO_3$, and $PbTiO_3$. These materials display an intriguing variety of ferroelectric, and antiferroelectric, and antiferrodistortive structural phase transitions, and are of particular interest for technological applications in view of their unique dielectric and piezoelectric properties and their widespread use in Navy acoustic transucer (sonar) systems. During the contract period, we succeeded in developing a detailed microscopic understanding of the structural and dielectric properties of many of these materials. In particular, we calculated the structural properties and identified the instabilities for eight materials; we developed a new approach to calculating electric polarization, and used it to compute spontaneous polarizations and dynamical effective charges; we calculated the phase transition sequence for $BaTiO_3$ and $SrTiO_3$ as a function of temperature; we studied the ground-state structure and phonons carefully for $PbTiO_3$; and we carried out studies of domain walls and surfaces in $BaTiO_3$.

14. SUBJECT TERMS
Ferroelectrics; structural Phase Transitions; First-Principles Calculations

15. NUMBER OF PAGES
7

16. PRICE CODE

17. SECURITY CLASSIFICATION OF REPORT	18. SECURITY CLASSIFICATION OF THIS PAGE	19. SECURITY CLASSIFICATION OF ABSTRACT	20. LIMITATION OF ABSTRACT
Unclassified	Unclassified	Unclassified	UL

DTIC QUALITY INSPECTED 4

Standard Form 298 (Rev. 2-89)
Prescribed by ANISE Sad Z39-18
298-102

Final Report on ONR Grant N00014-91-J-1184

This is a final technical report on ONR Grant N00014-91-J-1184, which provided funding for the project "Structural Properties of Ferroelectric Perovskites" from 11/1/90 to 12/31/96. The work was carried out at Rutgers University under the direction of the PI, Prof. David Vanderbilt.

Scientific Background

The goal of this work was to carry out realistic first-principles computer calculations of the ground-state and finite-temperature structural and dielectric properties of cubic perovskite materials such as $BaTiO_3$, $SrTiO_3$, $KNbO_3$, and $PbTiO_3$. These materials display an intriguing variety of ferroelectric (FE), and antiferroelectric (AFE), and antiferrodistortive (AFD) structural phase transitions, and are of particular interest for technological applications because of the existence or proximity of ferroelectric phases at lower temperatures. These give rise to unique dielectric and piezoelectric properties that are responsible for the widespread use of these materials in Navy acoustic transucer (sonar) systems. During the contract period, we succeeded in developing a detailed microscopic understanding of the structural and electrical properties of several of the most widely studied of these materials, as detailed below.

The structural phase transitions in the cubic perovskites are highly chemically specific. That is, materials with an identical high-temperature (cubic perovskite) crystal structure can have quite different low-temperature distorted phases, even for isoelectronic compounds like $BaTiO_3$ and $SrTiO_3$(which go cubic $\rightarrow$ tetragonal FE $\rightarrow$ orthorhombic FE $\rightarrow$ rhombohedral FE, and cubic $\rightarrow$ tetragonal AFD, respectively). Thus, an atomistic first-principles theoretical approach is required that is sufficiently accurate to predict such variations in behavior and to obtain reliable information about dielectric, elastic, piezoelectric, and electro-optic properties.

When we began this project, early work by Cohen and Krakauer[1]and others had already demonstrated that first-principles calculations based on Kohn-Sham density-functional theory in the local-density approximation (LDA),[2] could be used to formulate an accurate, predictive theory of these materials. Typically, these calculations have been carried out either within the linear-augmented-plane-wave (LAPW) or the plane-wave pseudopotential scheme. We chose to use a variant of the plane-wave pseudopotential approach involving so-called ultra-soft pseudopotentials[3−5] that are expecially well suited

1

to efficient calculations of properties This method provided us with a powerful and flexible tool for exploring the structural and dielectric properties of the perovskite materials.

Initial work on structural properties

Our initial work[6] focused on $BaTiO_3$. First, we checked that the calculated lattice constant $a=3.95$Å agrees well with experiment ($a=4.00$Å) and previous theoretical work[1] ($a=3.94$Å). The ferroelectric properties of $BaTiO_3$ were then examined by computing the total energy of the crystal as the ions were subject to displacements with tetrahedral and rhombohedral symmetry. We found the the energy of the crystal could be lowered by both types of distortion, confirming that our theoretical method captures the essential physics of the ferroelectric instability. We compared our theoretical atomic displacements of the low symmetry phases with the experimentally determined structures and we found excellent overall agreement.[6,7]

We next completed a battery of calculations on a set of eight perovskites comprising $SrTiO_3$, $CaTiO_3$, $KNbO_3$, $NaNbO_3$, $PbTiO_3$, $PbZrO_3$ and $BaZrO_3$ as well as $BaTiO_3$.[8] For each material, we analyzed the adiabatic energy surface of the five-atom primitive unit cell, when subjected to various distortions (frozen phonons and strains) consistent with periodic boundary conditions. For each compound, the dynamical matrix for the zone-center optical modes was determined from a series of frozen-phonon calculations. The eigenvector associated with the smallest eigenvalue of this dynamical matrix was used to identify the FE soft mode in each case. We found that the cubic structure was unstable toward the FE soft mode for all of the compounds except $BaZrO_3$. Next, we calculated the leading-order (quartic) anharmonic terms in the expansion of the energy in terms of the soft mode coordinates **u**. The sign of the anisotropy in these quartic terms determines whether the tetragonal or rhombohedral distortion is preferred at zero temperature in the absence of strain coupling. The coupling to strain was taken into account by carrying out systematic first-principles calculations of all of the elastic constants and Gruneisen parameters needed to determine strain-renormalized anharmonic coefficients. The renormalizations are sizable, and in the cases of $CaTiO_3$ and $PbTiO_3$, we find that the preferred distortion actually changes from orthorhombic to tetragonal when the strain coupling is included.

Theory of electric polarization in crystalline insulators

We made a fundamental advance in the theoretical understanding of electric polarization effects in solids.[9] In particular, we found a new expression for the change in electric

polarization of a solid which occurs when the solid is subjected to a finite perturbation, e.g., a displacement of the atoms. The new expression depends only on the valence band wavefunctions of the initial and final configurations of the crystal, and thus leads to a new and efficient method for calculating polarization effects. As a first application, the formulation was successfully applied to compute the Born effective charges and the piezo-electric tensor of GaAs;[9] the results were found to agree with previous work based on the considerably more complicated linear-response approach. We also explained how this approach can be used to formulate a new *definition* of the electric polarization in solids, and how this polarization is related to the electrostatic charge which accumulates at an insulating surface.[10] Our new formulation has been elaborated[11] and is now in routine use by many groups, including our own, for calculation of spontaneous polarizations and effective charges.

Anomalous Born effective charges and their effects

Using the above approach, we carried out a systematic series of first-principles calculations of Born effective charges Z^* and their effect on the optical phonon modes in $BaTiO_3$, $SrTiO_3$, $CaTiO_3$, $KNbO_3$, $NaNbO_3$, $PbTiO_3$, $PbZrO_3$ and $BaZrO_3$.[12] We found that anomalously large Z^*'s are a *general feature* of perovskite compounds. Our calculated optical phonon frequencies at the Γ point for both TO and LO modes are in good agreement with experiment. The eigenvector analysis reveals that in general, there is no simple correspondence between individual TO and LO modes. However, the softest TO mode usually involves the largest mode effective charge and can couple strongly with the electric field, thus giving an unexpected *giant LO-TO splitting*. The strong coupling to the electric field can easily destroy the ferroelectric state. We found that the calculated critical depolarization factor is only ≈ 0.1. This helps explain the remarkable sensitivity of ferroelectric state to domain structure and boundary conditions.

Phase transitions in BaTiO₃

We carried out a first-principles based study of the ferroelectric phase transitions in $BaTiO_3$.[13] In particular, we (i) constructed an effective Hamiltonian to describe the important degrees of freedom of the system, (ii) determined all the parameters of this effective Hamiltonian from high-accuracy *ab-initio* LDA calculations, and (iii) carried out classical Monte Carlo simulations to determine the phase transformation behavior of the resulting system. We found the *correct succession* of phases, with transition temperatures

3

and spontaneous polarization in reasonable agreement with experiment. All transitions were found (correctly) to be of first order, and estimates of the latent heat were obtained. Strain coupling was found to be crucial in producing the correct succession of low-symmetry phases. By analyzing the local distortions and phonon softening, we found the cubic-tetragonal transition in $BaTiO_3$ to be intermediate between the displacive and order-disorder limits.

Phase transitions in $SrTiO_3$

We applied a similar approach to study the competition between ferroelectric (FE) and antiferrodistortive (AFD) instabilities in compounds such as $SrTiO_3$.[16] In this case, we added to the effective Hamiltonian an additional set of degrees of freedom to represent the zone-boundary (octahedron rotation) modes associated with the AFD phases, fixing the coefficients in the Hamiltonian from LDA supercell calculations. We then carried out classical Monte Carlo simulations to determine the phase transformation behavior of the resulting system. We found that in this and many related cubic perovskites, the FE and AFD instabilities have a tendency to suppress one another, and have an opposite dependence on pressure. The Monte Carlo simulations thus show complicated behavior as a function of pressure and temperature for $SrTiO_3$. We found the transition from cubic to the tetragonal-AFD phase to occur at a temperature close to the experimental one, but we also found a transition to FE phases at very low temperature, where experimentally only a mysterious "quantum paraelectric" behavior is observed.

Effect of quantum fluctuations on phase transitions

Motivated largely by questions about the low-temperature phase behavior of $SrTiO_3$, we extended the study of the phase transitions in $SrTiO_3$ and $BaTiO_3$ by considering quantum (zero-point) fluctuations of the atom positions.[17] Normally such quantum effects are thought to be unimportant except for very light-atom systems (e.g., H, He) but we have shown that the smallness of the amplitude of the distortion associated with the FE or AFD phase is responsible for a sizeable quantum effect. In order to include the quantum effects in our Monte Carlo simulations, we made use of the path-integral Monte Carlo approach. We found that the quantum effects lower the transition temperatures of the FE modes in $BaTiO_3$ and of the AFD modes in $SrTiO_3$ by 15-30 K, and *eliminate entirely* the low-temperature FE phases in $SrTiO_3$. This slightly worsens the quantitative agreement of the transition temperatures in $BaTiO_3$ but gives excellent agreement with experiment

for $SrTiO_3$. Our results are consistent with a picture in which the magnitude of the FE fluctuations increases continuously with diminishing temperature, and becomes very large at $T = 0$, but we see no signs of a true phase transition at 37K as suggested by some authors.

Tight-binding study of Born effective charges

We have made a systematic study of the dynamic effective charges in compound semiconductors using our polarization approach[9] in the context of tight-binding theory.[18] We calculate the transverse effective charges of zincblende compound semiconductors using Harrison's tight-binding model to describe the electronic structure. Our results, which are essentially exact within the model, are found to be in much better agreement with experiment than previous perturbation-theory estimates.

Search for low-temperature instability in $PbTiO_3$

A first-principles study of the vibrational modes of $PbTiO_3$ in the ferroelectric tetragonal phase was performed at all the main symmetry points of the Brillouin zone.[19] The calculations reproduce well the available experimental information on the modes at the Γ point, including the LO-TO splittings. The work was motivated in part by a previously reported transition to an orthorhombic phase at low temperatures.[20] We showed that a linear coupling of orthorhombic strain to one of the modes at Γ plays a role in the discussion of the possibility of this phase transition. However, no mechanical instabilities (soft modes) are found, either at Γ or at any of the other high-symmetry points of the BZ.

Study of 180° domain walls in $BaTiO_3$

We carried out a study of the structure and energy of 180° FE domain walls in the tetragonal (room-temperature) phase of $BaTiO_3$,[21] using the effective Hamiltonian developed previously by us.[15] We found the domain wall to be atomically sharp, with the FE order parameter reversing (as opposed to rotating) as the domain wall is crossed. We calculated the average domain wall width, energy, and free energy. Previous theoretical and experimental estimates of these quantities were widely varying, and we believe our results give the most reliable values obtained to date.

Structural phase transitions in $CaTiO_3$ and $NaNbO_3$

We have applied our approach (first-principles calculations followed by classical Monte Carlo simulations on a fitted effective Hamiltonian) to study phase transitions in $CaTiO_3$ and $NaNbO_3$. Like $SrTiO_3$, these are compounds in which there is a competition between FE and AFD instabilities. However, these compounds are found to have rather complicated low-temperature structures, and the agreement between theory and experiment is less satisfying than for $SrTiO_3$.[22]

$BaTiO_3$ (100) surfaces

We carried out calculations of the structural properties of $BaTiO_3$ surfaces.[23] We considered the case of the (100) BaO- and TiO_2-terminated surfaces of tetragonal $BaTiO_3$ (with the ferroelectric order parameter lying parallel to the surface). We obtained the relaxed surface structure, including a determination of the influence of the surface on the ferroelectricity. We found only a weak enhancement of the ferroelectricity near the surface. The surface electronic structure was also studied; no deep gap states were found, but a valence-band derived state was found to protrude into the lower part of the band gap on the TiO_2-terminated surface.

Polarization effects in AlN/GaN interfaces

In collaboration with the group of V. Fiorentini (Cagliari, Italy) we carried out a study of the effects of polarization effects for polar AlN/GaN semiconductor interfaces. In this system, the lattice mismatch between AlN and GaN gives rise, through the piezoelectric effect, to polarizations that must be separated out in order to define and compute the band offsets. In a related study, we also computed the polarization directly for strained III-V nitrides via the Berry-phase method, and thereby carried out a systematic study of the dynamical effective charges and piezoelectric constants of these wide-gap semiconductors.

REFERENCES

[1] R.E. Cohen and H. Krakauer, Phys. Rev. B **42**, 6416 (1990).

[2] W. Kohn and L. J. Sham, Phys. Rev. **140**, A1133 (1965).

[3] D. Vanderbilt, Phys. Rev. B **41**, 7892 (1990).

[4] K. Laasonen, R. Car, C. Lee, and D. Vanderbilt, Phys. Rev. B **43**, 6796 (1991).

[5] K. Laasonen, A. Pasquarello, C. Lee, R. Car, and D. Vanderbilt, Phys. Rev. B **47**, 10142 (1993).

[6] R. D. King-Smith and D. Vanderbilt, Ferroelectrics **136**, 85 (1992).

[7] A.W. Hewat, Ferroelectrics **6**, 215 (1974).

[8] R.D. King-Smith and D. Vanderbilt, Phys. Rev. B **49**, 5828 (1994).

[9] R.D. King-Smith and D. Vanderbilt, Phys. Rev. B **47**, 1651 (1993).

[10] D. Vanderbilt and R.D. King-Smith, Phys. Rev. B **48**, 4442 (1993).

[11] R. Resta, Rev. Mod. Phys. **66**, 899 (1994).

[12] W. Zhong, R.D. King-Smith, and D. Vanderbilt, Phys. Rev. Lett. **72**, 3618 (1994).

[13] W. Zhong, D. Vanderbilt, and K.M. Rabe, Phys. Rev. Lett. **73**, 1861 (1994).

[14] W. Zhong, D. Vanderbilt, R.D. King-Smith, and K. Rabe, Ferroelectrics **164**, 291 (1995).

[15] W. Zhong, D. Vanderbilt, and K.M. Rabe, Phys. Rev. B **52**, 6301 (1995).

[16] W. Zhong and D. Vanderbilt, Phys. Rev. Lett. **74**, 2587 (1995).

[17] W. Zhong and D. Vanderbilt, Phys. Rev. B **53**, 5047 (1996).

[18] J. Bennetto and D. Vanderbilt, Phys. Rev. B. **53**, 15417 (1996).

[19] A. García and D. Vanderbilt, Phys. Rev. B **54**, 3817 (1996).

[20] J. Kobayashi, Y. Uesu, and Y. Sakemi, Phys. Rev. B **28**, 3866 (1983).

[21] J. Padilla, W. Zhong, and D. Vanderbilt, Phys. Rev. B **53**, R5969 (1996).

[22] W. Zhong and D. Vanderbilt, Ferroelectrics, in press.

[23] J. Padilla, W. Zhong, and D. Vanderbilt, Phys. Rev. B **56**, 1625 (1997).

Attachments

Reprints of the more important of the published papers supported by this research grant are provided as attachments, as follows:

Attachment 1: Ref. 8.
Attachment 2: Ref. 9.
Attachment 3: Ref. 12.
Attachment 4: Ref. 13.
Attachment 5: Ref. 15.
Attachment 6: Ref. 16.
Attachment 7: Ref. 17.
Attachment 8: Ref. 19.
Attachment 9: Ref. 21.
Attachment 10: Ref. 23.

First-principles investigation of ferroelectricity in perovskite compounds

R. D. King-Smith* and David Vanderbilt

Department of Physics and Astronomy, Rutgers University, Piscataway, New Jersey 08855-0849
(Received 16 August 1993)

We have used a first-principles ultra-soft-pseudopotential method in conjunction with an efficient preconditioned conjugate-gradient scheme to investigate the properties of a series of eight cubic perovskite compounds. The materials considered in this study are $BaTiO_3$, $SrTiO_3$, $CaTiO_3$, $KNbO_3$, $NaNbO_3$, $PbTiO_3$, $PbZrO_3$, and $BaZrO_3$. We computed the total-energy surface for zone-center distortions correct to fourth order in the soft-mode displacement, including renormalizations due to strain coupling. Quantities calculated for each material include lattice constants, elastic constants, zone-center phonon frequencies, Grüneisen parameters, and band structures. Our calculations correctly predict the symmetry of the ground-state structures of all compounds whose observed low-temperature structure retains a primitive five-atom unit cell. The database of results we have generated shows a number of trends which can be understood using simple chemical ideas based on the sizes of ions, and the frustration inherent in the cubic perovskite structure.

I. INTRODUCTION

The perovskites are an extremely important class of ferroelectric materials.[1] Generically these compounds have a chemical formula ABO_3 where A is a monovalent or divalent cation and B is a penta- or tetravalent metal. The perfect perovskite structure is very simple and has full cubic symmetry. It can be thought of as a lattice of corner sharing oxygen octahedra with interpenetrating simple cubic lattices of A and B cations. The B cations sit at the center of each oxygen octahedra while the A metal ions lie in 12-fold coordinated sites between the octahedra. The fascinating feature of the perovskite structure is the extreme ease with which it will undergo structural phase transitions; experimentally the perovskites exhibit a diverse range of phases including transitions to both ferroelectric and antiferroelectric states as well as structural transitions to states involving tilting of the oxygen octahedra.

In spite of the fact that the perovskites have been the subject of intense investigation since the discovery of ferroelectricity in barium titanate in the 1940s, there is still no complete understanding of the nature of the transitions in these materials. For example, given the chemical formula of a perovskite material, there are no reliable methods for predicting transition temperatures, whether a transition is first or second order, or even which phonons in the material will be responsible for transitions. In principle these quantities can be obtained by calculating the partition function given the ion-ion Hamiltonian of the crystal.[1] It is well established that both harmonic and anharmonic phonon-phonon couplings as well as phonon-strain couplings are essential ingredients for a description of the transitions observed in the perovskites. However, there is little quantitative knowledge about the interaction parameters of this Hamiltonian and an accurate determination of these variables is a challenging theoretical problem.

First-principles density functional calculations offer an attractive approach for enhancing our microscopic understanding of perovskites and other ferroelectrics. One of the earliest successes of this method was due to Rabe and Joannopoulos who combined conventional pseudopotential methods with renormalization-group theory to calculate the transition temperature of the narrow-band semiconductor GeTe.[2]

More recently there has been a flurry of activity to apply these methods to perovskite compounds. Cohen and Krakauer[3] used the all-electron full-potential linearized augmented-plane-wave (FLAPW) method to study ferroelectricity in $BaTiO_3$ within the local density approximation (LDA). They performed a series of frozen phonon calculations and demonstrated that the phase with full cubic symmetry is unstable with respect to zone-center distortions, in accord with the experimentally observed ferroelectric transition in this material. They went on to study the depth and shapes of the energy well with respect to soft-mode displacement, and to demonstrate that strain strongly influences the form of the total-energy surface. Later they extended this approach to the case of $PbTiO_3$.[4] Using experimental data as a guide they were able to show that the observed tetragonal ferroelectric ground state of this material is stabilized by the large strain which appears upon transition from the cubic structure. Cohen emphasized that the hybridization between the titanium $3d$ and oxygen $2p$ is necessary for ferroelectricity in $BaTiO_3$ and $PbTiO_3$.[5] Singh and Boyer have also used the FLAPW method to investigate ferroelectricity in $KNbO_3$.[6] They found that the cubic structure was stable at the theoretical lattice constant, at variance with experimental observations, although their calculations did show weak ferroelectric behavior when they set the lattice constant to the experimental value. The FLAPW studies have demonstrated that ferroelectricity in the perovskites reflects a delicate balance between long-range electrostatic forces which favor the ferroelectric state and short-range repulsions which favor the cubic phase. Thus it has been demonstrated that

high-quality LDA calculations can shed considerable insight into the nature of the total-energy surface in the perovskites. However, the work also raises a note of caution about the validity of the LDA. For example the work of Singh and Boyer[6] suggests that $KNbO_3$ is not a ferroelectric in this approximation.

Recently we have applied the ultrasoft-pseudopotential method to investigate ferroelectricity in $BaTiO_3$.[7] Pseudopotential methods offer a number of advantages over all-electron methods. They are computationally more efficient than methods such as the FLAPW, and moreover allow one to compute forces on the ions analytically. Methods which provide information on Hellmann-Feynman forces allow the adiabatic energy surface to be explored with many fewer calculations than techniques which only compute total energies. However, the use of a pseudopotential does introduce further approximations beyond the LDA, associated with neglect of the core states and other transferability issues. The results of our calculation on $BaTiO_3$,[7] which included Ba and Ti semicore states, were in substantial agreement with the work of Cohen and Krakauer. We thus demonstrated that this approach can attain the level of accuracy necessary to capture the physics of the of ferroelectricity in the perovskites.

In the present paper we have chosen to apply the ultrasoft-pseudopotential approach to a series of eight perovskites, thus greatly increasing the amount of first-principles data available on these materials. Again, we include semicore states in the valence shell for all metals considered. The compounds selected for study were $BaTiO_3$, $SrTiO_3$, $CaTiO_3$, $KNbO_3$, $NaNbO_3$, $PbTiO_3$, $PbZrO_3$, and $BaZrO_3$. The properties of these materials are reviewed in Refs. 1 and 8. Experimentally all of these compounds are observed to have the perfect cubic perovskite structure at sufficiently high temperatures. Three of these materials, $BaTiO_3$, $KNbO_3$, and $PbTiO_3$, are observed to have ferroelectric ground states with five atoms in the primitive cell. Both $BaTiO_3$ and $KNbO_3$ are observed to undergo the same sequence of transitions as a function of temperature from the perfect cubic perovskite structure, to a tetragonal phase, to an orthorhombic phase before becoming rhombohedral at the lowest temperatures. By way of contrast $PbTiO_3$ has a single well-established transition from the cubic to the tetragonal phase at 493 °C. $SrTiO_3$ is an incipient ferroelectric which undergoes a nonferroelectric oxygen tilting transition at about 105 K. $CaTiO_3$ undergoes a single transition from the cubic state to an orthorhombic phase with 20 atoms in the unit cell at about 1260 °C. $NaNbO_3$ shows at least six transitions as a function of temperature. Its ground state is a monoclinic ferroelectric phase with four formula units per unit cell. $PbZrO_3$ is an antiferroelectric compound with eight formula units per unit cell. The transition from the cubic phase occurs at about 230 °C. Finally $BaZrO_3$ is the simplest material considered here and is believed to have the perfect cubic perovskite structure at all temperatures.

Our approach has been to focus exclusively on the possible zone-center instabilities of these materials. This restriction has a number of important practical advantages.

First, as will be demonstrated in the following sections, the number of degrees of freedom of the system in this case is small enough to allow us to perform a completely systematic expansion of the energy to fourth order in the soft-mode displacement vector, without the need for experimental input which might bias our results. Second, this simplification allows us to focus on trends in the total-energy surface with composition even when the experimental situation may be much more complicated. For example it is clear from the previous discussion that the experimental behavior of each compound in the $BaTiO_3$, $SrTiO_3$, $CaTiO_3$ series is quite different. By concentrating on the relatively small number of parameters associated with zone-center distortions we might hope to begin to unravel the origins of these differences in these chemically similar materials. Finally, by choosing to work with the smallest possible cells we can afford to use very high-quality k-point sets for the Brillouin zone integrations. In the following it will be demonstrated that it is important to ensure that calculations are exceptionally well converged in this respect when studying ferroelectricity in the perovskites.

The remainder of this paper is set out as follows. In Sec. II we develop our systematic expansion of the soft-mode total-energy surface about the cubic perovskite structure. Section III describes some of the technical aspects of our work and discusses the convergence of our calculations. We present the results of our calculations in Sec. IV, and comment on some of the implications of the results in Sec. V. We review the main conclusions of this study in Sec. VI. Appendix A contains some of the more formal parts of the derivation of the energy expansion about the cubic perovskite structure. Appendix B describes our conjugate-gradient technique for minimizing the Kohn-Sham energy functional. Unless otherwise stated all results in the following sections are quoted in atomic units (i.e., lengths in bohrs and energies in hartrees).

II. FORMALISM

In order to carry out our investigation of the total-energy surfaces of the eight compounds in question it will be useful to develop a systematic expansion for the energy about the cubic perovskite structure. Our goal is to compute the minimum energy of configuration of the ions in the structure. It is well known that strain degrees of freedom play a significant role in determining the energies of the low-symmetry ferroelectric phases and should therefore be included in the analysis.[1,3,4] As stated in the Introduction we shall exclude from consideration any distortions which change the number of atoms in the unit cell. At first sight our task of performing a systematic exploration of the energy surface poses a formidable challenge, because even if we only include zone-center distortions and strains we are still faced with examining the properties of an 18-dimensional energy space.[4] However, we shall show that a manageable scheme for carrying through this program can be developed provided we restrict ourselves to computing the energy correct to fourth order in the soft-mode displacement. The high symme-

try of the cubic perovskite structure greatly reduces the number of calculations which are required. Our expansion of the energy is similar in spirit to that of Pytte,[9] although it differs in some details.

Formally the energy of the crystal is function of the six independent components of the strain tensor η_i, where i is a Voigt index ($\eta_1 = e_{11}, \eta_4 = 2e_{23}$), and the 15 displacement variables v_α^τ, where τ is an atom label and α is a Cartesian direction. Thus we may write the energy per unit cell as

$$E = E(\{\eta_i\}, \{v_\alpha^\tau\}). \tag{1}$$

In the following we shall make extensive use of the fact that

$$E(\{\eta_i\}, \{v_\alpha^\tau\}) = E(\{\eta_i\}, \{-v_\alpha^\tau\}). \tag{2}$$

Equation (2) follows by virtue of the fact that each atom in the perovskite structure sits at a center of inversion upon application of an arbitrary homogeneous strain. Formally it will be helpful to divide the energy function into parts arising from pure displacement, pure strain, and an interaction term as

$$E = E^0 + E^{\text{disp}}(\{v_\alpha^\tau\}) + E^{\text{elas}}(\{\eta_i\}) + E^{\text{int}}(\{\eta_i\}, \{v_\alpha^\tau\}), \tag{3}$$

where E^0 is the energy of the perfect perovskite structure. $E^{\text{disp}}(\{v_\alpha^\tau\})$ and $E^{\text{elas}}(\{\eta_i\})$ give a description of the energy to all orders at zero strain and zero displacement respectively. In crystals with cubic symmetry the strain energy is given, correct to second order in the strains, by

$$\begin{aligned} E^{\text{elas}}(\{\eta_i\}) = &\frac{1}{2}B_{11}(\eta_1^2 + \eta_2^2 + \eta_3^2) \\ &+ B_{12}(\eta_1\eta_2 + \eta_2\eta_3 + \eta_3\eta_1) \\ &+ \frac{1}{2}B_{44}(\eta_4^2 + \eta_5^2 + \eta_6^2), \end{aligned} \tag{4}$$

where B_{11}, B_{12}, and B_{44} are related by factors of the cell volume to the elastic constants of the crystal.

We begin by considering in detail the expansion of $E^{\text{disp}}(\{v_\alpha^\tau\})$. Straightforward Taylor expansion of the energy implies that the lowest-order term can be written as $\frac{1}{2}\sum_{\tau,\tau',\alpha,\beta} D_{\alpha,\beta}^{\tau,\tau'} v_\alpha^\tau v_\beta^{\tau'}$ where $D_{\alpha,\beta}^{\tau,\tau'} = \left. \frac{\partial^2 E}{\partial v_\alpha^\tau \partial v_\beta^{\tau'}} \right|_0$.

The second derivative matrix $D_{\alpha,\beta}^{\tau,\tau'}$ is of course related to the zone-center dynamical matrix by trivial factors of the ionic masses. The symmetry properties of $D_{\alpha,\beta}^{\tau,\tau'}$ have already been discussed in the context of first-principles calculations.[3,6] In the following we shall adopt a coordinate system such that the atoms in our general perovskite with formula ABO_3 in the perfect structure have positions A at $(0,0,0)a$, B at $(\frac{1}{2},\frac{1}{2},\frac{1}{2})a$, O_I at $(0,\frac{1}{2},\frac{1}{2})a$, O_{II} at $(\frac{1}{2},0,\frac{1}{2})a$, and O_{III} at $(\frac{1}{2},\frac{1}{2},0)a$, where a is the lattice constant. The first point to note is that all elements of $D_{\alpha,\beta}^{\tau,\tau'}$ for which $\alpha \neq \beta$ are zero (it is intuitive that displacement of any of the five sublattices in, say, the x direction will produce no forces in the y or z direction). The 15×15 second derivative matrix therefore breaks into a set of

three independent and identical 5×5 blocks, each corresponding to displacements in the x, y, or z direction. As a consequence the eigenvalues of the second derivate matrix fall into five sets of threefold degenerate modes. In the following we will denote the eigenvalues of $D_{\alpha,\beta}^{\tau,\tau'}$ as $\lambda(j)$ where j is an index which runs from 1 to 5. Thus we may write

$$\sum_{\beta\tau'} D_{\alpha,\beta}^{\tau,\tau'} \xi_\beta^{\tau'}(j,\gamma) = \lambda(j)\xi_\alpha^\tau(j,\gamma). \tag{5}$$

Moreover, it is clear from the foregoing discussion that the eigenvectors, $\xi_\alpha^\tau(j,\beta)$, of the second derivative matrix can be chosen to lie entirely along x, y, or z and can thus be labeled by j and the Cartesian direction β. With this convention we will have $\xi_\alpha^\tau(j,\beta) = 0$ if $\alpha \neq \beta$. Two of the eigenvectors of each 5×5 block are determined by symmetry. The first mode is the trivial translation mode with eigenvalue 0. The second mode has Γ_{25} symmetry.[6] The eigenvector of this mode for displacements in the z direction has the form $(0,0,\frac{1}{\sqrt{2}},-\frac{1}{\sqrt{2}},0)$ where the displacement vector is listed in the order $(v_z^A, v_z^B, v_z^{O_I}, v_z^{O_{II}}, v_z^{O_{III}})$. The remaining three modes of each block have Γ_{15} symmetry and their eigenvectors cannot be deduced on symmetry grounds alone. Experimentally it is these modes with Γ_{15} symmetry which are responsible for ferroelectric transitions from the high-symmetry cubic phase. In a material such as barium titanate where the experimental ground state is a five-atom unit cell with rhombohedral symmetry one expects at least one of the three Γ_{15} eigenvalues to have a negative sign, indicating that the cubic structure is a saddle point of the total-energy surface. In the following the lowest-frequency mode with Γ_{15} symmetry will be referred to as the *soft mode*.

We can reexpress E^{disp}, correct to second order, in terms of the diagonalized $D_{\alpha,\beta}^{\tau,\tau'}$ matrix as

$$E^{\text{disp}} = \frac{1}{2}\sum_j \lambda(j)\sum_\alpha u_\alpha^j u_\alpha^j, \tag{6a}$$

where u_α^j are eigenmode amplitudes given by

$$u_\alpha^j = \sum_\tau \xi_\alpha^\tau(j,\alpha)v_\alpha^\tau. \tag{6b}$$

Because of their special role in the following it will be convenient to introduce a simplified notation to describe the soft-mode distortions. If j_{soft} is the index of the soft mode, then we define

$$\kappa = \frac{1}{2}\lambda(j_{\text{soft}}), \tag{7a}$$

and will suppress the j superscript for the soft-mode amplitude so that

$$u_\alpha = u_\alpha^{j_{\text{soft}}}. \tag{7b}$$

Having decoupled the soft-mode degrees of freedom to second order in the displacements we now consider the effects of higher-order terms in the soft-mode expansion of the energy. We introduce $\Phi(\{u_\alpha\})$ which is E^{disp} with all

non-soft-mode eigenmode amplitudes held at zero. There can be no third-order terms in the displacement which contribute to $\Phi(\{u_\alpha\})$ by virtue of Eq. (2). Two independent parameters are required to describe the fourth-order terms and we find

$$\Phi(\{u_\alpha\}) = \kappa u^2 + \frac{1}{24} B_{xxxx} \sum_\alpha u_\alpha^4$$
$$+ \frac{1}{4} B_{xxyy}(u_x^2 u_y^2 + u_y^2 u_z^2 + u_z^2 u_x^2), \qquad (8a)$$

where

$$B_{xxxx} = \left.\frac{\partial^4 E}{\partial u_x^4}\right|_0, \qquad (8b)$$

$$B_{xxyy} = \left.\frac{\partial^4 E}{\partial u_x^2 \partial u_y^2}\right|_0, \qquad (8c)$$

and $u^2 = \sum_\alpha u_\alpha^2$. It will simplify the notation if we introduce two new parameters α and γ defined by

$$\alpha = \frac{1}{24} B_{xxxx} \qquad (9a)$$

and

$$\gamma = \frac{1}{12}(3 B_{xxyy} - B_{xxxx}). \qquad (9b)$$

Substituting into Eq. (8a) we obtain

$$\Phi(\{u_\alpha\}) = \kappa u^2 + \alpha u^4 + \gamma(u_x^2 u_y^2 + u_y^2 u_z^2 + u_z^2 u_x^2). \qquad (10)$$

The constant γ gives a measure of the anisotropy of the total-energy surface. In the following we shall be primarily concerned with the case where there are zone-center instabilities so that $\kappa < 0$. Under these circumstances it can be shown that Φ has four distinct types of stationary points. The first of these is the trivial case where $u_x = u_y = u_z = 0$, with $\Phi = 0$. This is always a maximum of Φ when $\kappa < 0$ indicating that the crystal is unstable in the cubic perovskite structure. There are six symmetry-equivalent stationary points of the second type. They lie along the $\langle 100 \rangle$ directions and have positions such as

$$u_x = u_y = 0, \quad u_z = \sqrt{-\frac{\kappa}{2\alpha}}, \qquad (11a)$$

with energy

$$\Phi = -\frac{\kappa^2}{4\alpha}. \qquad (11b)$$

The third set of stationary points, of which there are 12, falls in the $\langle 110 \rangle$ directions and has coordinates of the type

$$u_x = 0, \quad u_y = u_z = \sqrt{-\frac{\kappa}{4\alpha + \gamma}}, \qquad (12a)$$

with energy

$$\Phi = -\frac{\kappa^2}{4(\alpha + \frac{1}{4}\gamma)}. \qquad (12b)$$

Finally there are eight equivalent stationary points in the $\langle 111 \rangle$ directions with positions such as

$$u_x = u_y = u_z = \sqrt{-\frac{\kappa}{6\alpha + 2\gamma}}, \qquad (13a)$$

with energy

$$\Phi = -\frac{\kappa^2}{4(\alpha + \frac{1}{3}\gamma)}. \qquad (13b)$$

Necessary conditions for the above fourth-order analysis to be valid are that $\alpha > 0$ and $\gamma > -3\alpha$. Otherwise the energy has unphysical divergences to $-\infty$ implying that higher-order terms must be taken into account. Provided the fourth-order analysis is valid, two distinct ground states can arise depending on the sign of γ. If $\gamma > 0$, then Eq. (11b) is a global minimum and the crystal ground state has tetragonal symmetry. If $\gamma < 0$, then the global minima are along the $\langle 111 \rangle$ directions and the ground state has rhombohedral symmetry with energy given in Eq. (13b).

Finally we must consider how the above picture is modified when we permit possible extra relaxations of the system through coupling of the soft modes to other phonons and the strains. The basic strategy is to compute the values of η_i and u_α^j which minimize the total energy as a function of the soft-mode variables. Following the notation of Ref. 10 we denote these minimizing values with $\tilde{\eta}_i(\{u_\alpha\})$ and $\tilde{u}_\alpha^j(\{u_\alpha\})$ and the corresponding energy with $\tilde{E}(\{u_\alpha\})$. By straightforward differentiation of Eq. (3) it can be shown that the only term which leads to renormalization of the soft-mode surface, in the fourth-order theory, is the lowest-order term in E^{int}.[11] This term can be written in the form $\frac{1}{2} \sum_{i\alpha\beta} B_{i\alpha\beta}\eta_i u_\alpha u_\beta$, in an obvious notation. To second order in u_α, $\tilde{\eta}_i$ is given by the solution to the matrix equation

$$\sum_j B_{ij}\tilde{\eta}_i + \frac{1}{2}\sum_{\alpha\beta} B_{i\alpha\beta} u_\alpha u_\beta = 0. \qquad (14)$$

There are three different types of nonzero elements in the $6 \times 3 \times 3$ matrix $B_{i\alpha\beta}$. Typical nonzero elements are B_{1xx}, B_{1yy}, and B_{4yz}. The renormalized energy is given by

$$\tilde{E}(\{u_\alpha\}) = E^0 + \Phi(\{u_\alpha\})$$
$$- \frac{1}{8}\sum_{ij}\sum_{\alpha\beta\gamma\delta} u_\alpha u_\beta B_{i\alpha\beta} N_{ij} B_{j\gamma\delta} u_\gamma u_\delta, \qquad (15)$$

where $N_{ij} = \left[B^{-1}\right]_{ij}$. The solution of Eq. (14) to obtain $\tilde{E}(\{u_\alpha\})$ in Eq. (15) is somewhat tedious, and is therefore deferred to Appendix A. It is shown there that

$$\widetilde{E}(\{u_\alpha\}) = E^0 + \Phi(\{u_\alpha\}) - \frac{1}{24}\left(\frac{C^2}{B} + 4\frac{\nu_t^2}{\mu_t}\right)\sum_\alpha u_\alpha^4 - \frac{1}{12}\left(\frac{C^2}{B} - 2\frac{\nu_t^2}{\mu_t} + 6\frac{\nu_r^2}{\mu_r}\right)(u_x^2 u_y^2 + u_y^2 u_z^2 + u_z^2 u_x^2), \quad (16)$$

where B is the bulk modulus,

$$B = B_{11} + 2B_{12}, \quad (17a)$$

μ_t and μ_r are shear moduli for tetragonal and rhombohedral distortions,

$$\mu_t = \frac{1}{2}(B_{11} - B_{12}), \quad (17b)$$

$$\mu_r = B_{44}, \quad (17c)$$

and C, ν_t, and ν_r are analogously defined quantities obtained from the strain-phonon coupling constants,

$$C = B_{1xx} + 2B_{1yy}, \quad (17d)$$

$$\nu_t = \frac{1}{2}(B_{1xx} - B_{1yy}), \quad (17e)$$

$$\nu_r = B_{4yz}. \quad (17f)$$

Comparing Eq. (16) with Eq. (8a) we arrive at the reassuring conclusion that the fourth-order corrections to the minimum energy $\widetilde{E}(\{u_\alpha\})$ arising from soft-mode coupling to the strain have exactly the same structure as the original "bare" fourth-order terms. The net effect of switching on the coupling between the phonon and strain degrees of freedom can be thought of as a renormalization of the bare fourth-order interaction coefficients B_{xxxx} and B_{xxyy} to B'_{xxxx} and B'_{xxyy} defined by

$$B'_{xxxx} = B_{xxxx} - \left(\frac{C^2}{B} + 4\frac{\nu_t^2}{\mu_t}\right) \quad (18a)$$

and

$$B'_{xxyy} = B_{xxyy} - \frac{1}{3}\left(\frac{C^2}{B} - 2\frac{\nu_t^2}{\mu_t} + 6\frac{\nu_r^2}{\mu_r}\right). \quad (18b)$$

We therefore conclude that our analysis of the stationary properties of the total-energy surface can equally well be applied to the case where phonon-strain couplings are present, provided we work with renormalized coupling constants α' and γ' where

$$\alpha' = \alpha - \frac{1}{24}\left(\frac{C^2}{B} + 4\frac{\nu_t^2}{\mu_t}\right) \quad (19a)$$

and

$$\gamma' = \gamma + \frac{1}{2}\left(\frac{\nu_t^2}{\mu_t} - \frac{\nu_r^2}{\mu_r}\right). \quad (19b)$$

Our final expression for $\widetilde{E}(\{u_\alpha\})$ is simply

$$\widetilde{E}(\{u_\alpha\}) = E^0 + \kappa u^2 + \alpha' u^4 + \gamma'(u_x^2 u_y^2 + u_y^2 u_z^2 + u_z^2 u_x^2). \quad (20)$$

In the case where $\kappa < 0$ there are two possible ground states in the complete fourth-order theory. If $\gamma' < 0$, we would predict that a phase with rhombohedral symmetry has the lowest energy, where as $\gamma' > 0$ implies that the ground state is tetragonal. In the following section our objectives are to use high-quality first-principles calculations to obtain the various expansion parameters necessary to determine the constants in Eq. (20).

In conclusion we have shown that the minimum total energy as a function of soft-mode displacement can be determined correct to fourth order in u_α in terms of nine independent interaction parameters κ, B_{11}, B_{12}, B_{44}, B_{1xx}, B_{1yy}, B_{4yz}, B_{xxxx}, and B_{xxyy}. We have found that in practice these quantities can be computed using about 40 self-consistent calculations per material. The major formal results are that coupling of the soft mode to the strain renormalizes the minimum energy surface in our fourth-order approximation, whereas coupling to other phonons does not. The quadratic coefficient in the total energy, κ, is unrenormalized by either phonon or strain interactions.

III. TECHNICAL DETAILS OF CALCULATIONS

The first-principles calculations presented in this paper were performed using the Vanderbilt ultrasoft-pseudopotential scheme.[12] Technical details of this method and its implementation in solid-state calculations have already been discussed elsewhere.[7,13–16] A feature of the present work is the use of a conjugate-gradient technique for minimizing the Kohn-Sham energy functional, as described in Appendix B.

The ultrasoft-pseudopotential approach has two major advantages. First, it allows us to work with a modest plane-wave cutoff, despite the presense of both first-row atoms and first-row transition metal atoms, which are generally difficult cases for pseudopotential methods.[17] This is accomplished at the expense of introducing a generalized eigenvalue equation containing an overlap operator, and generalizing the usual definition of the valence charge density to include an augmentation step. The ultrasoft potentials are a little more complicated than the original Kleinman-Bylander separable potentials.[18] However, the computational costs associated with the extra steps in the calculations only add a small fraction to the time required per conjugate-gradient iteration.

Second, it allows for the generation of exceptionally transferable pseudopotentials, because of its use of multiple reference energies during the construction procedure.[12] In essence the scheme allows one to insist that the all-electron and pseudologarithmic derivatives agree at two or three energies, instead of at just one energy.[19] This ensures that the all-electron and pseudoatom scattering properties agree over an exceptionally wide energy range. Moreover, it allows us to treat ex-

TABLE I.   Transferability of the titanium pseudopotential. All-electron $3s$, $3p$, $4s$, and $3d$ eigenvalues are given in hartrees; Δ is the corresponding difference between the all-electron eigenvalue and pseudoeigenvalue, in mhartree. $\Delta = 0$ in the reference $3s^2 3p^6 4s^2 3d^1$ configuration by construction.

Configuration	$3s$	$\Delta(3s)$	$3p$	$\Delta(3p)$	$4s$	$\Delta(4s)$	$3d$	$\Delta(3d)$
$3s^2 3p^6 4s^2 3d^2$	-2.288023	-0.2	-1.425332	-0.3	-0.169049	0.0	-0.164012	0.2
$3s^2 3p^6 4s^2 3d^1$	-2.765159	0.0	-1.893377	0.0	-0.445220	0.0	-0.592621	0.0
$3s^2 3p^6 4s^2 3d^0$	-3.359884	0.5	-2.475773	0.3	-0.783472	0.0	-1.139811	-1.1
$3s^2 3p^6 4s^1 3d^1$	-3.104766	0.1	-2.231605	0.1	-0.707960	0.0	-0.921973	0.0
$3s^2 3p^6 4s^0 3d^0$	-4.175466	0.0	-3.285763	0.2	-1.359890	0.6	-1.930327	0.3
$3s^2 3p^5 4s^2 3d^1$	-3.396932	-1.8	-2.511765	-2.1	-0.790393	0.1	-1.169291	0.2

plicitly the "shallow" core states in the calculation by including multiple sets of occupied states in each angular momentum channel. This helps to improve the chemical hardness of the potential.[20] Moreover, there is evidence that explicit treatment of the semicore levels is necessary to correctly describe the phonon instabilities of perovskites and related materials.[21]

Semicore shells have been included in the present calculation for all the metals considered. Specifically, we include as valence states the $2s$ and $2p$ states of Na; the $3s$ and $3p$ states of K, Ca, and Ti; the $4s$ and $4p$ states of Sr, Zr, and Nb; and the $5s$ and $5p$ states of Ba. We also include the $5d$ shell in Pb. Thus, we have been much more conservative about our choice of what constitutes a valence state than is generally the case in the pseudopotential method.[22] This is motivated by the need for high accuracy when studying the ferroelectric instabilities in perovskites.

Other details are as follows. Relativity was included by first performing scalar relativistic calculations on all-electron atoms,[23] and then applying a suitable generalization of the pseudization procedure proposed by Kleinman.[24] The oxygen potential used two construction energies each in the s and p channels. The potentials for the metals in this study all employed two reference energies per angular momentum in s, p, and d channels. The pseudo-wave-functions were constructed using the optimized potential method proposed by Rappe et al.,[17] by minimizing the kinetic energy of the pseudo-wave-

function above the plane-wave cutoff, which we chose to be 25 Ry throughout our calculations. A variant of the same scheme was also applied to generate pseudo-charge-augmentation functions. In this case the cutoff for the optimization step was chosen to be 100 Ry, because the cutoff energy for the potentials and densities in plane-wave methods is generally 4 times as large as that for the wave functions.

Our tests suggest that the potentials in this study are of very high quality. We shall consider in more detail the case of Ti, which is probably the least transferable of the ten pseudopotentials required for this study. There are two main tests of pseudopotential transferability in common use. The first involves checking that the logarithmic derivatives of the all-electron and pseudoatom agree over a reasonable range of energies. In a previous publication we showed that our titanium potential does an exceptional job of matching the all-electron logarithmic derivatives over a 4 hartree range of energy.[7] The second main test is to check that the all-electron atoms and pseudoatoms have similar eigenvalues when the ionization state of the atom is changed. In Table I we summarize the results of our tests on the titanium potential. The atom was generated in the $3s^2 3p^6 4s^2 3d^1$ configuration and so Δ, the difference between the all-electron eigenvalues and pseudoeigenvalues in mhartree, is zero by construction for all states in this case. The largest values of Δ of -2.1 mhartree occur when an electron is removed from the $3p$ level. However, given the depth of

TABLE II.   Convergence of eigenvalues and eigenvectors of $D_{\alpha\beta}^{\tau\tau'}$ with k-point set in PbTiO₃. The lower eigenvalues, which are a measure of potential soft-mode instability, are remarkably sensitive to the k-point sampling; this may be indicative of delicate cancellations between competing contributions to the force constants. Subsequent calculations use the $(6,6,6)$ mesh.

k points	Eigenvalues			Eigenvectors		
2 2 2	-0.00918	-0.8679	0.0246	0.3244	0.3244	0.1885
	0.15538	-0.0620	0.5993	0.1207	0.1207	-0.7795
	0.16851	-0.2119	0.6631	-0.4236	-0.4236	0.3955
4 4 4	-0.01824	-0.6400	-0.4376	0.4062	0.4062	0.2622
	0.05070	-0.6145	0.7801	-0.0285	-0.0285	-0.1096
	0.15338	-0.1168	0.0003	-0.3655	-0.3655	0.8479
6 6 6	-0.02584	-0.5729	-0.5146	0.4074	0.4074	0.2732
	0.04422	-0.6765	0.7312	0.0144	0.0144	-0.0843
	0.15250	-0.1183	0.0027	-0.3657	-0.3657	0.8476
8 8 8	-0.02720	-0.5644	-0.5237	0.4066	0.4066	0.2765
	0.04350	-0.6830	0.7250	0.0210	0.0210	-0.0826
	0.15264	-0.1187	0.0059	-0.3665	-0.3665	0.8468

TABLE III. Convergence of eigenvalues and eigenvectors of $D_{\alpha\beta}^{\tau\tau'}$ with energy cutoff in $PbTiO_3$. Results appear to be well converged at 25 Ry, which is used as the cutoff for subsequent calculations.

Cutoff (Ry)	Eigenvalues	Eigenvectors				
25	-0.02584	-0.5729	-0.5146	0.4074	0.4074	0.2732
	0.04422	-0.6765	0.7312	0.0144	0.0144	-0.0843
	0.15250	-0.1183	0.0027	-0.3657	-0.3657	0.8476
50	-0.02400	-0.5961	-0.4888	0.4087	0.4087	0.2674
	0.04493	-0.6576	0.7489	-0.0055	-0.0055	-0.0804
	0.15565	-0.1099	-0.0106	-0.3645	-0.3645	0.8497

this state it is extremely unlikely that it could be depleted by anything approaching a single electron in the ground state of a real solid. The more important data are therefore the rows connected with removal of the valence $4s$ and $3d$ electrons. Typically the values of Δ are less than 0.5 mhartree in this case. Overall the agreement between all-electron eigenvalues and pseudoeigenvalues appears to be comparable with that achieved by Teter's recent extended-norm and hardness-conserving (ENHC) potentials, which represent the state of the art in this respect in more conventional pseudopotential technology.[20]

The solid-state calculations throughout this work were performed using a (6,6,6) Monkhorst-Pack mesh,[25] i.e., 6^3 points in the full Brillouin zone. The unit cells used here had either cubic, tetragonal, or rhombohedral symmetry, which yielded 10, 18, and 28 k points in the irreducible wedge of the zone respectively. This represents a k-point set of quite exceptional quality given that the materials in question are all insulators. However, our tests indicate that this level of accuracy is necessary when computing the properties of the soft-mode total-energy surface. For example Table II shows how the Γ_{15} symmetry eigenvalues and eigenvectors of the $D_{\alpha\beta}^{\tau\tau'}$ matrix converge as a function of k-point set quality in $PbTiO_3$. The second derivative matrix was constructed using a frozen phonon approach. The soft-mode eigenvalues $\lambda(j_{soft}) = 2\kappa$, computed with the (4,4,4) and (6,6,6) Monkhorst-Pack mesh, differ by about 30%. The analysis of the previous section shows that the well depths depend on κ^2. We would therefore conclude that well depths computed with the (4,4,4) and (6,6,6) Brillouin zone meshes would disagree by 50% if the anharmonic terms were unaffected. This unusual sensitivity may be indicative of delicate cancellations between competing contributions to the restoring forces for soft-mode distortions.

A plane-wave cutoff of 25 Ry was used throughout our calculations, consistent with the optimization value used in our construction procedure. We have also tested the convergence of the Γ_{15} eigenvalues and eigenvectors of the $D_{\alpha\beta}^{\tau\tau'}$ matrix with respect to energy cutoff. Results are summarized in Table III. We find that κ changed by about 7% on increasing the cutoff from 25 to 50 Ry. The higher-frequency $\lambda(j)$ are converged to about 2% at 25 Ry. It would therefore appear that the error due to incomplete convergence of the basis set is of similar size to the k-point sampling error. The exchange and correlation was calculated using the Ceperley-Alder form.[26]

We conclude that our calculations are fairly well con-

verged with respect to k-point sets and plane-wave cutoff, although there is room for improvement in these areas. It should be borne in mind that many previous studies on the perovskite compounds have used the (4,4,4) rather than (6,6,6) Monkhorst-Pack meshes.[3–6] We think that this is potentially a significant source of error, particularly when it comes to computing the depths of the ferroelectric wells.

IV. RESULTS

A. Lattice constants of the perovskites

We computed the value of the lattice constant which minimizes the energy of the structure when the ions are held fixed in the perfect cubic perovskite structure. Our results, in atomic units, are summarized in Table IV. The values obtained are in excellent accord with those calculated with the FLAPW method, in those cases where calculations exist. The first-principles results are generally $1-2\%$ smaller than the experimental values. This magnitude and sign of error are typical of high-quality total-energy calculations, which tend to underestimate lattice constants as a consequence of the LDA. For comparison we have also computed values of the lattice constant using Shannon-Prewitt radii.[27] We consider the possibility that the lattice constant is determined either by interaction of the 12-fold coordinated A cation and oxygen (A-O), or by interaction of the 6-fold coordinated B cation and oxygen (B-O). The ionic radius approach clearly tends to overestimate the lattice constant. In their original paper Shannon and Prewitt[27] noted that their method tends to perform relatively poorly for perovskites and other high-symmetry structures. Nevertheless, many of the trends observable in Table IV can be understood in terms of this simple picture. For example both the theoretical and experimental lattice constants are seen to decrease with decreasing radius of the A cation in the $BaTiO_3$, $SrTiO_3$, $CaTiO_3$ series. In a similar way we also find that the lattice constant increases on replacing Ti with the larger Zr ion in both $BaTiO_3$ and $PbTiO_3$.

In the final column of Table IV we introduce a quantity, δ, which is a length that measures the extent of the frustration between the competing (A-O) and (B-O) interactions in the cubic perovskite lattice. We define δ to be the difference between the cubic lattice constants predicted by the Shannon-Prewitt radii assuming that (A-O) and (B-O) interactions are dominant. Thus a value of δ close to zero, as found in $BaZrO_3$ or $SrTiO_3$, im-

TABLE IV.   Cubic perovskite lattice constants in bohrs.

Compound	This work	FLAPW	Experiment	(A-O)	(B-O)	δ
$BaTiO_3$	7.456	7.45[a]	7.58	8.02	7.58	0.44
$SrTiO_3$	7.303		7.38	7.59	7.58	-0.01
$CaTiO_3$	7.192		7.25	7.35	7.58	-0.23
$KNbO_3$	7.472	7.488[b]	7.58	8.02	7.71	0.31
$NaNbO_3$	7.396		7.44	?[e]	7.71	?[e]
$PbTiO_3$	7.350	7.35[c]	7.50	7.72	7.58	0.14
$PbZrO_3$	7.770		7.81[d]	7.72	8.01	-0.29
$BaZrO_3$	7.853		7.924	8.02	8.01	0.01

[a] Ref. 3.

[b] Ref. 6.

[c] R.E. Cohen (private communication).

[d] Calculated assuming the same density as the tetragonal phase.

[e] Value not calculated as tables do not include value for 12-fold coordinated Na^+.

plies that both A and B cations are simultaneously satisfied by their oxygen environment. The sign convention adopted here is such that a positive value of δ, as that found in $BaTiO_3$, implies that the hole for the B cation is stretched beyond its ideal value. In the following we shall explore the extent to which trends in the behavior of the perovskite compounds can be correlated with δ. The importance of competing $(A$-$O)$ and $(B$-$O)$ interactions in the perovskites has been emphasized previously and can be traced at least as far back as Slater's work on $BaTiO_3$.[28]

B. Zero-temperature structures of the perovskites in the LDA

Having obtained the lattice constant which minimizes the energy of the perfect cubic perovskite structure for each material, we went on to compute the soft-mode eigenvalues κ and eigenvectors introduced in Sec. II, using the frozen phonon method. Three calculations with different displacement patterns are sufficient to obtain the modes with Γ_{15} symmetry.   We used displacements in the z direction of the form $(0.002,0,0,0,0)a$, $(0,0.002,0,0,0)a$, and $(0,0,0.001,0.001,-0.002)a$, where the displacement vector is listed in the order $(v_z^A, v_z^B, v_z^{O_I}, v_z^{O_{II}}, v_z^{O_{III}})$. Our results for κ are summarized in column 8 of Table V.

There are a number of interesting observations to be made about the values of κ obtained in this way. First, we find that κ is positive only for $BaZrO_3$. This result

for $BaZrO_3$ is in accord with the experimental observation that this material is stable in the cubic perovskite structure at all temperatures. We would also expect the three compounds $BaTiO_3$, $KNbO_3$ and $PbTiO_3$, which have ferroelectric ground states with primitive five-atom unit cells, to have negative values of κ. This expectation is confirmed in Table V and Table VI where we summarize which compounds are theoretically ferroelectric, if we restrict attention to just the zone-center instabilities. Previous studies on $BaTiO_3$ (Refs. 3 and 7) and $PbTiO_3$ (Ref. 4) have found zone-center instabilities at the theoretical lattice constant. However, the previous LDA study on $KNbO_3$,[6] using the FLAPW method, found this material to be stable at the theoretical lattice constant, although there was a very small ferroelectric instability when the lattice was strained to the experimental value. This discrepancy is discussed further at the end of this subsection.

The remaining compounds in this study exhibit transitions in which phonons become soft at points other than Γ in the Brillouin zone. Experimental observations therefore do not preclude the possibility that there may be an unstable Γ point phonon; another transition may simply intervene before the Γ point instability has a chance to freeze in. For example, $SrTiO_3$ is an incipient ferroelectric and by extrapolating the high-temperature form for the dielectric response one would predict a transition to a ferroelectric ground state at 40 K.[1] At atmospheric pressure, however, $SrTiO_3$ makes a transition to a structure with tilted oxygen octahedra at 110 K.

TABLE V.   Interaction parameters of eight perovskites in a.u.

	B_{11}	B_{12}	B_{44}	B_{1xx}	B_{1yy}	B_{4yz}	κ	α	γ	α'	γ'
$BaTiO_3$	4.64	1.65	1.84	-2.18	-0.20	-0.08	-0.0175	0.320	-0.473	0.176	-0.124
$SrTiO_3$	5.14	1.38	1.56	-1.41	0.06	-0.11	-0.0009	0.150	-0.191	0.093	-0.010
$CaTiO_3$	5.15	1.22	1.29	-0.59	0.06	-0.10	-0.0115	0.023	-0.006	0.013	0.061
$KNbO_3$	6.54	0.96	1.37	-3.01	0.33	-0.01	-0.0154	0.378	-0.613	0.184	-0.111
$NaNbO_3$	6.63	0.96	1.07	-1.71	0.50	0.00	-0.0124	0.168	-0.256	0.093	-0.041
$PbTiO_3$	4.52	1.97	1.36	-0.78	0.00	-0.03	-0.0129	0.044	-0.045	0.022	0.025
$PbZrO_3$	5.92	1.37	1.07	-0.22	0.07	-0.01	-0.0156	0.011	-0.013	0.009	-0.003
$BaZrO_3$	5.52	1.56	1.47	-0.47	0.07	-0.11	0.0078	0.016	0.000	0.009	0.054

TABLE VI. Summary of the theoretical and experimental ground-state structures of the eight perovskites. Abbreviations are ferroelectric (FE), antiferroelectric (AF), antiferrodistortive (AFD), rhombohedral (R), tetragonal (T), monoclinic (M), cubic (C), and orthorhombic (O).

	Theory	Expt. (primitive)	Expt. (complex)
$BaTiO_3$	FE-R	FE-R	
$SrTiO_3$	FE-R		AFD-T
$CaTiO_3$	FE-T		O
$KNbO_3$	FE-R	FE-R	
$NaNbO_3$	FE-R		FE-M
$PbTiO_3$	FE-T	FE-T	
$PbZrO_3$	FE-R	FE-R[a]	AF-O
$BaZrO_3$	C	C	

[a] Extrapolated from the phase diagram of PZT.

A direct comparison between the theoretical and experimental soft-mode eigenvectors can be made for the cases of $BaTiO_3$, $KNbO_3$, and $PbTiO_3$, using the experimentally measured ionic displacements for the ferroelectric phase.[29-31] The results are summarized in Table VII. In all cases the soft-mode amplitude is underestimated by the fourth-order theory. Typically the error is about 30%. This size and sign of error is not surprising in view of the fact that our calculations underestimate the theoretical lattice constant, and that this and other studied[3,4,6,7] have shown that the soft-mode surface is a sensitive function of volume. For the case of $BaTiO_3$, our results for the soft-mode eigenvector are in good accord with the experimental data, a result we found in our previous work.[3,7] However, the level of agreement is less satisfactory for $KNbO_3$ and still worse for the case of $PbTiO_3$, which has the largest spontaneous distortion. We have tried relaxing the ions in $PbTiO_3$ at the experimental lattice constant and c/a ratio. The displacement vector obtained in this case is $(0.73, 0.32, -0.36, -0.36, -0.32)$, which is clearly in much better accord with the experimental data. The soft-mode amplitude was also brought in closer agreement with experiment, coming out to be 0.913 a.u. Thus, we conclude that for the compounds with the largest spontaneous distortion, the fourth-order

expansion should not be trusted to describe the energy surface with quantitative accuracy all the way to the distorted equilibrium structure.

The elastic constants for the eight perovskites were computed by examining the behavior of the total energy as a function of strain. Data generated in the previous section were used to compute the bulk modulus by fitting a third-order polynomial through the energy vs lattice constant data. A typical example of the quality of fit is shown in Fig. 1(a) where we show our results for the case of $PbTiO_3$. The two remaining independent elastic constants, which were taken to be B_{11} and B_{44}, were obtained by freezing in strains which lowered the symmetry of the cells to tetragonal or rhombohedral symmetry, and again fitting the energy vs strain curves with a third-order polynomial. At least five different values of the strain were employed to obtain each elastic constant in each material.

The elastic constants we have obtained for the perovskites appear to be in good agreement with previous theoretical results in the few places we have been able to make comparisons. Singh and Boyer[6] found a bulk modulus of 195 GPa in their FLAPW work on $KNbO_3$ which agrees to about 2% with the value of 199 GPa found here. Cohen,[32] also using the FLAPW method, obtained a bulk modulus of 215 GPa for $PbTiO_3$, which is about 3% larger than our value of 209 GPa. The best available experimental elastic constants on the cubic phases of the materials studied here appear to be for $SrTiO_3$.[8] The Landolt-Börnstein tables quote room temperature ranges of 316−348 GPa, 101−103 GPa, and 119−124 GPa for c_{11}, c_{12}, and c_{44}, respectively, which can be compared with our own values of 389 GPa, 105 GPa, and 155 GPa. Overall the level of agreement between theory and experiment is about 20%, which is not as good as one would generally expect from an LDA calculation. However, it must be borne in mind that the cubic phase of $SrTiO_3$ is unstable, and that the measured elastic constants are quite strong functions of temperature. For example according to the results of Bell and Rupprecht[33] c_{11} increases by about 4% as the temperature is lowered from room temperature to $-160\,°C$, before dropping precipitously as the transition temperature is approached. It is therefore unclear whether a direct comparison of the

TABLE VII. Comparison of theoretical and experimental soft-mode amplitudes and vectors. Amplitudes are in bohrs, and vectors are normalized to unity.

	$BaTiO_3$ Theory	$BaTiO_3$ Expt.[a]	$KNbO_3$ Theory	$KNbO_3$ Expt.[b]	$PbTiO_3$ Theory	$PbTiO_3$ Expt.[c]
$\xi_z^A(j_{soft}, z)$	0.20	0.22	0.18	0.32	0.57	0.72
$\xi_z^B(j_{soft}, z)$	0.76	0.76	0.80	0.73	0.51	0.33
$\xi_z^{O_I}(j_{soft}, z)$	-0.21	-0.23	-0.31	-0.33	-0.41	-0.35
$\xi_z^{O_{II}}(j_{soft}, z)$	-0.21	-0.23	-0.31	-0.33	-0.41	-0.35
$\xi_z^{O_{III}}(j_{soft}, z)$	-0.53	-0.52	-0.37	-0.38	-0.27	-0.35
Amplitude	0.25	0.31	0.22	0.37	0.54	0.82

[a] Ref. 29.

[b] Ref. 30.

[c] Ref. 31.

theoretical and experimental elastic constants for the cubic symmetry structure is valid and in view of these uncertainties we were satisfied with the level of agreement obtained.

The phonon strain interaction parameters B_{1xx}, B_{1yy}, and B_{4yz} were found by freezing in a small amount of the soft-mode vector (typically we used $u = 0.005a$) and
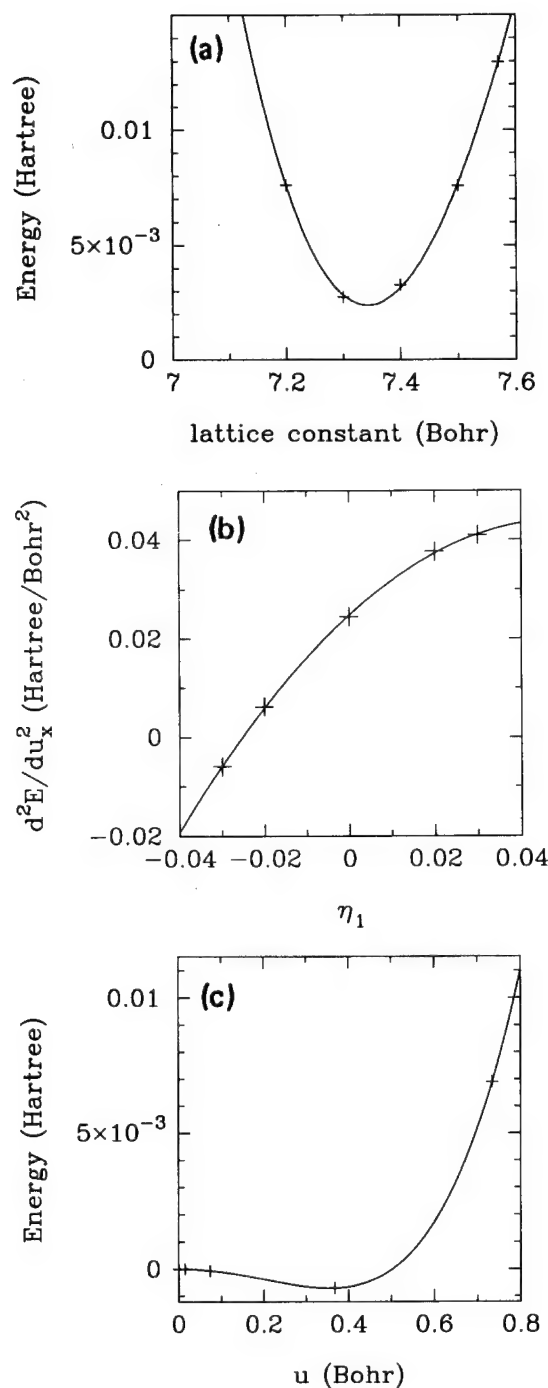

FIG. 1. Sample fits used to obtain interaction parameters of $PbTiO_3$. (a) shows fit of energy vs lattice constant. (b) depicts $\dfrac{\partial^2 E}{\partial u_x^2}$ as an η_1 strain is frozen into the cell. (c) shows the variation of the energy as the soft-mode amplitude is increased for the case $u_x = u$, $u_y = u_z = 0$.

computing the changes in the forces on the ions for five different strains. Results for our calculation of B_{1xx} in the case of $PbTiO_3$ are shown in Fig. 1(b). It is apparent from Table V that the most important strain-phonon coupling arises through the term B_{1xx} terms which tend to be large and are always negative. Physically B_{1xx} measures the extent to which the x-polarized soft-mode eigenvalue changes on application of an η_1 strain. The negative sign of this coupling constant is reasonable, because compression of the lattice in the x direction (application of a negative η_1) will tend to increase the ion-ion repulsions and hence raise the soft-mode eigenvalue. In Fig. 2 we plot B_{1xx} as a function of the soft-mode angle. It is apparent that B_{1xx} shows a marked tendency to become more negative as the soft-mode angle decreases. Given that a small soft-mode angle implies large motion of the B cation, this suggests that B_{1xx} is most sensitive to the B-O interactions in the cell, and that the B-O bond stiffens rapidly as it is compressed.

Finally α and γ were obtained by freezing in the soft-mode distortion for a range of values of u in the [100] and [111] directions and fitting the resulting energy vs displacement curves with a quadratic polynomial in the square of the soft-mode coordinate. Typical results for the case of $PbTiO_3$ are illustrated in Fig. 1(c). The resulting sets of parameters are summarized in Table V. The final two columns of this table give the values of α' and γ' as defined in Sec. II.

Perhaps the most successful aspect of Table V is that it correctly predicts the symmetry of the ground-state structures of all the compounds with primitive five-atom unit cells. For clarity we have summarized the theoretical and experimental results in Table VI. γ' is negative for $BaTiO_3$ and $KNbO_3$, and so these materials should have rhombohedral structures as their lowest-temperature structures according to our fourth-order theory. $PbTiO_3$, on the other hand, has a positive value of γ' and is thus correctly predicted to have a tetragonal ground state. A further interesting case is provided by $PbZrO_3$. While pure $PbZrO_3$ has a rather complicated
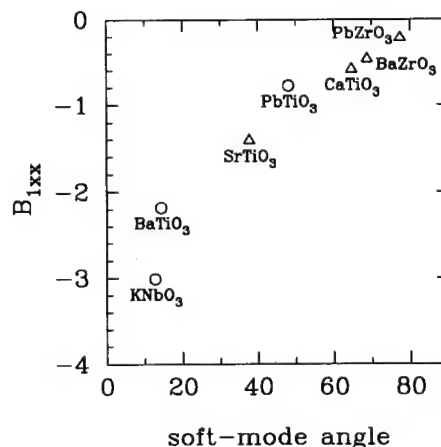

FIG. 2. Strain-phonon interaction parameter B_{1xx} in hartree/bohr^2 against soft-mode angle in degrees.

ground-state structure, it is found that the solid solution $PbTi_xZr_{1-x}O_3$ (PZT) has a simple ferroelectric structure in the range $0.1 < x < 1.0$. The ground-state structure undergoes a transition from a tetragonal to a rhombohedral phase at a composition of x about 0.5 as $PbZrO_3$ is added to $PbTiO_3$.[1] It is therefore also reasonable that γ' should be negative for $PbZrO_3$ as observed in Table V.

We return now to discuss the discrepancy between our results and those of Singh and Boyer.[6] As noted earlier, these authors found that $KNbO_3$ is stable in the cubic structure at the theoretical lattice constant, whereas the current work predicts $\kappa < 0$ and a rhombohedral ground-state structure. The origins of this discrepancy are unclear at this time. Part of the explanation may lie in the higher-quality k-point sets used here, as the trends observable in Table II suggest that incomplete convergence of the Brillouin zone integrations leads to an overestimate of κ. Our experience has been that the calculation of the soft-mode eigenvalue in a ferroelectric is a much more difficult calculation than the apparently similar problem of obtaining the phonon frequencies of a semiconductor such as Si. In the previous section it was demonstrated that this quantity is unusually sensitive to k-point sets and plane-wave cutoff. However, this probably does not account for the whole difference between our results, and we think it is too early to decide whether the present work or that of Singh and Boyer is closer to the "exact LDA" answer. On the one hand, we are clearly in closer agreement with experiment than the FLAPW calculations; on the other hand, it is to be admitted that the pseudopotential method makes an additional approximation over the FLAPW method. This uncertainty highlights the need for further high-quality calculations by other groups using independent codes and methods to more accurately quantify the size of the LDA errors in these materials.

C. Band structures

We have calculated the band structures for each perovskite. In each case we worked with the unit cell with full cubic symmetry at the theoretical lattice constant. Figure 3 shows our results for $PbTiO_3$. The energy scale is in eV, and the origin of energy was arbitrarily set to be at the valence band maximum. A visual comparison of our results for this material against those of Cohen
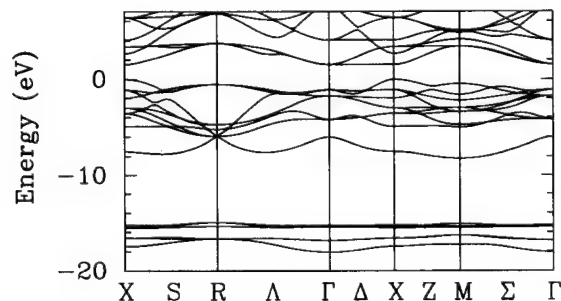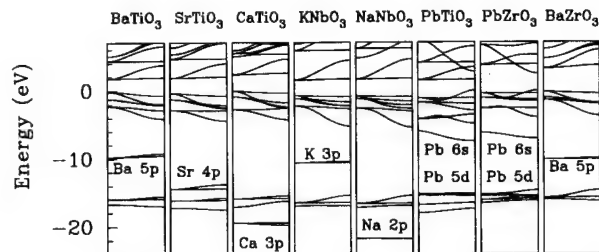
FIG. 4.   Comparison of the band structures of eight perovskite compounds in the cubic structure from Γ to X.

and Krakauer[4] shows almost no discernible difference. In Fig. 4 we show the results of our calculation for all eight materials between Γ and X. In each material there is a fairly narrow set of oxygen $2s$ bands between about -16.0 and -18.0 eV, and a group of oxygen $2p$ states between 0.0 and -5.0 eV. Also visible on this scale is a number of shallow core states associated with the A cation, which we have labeled individually in Fig. 4. It can be seen that these shallow core states have the most influence on the upper valence bands and lower conduction bands in the case of the lead compounds.

Our band-structure calculation for $SrTiO_3$ is also in good agreement with the LAPW calculation of Mattheiss;[34] the small differences that do occur presumably reflect the neglect of relativistic effects in the latter. Our calculations for all eight materials show the same characteristic flatness of certain bands (e.g., the lowest conduction band along Γ to X) as was found by Mattheiss for $SrTiO_3$ and several other cubic perovskites.[34] The fitting of the perovskite band structures to tight-binding models has been discussed by Mattheiss,[34] Harrison,[35] and Wolfram and Ellialtioğlu.[36] The latter authors relate the observed flatness of the bands to certain unusual features in the density of states and optical response which appear to be characteristic of two-dimensional systems.

D. Analysis of structural trends

Here, we discuss whether the results obtained above can be understood on the basis of simple models and chemical trends. As discussed in the previous subsection, it is clear that band-structure features are best discussed in the context of a tight-binding description.[34–36] Here, our emphasis is on structural energetics.

A number of trends in our soft-mode data can be understood in a qualitative way in terms of δ, the parameter introduced in Sec. IV A to reflect the frustration in the ionic radii. Intuitively we might expect that those materials with the values of δ which are closest to zero should be the most stable materials in the cubic perovskite phase and might therefore tend to have the largest values of soft-mode eigenvalue. In Fig. 5 we plot κ in a.u. against δ in a.u. In order to slightly increase the database of results we have also included in the plot values obtained for $SrZrO_3$ and $CaZrO_3$. There does appear to be some tendency for κ to peak around $\delta = 0$. The trend is perhaps most convincing if one focuses on groups of chem-

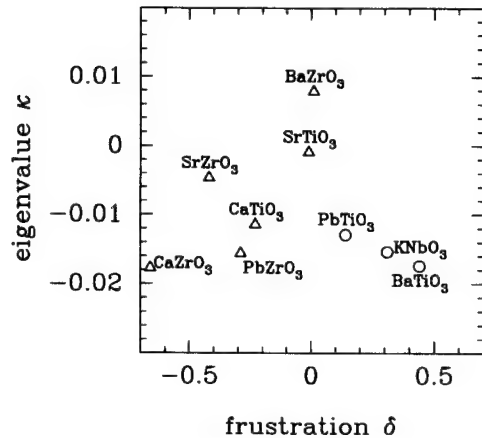FIG. 3.   Band structure of cubic $PbTiO_3$ for selected high-symmetry directions.

FIG. 5. Soft-mode eigenvalues (hartree/bohr^2) against frustration (bohrs) for nine perovskite compounds. Materials with primitive five-atom ferroelectric ground states are plotted as circles. All other cases are shown as triangles.

FIG. 6. Soft-mode angle in degrees vs frustration (bohrs). Symbols as in Fig. 5.

ically similar compounds, such as the BaZrO$_3$, SrZrO$_3$, CaZrO$_3$ series where κ decreases steadily as δ decreases from about 0.0 a.u. to about -0.7 a.u., or the BaTiO$_3$, SrTiO$_3$, CaTiO$_3$ series, which is peaked at SrTiO$_3$ with $\delta = -0.01$.

Interestingly, the three compounds with ferroelectric ground states with five atoms in the primitive cell (depicted with circles in Fig. 5) are the compounds with significantly positive values of δ. While we think that the above observations form a useful point of view for analyzing our data, it is important to point out that a simple analysis in terms of our frustration parameter δ has its limitations. For example the compound KTaO$_3$ has exactly the same value of δ as KNbO$_3$ according to the Shannon-Prewitt tables. However KTaO$_3$ is believed to be stable in the cubic perovskite structure at all temperatures.[1,8] Thus we have an example of a material with a substantial positive value of δ which is not ferroelectric and must have $\kappa > 0$.

We have also considered the behavior of the soft-mode eigenvector, $\xi_\alpha^\tau(j_{\text{soft}}, \alpha)$ as a function of δ. For positive δ the B ions are likely to be "loose" in their sockets because the A-O interactions expand the lattice beyond the ideal B-O value. It is reasonable to expect that the magnitude of $\xi_\alpha^B(j_s, \alpha)$ will be greater than $\xi_\alpha^A(j_s, \alpha)$ in these circumstances. The converse should hold true for the situation where $\delta < 0$. In Fig. 6 we have plotted the soft-mode angle defined as $\tan^{-1}\left[\xi_\alpha^A(j_s, \alpha)/\xi_\alpha^B(j_s, \alpha)\right]$ in degrees against δ in bohrs. The first point of note is that all the angles are positive, which implies that in all cases the A and B cations move in the same direction in the soft mode. As expected, there is a convincing trend for the A cation motion to decrease with increasing δ.

Of course, δ is a purely "classical" measure of ionic radius. However, the perovskites are only weakly ionic. For example, the hopping $V_{pd\sigma}$ between nearest-neighbor O $2p$ and Ti $3d$ orbitals is found to be on the same order as the energy separation between these levels, about 3 eV.[34] Thus it is clear that p-d hybridization must make
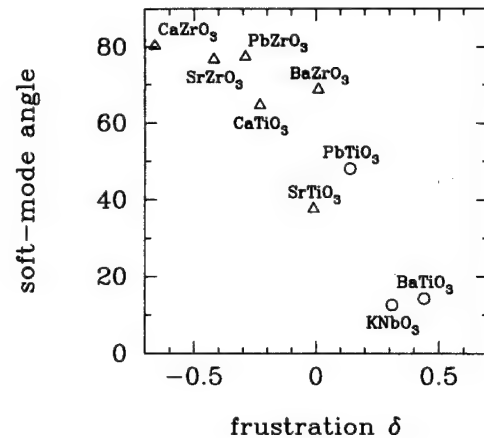
a contribution to the crystal cohesion and must play a role in the ferroelectric instabilities. One is therefore led to look for correlations of computed structural properties with chemical trends and isoelectronic relationships. However, such trends are not very evident in Table V. Focusing just on the elastic constants (the only quantities which do not involve the soft mode), one does see that the two compounds of the form I-Va-O$_3$ (NaNbO$_3$ and KNbO$_3$) have larger values of B_{11} and smaller values of B_{12} than the other six materials. This is most likely due to the difference in Madelung energies. However, a systematic dependence of computed quantities upon the species of the B cation, as might be expected from the role of the latter in hybridizing with the oxygen, is not evident. For example, while NaNbO$_3$ and KNbO$_3$ might be expected to behave similarly on chemical grounds, many of the quantities listed beyond the third column of Table V are quite different. This is because these quantities all depend indirectly upon the soft-mode eigenvector, which is quite different for the two materials (for which the soft-mode angle defined above is 36° and 13° respectively). Thus, despite the expected importance of p-d hybridization, it appears that simple arguments based on ionic radii are surprisingly effective.

V. DISCUSSION

Here, we comment briefly on some of the implications of our results.

We find that the sign of the effective fourth-order coupling is positive in all directions in all eight materials. (As can be seen from Sec. II, this effective fourth-order coupling ranges from α' to $\alpha' + \gamma'/3$, depending on direction; Table V shows that this quantity is always positive, even after renormalization by strain coupling is taken into account.) In the Landau-type theories of the ferroelectric phase transition, the sign of the fourth-order term in the order-parameter expansion of the free energy determines whether the transition is of first or second order.[1] Of course, at $T > 0$ the free energy is renormalized by anharmonic coupling of the soft-mode variable to

other phonons, which is not included in our calculations. Thus, at least for the compounds studied, we conclude that coupling to strain alone is insufficient to drive the fourth-order term negative as required for a first-order transition. In those cases where the transition is observed to be first order, the anharmonic phonon couplings must be responsible.

The bare coupling constant γ is almost always found to be negative in the materials studied here. The strain renormalizations were always found to increase the value of this quantity (i.e., $\gamma' > \gamma$), and in a couple of cases cause it to switch sign. These observations serve to highlight the important consequences of strain coupling in the perovskites, as emphasized previously by Cohen and Krakauer[4] in their study of $PbTiO_3$. Moreover, they provide a possible explanation for a well-known asymmetry in the observed sequences of phase transitions: namely, that those materials like $BaTiO_3$ which are rhombohedral at $T = 0$ typically pass through tetragonal and sometimes orthorhombic phases on the way from the cubic phase, while those materials such as $PbTiO_3$ which are tetragonal at $T = 0$ usually transform directly from the cubic phase. In the former case, the sequence of transitions is usually rationalized in terms of an eight-site model, in which the order parameter just above the transition to the cubic phase is assumed to spend most of its time fluctuating among the eight minima in the $\langle 111 \rangle$ directions. Just below the transition, it freezes onto a subset of four of these minima, with average $\langle 100 \rangle$ orientation and tetragonal symmetry; only at very low temperature does it freeze into a single minimum and acquire rhombohedral symmetry. This scenario requires that the sites along the $\langle 111 \rangle$ directions be minima even in the cubic phase, *before* the strain develops. That is, it requires that γ and γ' be of the same sign (in this case, negative). Insofar as $\gamma' > \gamma$, this is automatic for rhombohedral $T = 0$ materials, which must have $\gamma' < 0$. If both γ and γ' were of positive sign, one might imagine a scenario in which a "six-site model" would give rise to a transition from cubic to rhombohedral, orthorhombic, and tetragonal, as the order parameter freezes onto subsets of three, two, and one $\langle 111 \rangle$ minima, respectively. However, for $PbTiO_3$ we have γ and γ' of opposite sign, so that such a scenario is not plausible. If this situation is typical of materials with tetragonal $T = 0$ structures, it would explain why the reversed sequence is not observed.

We emphasize that we do not have in hand all the elements needed to construct a theory of the phase transition from first principles. Nevertheless, we have obtained many of the ingredients that would enter such a theory.[9] In particular, we have calculated virtually all the relevant *on-site* couplings, including anharmonic and strain couplings. The most pressing need now is for calculations which will determine some of the *intercell* couplings, especially those at harmonic order. These can be extracted from LDA calculations for phonons away from the Brillouin zone center, using either the supercell frozen phonon approach or a linear response approach. Thus it appears that it may not be long before a thermodynamic theory of the phase transitions in perovskite ferroelectrics may be constructed from first principles.

Of course, the results presented here remind us of a serious limitation of the first-principles LDA approach, connected with the extreme sensitivity of some calculated quantities to the lattice constant. As discussed in the body of the paper, we find that LDA underestimates lattice constants by approximately 1% in perovskites, as is common for other materials. Unfortunately, because of the proximity to the ferroelectric phase transition in the perovskites, this 1% error can translate into large errors in such quantities as the magnitude of the $T = 0$ distortion, the spontaneous polarization, and ultimately, in the ferroelectric transition temperature. However, there is no reason to expect it to have a radical effect on many of the other calculated quantities, such as the values of the anharmonic and strain couplings and the soft-mode eigenvectors. If and when it becomes possible to calculate pressure-temperature phase diagrams from first-principles LDA calculations, we anticipate that the pressure axis may have to be artificially shifted to accommodate the $\sim 1\%$ lattice-constant error. But we are optimistic that the structure of the phase diagram (sequence of phases, first-order vs second-order transitions, boundaries, etc.) will otherwise be reliable.

VI. CONCLUSIONS

We have performed accurate first-principles pseudopotential calculations on eight perovskite compounds within an ultrasoft-pseudopotential approach and the LDA. We have shown that it is possible to devise a computationally tractable scheme to compute the soft-mode total-energy surface correct to fourth order in the soft-mode displacement. Our convergence tests highlight the need for extreme accuracy in the k-point sets in these calculations.

We find that zone-center instabilities in the cubic perovskite structure are very common, and that all the compounds studied here which have an experimental phase transition also have a zone-center soft mode at the theoretical LDA lattice constant, even in cases where the observed transitions are caused by soft modes away from the Γ point. We find that the LDA correctly predicts the symmetry of the ground-state structures of $BaZrO_3$, $BaTiO_3$, $KNbO_3$, and $PbTiO_3$. The remaining compounds have ground-state unit cells with more than five atoms, and the determination of their ground states therefore lies beyond the scope of the present study.

ACKNOWLEDGMENTS

APPENDIX A

Our objective here is to solve the matrix equation for the strain $\widetilde{\eta}_i$ which minimizes the total energy for a given set of u_α. The symmetry of the problem becomes most readily apparent if we define a new vector y_i with components $y_1 = u_x^2$, $y_2 = u_y^2$, $y_3 = u_z^2$, $y_4 = u_y u_z$, $y_5 = u_z u_x$, $y_6 = u_x u_y$. With this notation Eq. (14) can be written as

$$0 = \sum_i B_{ij}\widetilde{\eta}_j + \frac{1}{2}\sum_j C_{ij} y_j , \tag{A1}$$

where **B** and **C** are both 6×6 matrices with the structure

$$\mathbf{M} = \begin{bmatrix} P & Q & Q & 0 & 0 & 0 \\ Q & P & Q & 0 & 0 & 0 \\ Q & Q & P & 0 & 0 & 0 \\ 0 & 0 & 0 & R & 0 & 0 \\ 0 & 0 & 0 & 0 & R & 0 \\ 0 & 0 & 0 & 0 & 0 & R \end{bmatrix}. \tag{A2}$$

For the **B** matrix $P = B_{11}$, $Q = B_{12}$, and $R = B_{44}$, while for **C** we have $P = B_{1xx}$, $Q = B_{1yy}$, and $R = 2B_{4yz}$. Because **M** is a symmetric matrix it can be written as

$$\mathbf{M} = \mathbf{Z}\Lambda(\mathbf{M})\mathbf{Z}^\dagger, \tag{A3}$$

where $\Lambda(\mathbf{M})$ is the diagonal matrix of eigenvalues of **M** and **Z** is the matrix of orthonormal eigenvectors. The eigenvalues are just $P + 2Q$ (1), $P - Q$ (2), and R (3), where the number in parentheses gives the degeneracy. In terms of the bulk and shear moduli defined in Eqs. (17a)–(17f) the eigenvalues of **B** are B, $2\mu_t$, and μ_r, while the eigenvalues of **C** are C, $2\nu_t$, and $2\nu_r$. The eigenvectors of a matrix of the form **M** can be chosen to be independent of the values of P, Q, and R. For example one simple choice is

$$\mathbf{Z} = \begin{bmatrix} \frac{1}{\sqrt{3}} & 0 & -\frac{2}{\sqrt{6}} & 0 & 0 & 0 \\ \frac{1}{\sqrt{3}} & \frac{1}{\sqrt{2}} & \frac{1}{\sqrt{6}} & 0 & 0 & 0 \\ \frac{1}{\sqrt{3}} & -\frac{1}{\sqrt{2}} & \frac{1}{\sqrt{6}} & 0 & 0 & 0 \\ 0 & 0 & 0 & 1 & 0 & 0 \\ 0 & 0 & 0 & 0 & 1 & 0 \\ 0 & 0 & 0 & 0 & 0 & 1 \end{bmatrix}. \tag{A4}$$

It is clear that the expression for $\widetilde{E}$ given in Eq. (15) can be written as

$$\widetilde{E}(\{u_\alpha\}) = E^{(0)} + \Phi(\{u_\alpha\}) - \frac{1}{8}\sum_{ij} y_i \left[\mathbf{Z}\Lambda(\mathbf{C})\mathbf{Z}^\dagger\mathbf{Z}\Lambda^{-1}(\mathbf{B})\mathbf{Z}^\dagger\mathbf{Z}\Lambda(\mathbf{C})\mathbf{Z}^\dagger\right]_{ij} y_j. \tag{A5}$$

For a symmetric matrix we have $\mathbf{Z}^\dagger\mathbf{Z} = 1$ and thus it is obvious that the matrix in square brackets is just another matrix of the form **M** with eigenvalues $\frac{C^2}{B}$, $2\frac{\nu_t^2}{\mu_t}$, and $4\frac{\nu_r^2}{\mu_r}$. Given the relationship between the eigenvalues and P, Q, and R the components of this matrix are just

$$P = \frac{1}{3}\left(\frac{C^2}{B} + 4\frac{\nu_t^2}{\mu_t}\right), \tag{A6a}$$

$$Q = \frac{1}{3}\left(\frac{C^2}{B} - 2\frac{\nu_t^2}{\mu_t}\right), \tag{A6b}$$

and

$$R = 4\frac{\nu_r^2}{\mu_r}. \tag{A6c}$$

It is now simply a matter of multiplying out the matrix term in Eq. (A5) and using the definition of y_i in terms of u_α to derive Eq. (16).

APPENDIX B

In this appendix we describe the conjugate-gradient (CG) scheme which was employed in the calculations presented in this paper to minimize the Kohn-Sham functional. Probably the best known CG method for use in fast Fourier transform (FFT) based pseudopotential codes is that due to Teter, Payne, and Allan[37] which has been applied with great success to a wide range of problems. This method minimizes the total energy in a band-by-band fashion. Orthogonality is maintained by projecting out from the conjugate direction **h** all components of the vector which are parallel to orbitals at the current k point. The algorithm is further improved with preconditioning based on the diagonal dominance of the kinetic energy at large reciprocal lattice vectors. Teter *et al.* have emphasized the importance of updating the Kohn-Sham Hamiltonian self-consistently on each iteration in order to control the "charge sloshing" instabilities caused by the divergent behavior of the Coulomb interaction at long wavelengths.

We have chosen to formulate our CG scheme using a generalization of the Kohn-Sham energy functional to nonorthogonal orbitals in a manner which is very similar to an idea which was recently proposed by Galli and Parrinello.[38] Two major benefits arise from this general functional. First, the CG algorithm does not lend itself easily to constrained minimization problems, particularly if one should wish to move away from band-by-band types of schemes. By choosing to work with nonorthogonal orbitals, we dispense with the need to impose the orthogonality constraint during the course of the minimization process. Second, the nonlocal overlap operator $\hat{S}$ which occurs in the Vanderbilt ultrasoft-pseudopotential scheme is easily incorporated into the formalism.

A second major ingredient of our method is to minimize the Kohn-Sham functional with respect to all the wave-function degrees of freedom simultaneously. In the one-band-at-a-time approach it is fruitless to iterate any

given band to self-consistency, because iterating on later bands changes the total potential, destroying the self-consistency of previous bands. The sequential approach limits the number of CG steps which can usefully be performed on any given band to about 5.[37] Within the approach preferred here, where all bands at all k points are changed on each iteration, this self-consistency consideration does not come into play and as many CG steps as desired can be performed before a restart. Our experience has been that one set of 20 steps of the CG algorithm is considerably more efficient that four sets of 5 steps and that quite substantial gains in performance can therefore be made.

In the following we shall develop our formulation for the case where the number of electrons in each occupied band at each k point is the same. This restriction is not necessary and the question of how to handle the more general case of variable occupation has recently been addressed by Arias et $al.$[39] We shall also concentrate on the case where we have a single k point, as the extension to the multiple k-point case is trivial. Within the ultrasoft framework the Kohn-Sham functional is written in terms of a set of linearly independent nonorthogonal orbitals $\{\phi_i\}$ as

$$E_{\text{tot}}[\{\phi_i\}, \{\mathbf{R}_I\}] = \sum_i \langle \phi_i \mid -\tfrac{1}{2}\nabla^2 + V_{\text{NL}} \mid \overline{\phi}_i \rangle$$
$$+ \frac{1}{2} \int \int d\mathbf{r} d\mathbf{r}' \frac{n(\mathbf{r})n(\mathbf{r}')}{\mid \mathbf{r} - \mathbf{r}' \mid} \quad \text{(B1a)}$$
$$+ E_{\text{xc}}[n] + \int d\mathbf{r} V_{\text{loc}}^{\text{ion}}(\mathbf{r})n(\mathbf{r}) + U(\{\mathbf{R}_I\}),$$

where the charge density $n(\mathbf{r})$ is given by

$$n(\mathbf{r}) = \sum_i \phi_i^*(\mathbf{r})\overline{\phi}_i(\mathbf{r})$$
$$+ \sum_i \sum_{nmI} Q_{nm}^I(\mathbf{r})\langle \phi_i \mid \beta_m^I \rangle\langle \beta_n^I \mid \overline{\phi}_i \rangle, \quad \text{(B1b)}$$

with

$$\overline{\phi}_i = \sum_j \phi_j T_{ji} \quad \text{(B1c)}$$

and

$$[T^{-1}]_{ji} = \langle \phi_j \mid \hat{S} \mid \phi_i \rangle. \quad \text{(B1d)}$$

In Eq. (B1a) V_{NL} is the nonlocal potential, $V_{\text{loc}}^{\text{ion}}$ is the local ionic potential, i is an index running over all occupied bands, n and m are indices running over projector functions $\mid \beta\rangle$ on a given atom, I is an index running over atoms, and $U(\{\mathbf{R}_I\})$ is the ion-ion interaction energy. A complete discussion of all of the meaning of the terms in Eq. (B1a) can be found in Ref. 14. Conventionally the Kohn-Sham energy in the Vanderbilt scheme is written in terms of a set of $\hat{S}$-orthonormal orbitals.[14] The energy computed in Eq. (B1a) is identical to that computed with the conventional expression using any set of of $\hat{S}$-orthonormal orbitals which span the same space as $\{\phi_i(\mathbf{r})\}$. Note that the above expressions are equally applicable to the more usual plane-wave formulations using

Kleinman-Bylander potentials: This limit is recovered by setting $\hat{S}$ to the unit operator and the $Q_{nm}^I(\mathbf{r})$ functions to zero.

The functional derivative of E_{tot} with respect to ϕ_i^* (Ref. 38) is given by

$$\frac{\delta E_{\text{tot}}}{\delta \phi_i^*} = \hat{H} \mid \overline{\phi}_i \rangle - \sum_j \hat{S} \mid \overline{\phi}_j \rangle\langle \phi_j \mid \hat{H} \mid \overline{\phi}_i \rangle, \quad \text{(B2)}$$

where $\hat{H}$ is the usual Kohn-Sham Hamiltonian in the Vanderbilt ultrasoft scheme.[14] Note that since $\langle \phi_k \mid \hat{S} \mid \overline{\phi}_j \rangle = \delta_{kj}$ we have $\langle \phi_k \mid \frac{\delta E_{\text{tot}}}{\delta \phi_i^*} \rangle = 0$, which implies that the projection of any occupied orbital on the gradient direction is zero. Physically, adding any amount of the state ϕ_k to the state ϕ_i does not change the subspace spanned by the occupied orbitals and thus leaves the total energy unchanged.

We start our CG iteration with a set of $\hat{S}$-orthonormal $\{\phi_i\}$ obtained from a random number generator or a previous calculation and compute a G-space diagonal preconditioning matrix $\mathbf{K}$ following the algorithm of Teter et $al.$[37] A standard preconditioned CG algorithm is then used to minimize the Kohn-Sham functional. Thus on iteration $n + 1$ our gradient is just

$$\mathbf{g}^{n+1} = -\frac{\delta E_{\text{tot}}^n}{\delta \phi_i^*}, \quad \text{(B3a)}$$

where it is implicit that the gradient is to be evaluated with the orbitals $\{\phi_i^n\}$ obtained from the nth iteration. The conjugate search direction $\mathbf{h}^{n+1}$ is

$$\mathbf{h}^{n+1} = \mathbf{K} \cdot \mathbf{g}^{n+1} + \gamma^n \mathbf{h}^n, \quad \text{(B3b)}$$

where

$$\gamma^n = \frac{(\mathbf{g}^{n+1})^\dagger \cdot \mathbf{K} \cdot \mathbf{g}^{n+1}}{(\mathbf{g}^n)^\dagger \cdot \mathbf{K} \cdot \mathbf{g}^n}. \quad \text{(B3c)}$$

The line minimizations along the conjugate directions are performed using a variant of the method suggested in Ref. 37. We assume that the energy functional varies quadratically in the region of interest. The total energy and gradient at the point in function space $\{\phi_i^n\}$ are known which fixes two parameters of our quadratic form. The final parameter is obtained by taking a small step along the direction $\mathbf{h}^{n+1}$ and recomputing the self-consistent total energy. Typically the size of the trial step is simply taken to be about the size of step which minimized the function on the previous step.

In order to illustrate the benefits of iterating on all the degrees of freedom at once we have performed two calculations on a five-atom unit cell of $BaTiO_3$ using ten k points in the irreducible wedge of the zone. The first calculation proceeded by minimizing one k point at a time using five CG steps at each k point, where as the second calculation iterated on all k points at once and used 15 CG steps between restarts. The results are illustrated in Fig. 7. Each pass through all the bands was counted as five iterations in the k-point-by-k-point case so comparisons could be made. Relaxing all degrees of freedom at once speeds the calculation by about a factor of 2.
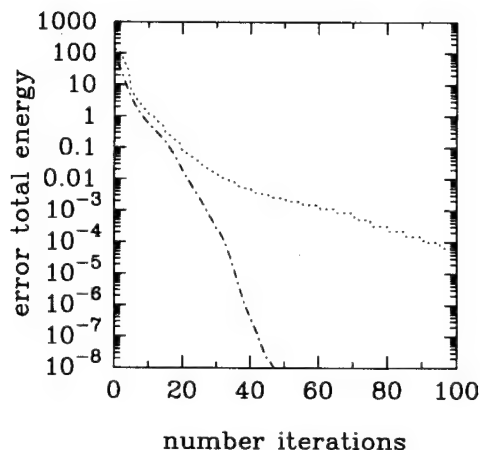
FIG. 7. Error in total energy per unit cell in hartrees vs iteration number using the k-point-by-k-point method (dotted line) and all-k-points-together approach (dashed line).

The operation count per band per iteration is better for a method which updates all the wave-function coefficients together because the Hartree and exchange correlation potential need to be updated much less frequently. This is of particular importance in the Vanderbilt ultrasoft scheme, because augmentation of the density would become a major cost of the calculation if it were done on a band-by-band basis. When all the bands are updated simultaneously the augmentation overhead in the ten k-point calculation discussed above took less than 2% of the time on each CG step. For the size of unit cell considered in this paper the most efficient scheme that we have found for computing the regular contribution to the charge density is to explicitly construct an $\hat{S}$-orthonormal set of orbitals $\{\psi_i\}$ in reciprocal space which span the space of $\{\phi_i\}$. Thus we evaluate $\sum_i \phi_i^*(\mathbf{r})\bar{\phi}_i(\mathbf{r})$ in Eq. (B1b) as $\sum_i \psi_i^*(\mathbf{r})\psi_i(\mathbf{r})$, which can be done with a single FFT per band.

The major drawback of this scheme is that the amount of gradient and conjugate-gradient direction information which must be stored is substantially increased. However, we have found that it is possible to structure the codes so this information is read and written to a disk, without incurring substantial input-output penalties, both on workstations and on the Cray YMP (where we utilized a solid-state disk). In our current implementation of the scheme we use one major work array dimensioned to all the wave functions at all k points and a second smaller array which is sufficient to hold the wave functions at a single k point. Three disk scratch files were used to store current values of $\{\phi_i\}$, the gradient direction, and the conjugate direction.

*Permanent address: Biosym Technologies Inc., 9685 Scranton Rd., San Diego, CA 92122.

[1]M.E. Lines and A.M. Glass, *Principles and Applications of Ferroelectrics and Related Materials* (Clarendon Press, Oxford, 1977).

[2]K.M. Rabe and J.D. Joannopoulos, Phys. Rev. Lett. **59**, 570 (1987); Phys. Rev. B **36**, 6631 (1987).

[3]R.E. Cohen and H. Krakauer, Phys. Rev. B **42**, 6416 (1990).

[4]R.E. Cohen and H. Krakauer, Ferroelectrics **136**, 65 (1992).

[5]R.E. Cohen, Nature **358**, 136 (1992).

[6]D.J. Singh and L.L. Boyer, Ferroelectrics **136**, 95 (1992).

[7]R.D. King-Smith and D. Vanderbilt, Ferroelectrics **136**, 85 (1992).

[8]T. Mitsui et al., *Ferro- and Antiferroelectric Substances*, Landolt-Börnstein, Group III, Vol. 3, edited by K.-H. Hellwege and A.M. Hellwege (Springer-Verlag, Berlin, 1969).

[9]E. Pytte, Phys. Rev. B **5**, 3758 (1972).

[10]D. Vanderbilt, S.H. Taole, and S. Narasimhan, Phys. Rev. B **40**, 5657 (1989).

[11]It is straightforward to show that to lowest order in u_α, $\tilde{u}_\alpha^j(\{u_\alpha\})$ is given by solution of $\lambda(j)\tilde{u}_\alpha^j(\{u_\alpha\}) + \frac{1}{6}\sum_{\beta,\gamma,\delta}\left(\partial^4 E/\partial u_\alpha^j \partial u_\beta \partial u_\gamma \partial u_\delta\right)\big|_0 u_\beta u_\gamma u_\delta = 0$. We thus conclude that the variation of $\tilde{u}_\alpha^j(\{u_\alpha\})$ is at least third order in u_α, and that couplings of the soft mode to other phonons gives rise to sixth-order corrections in the energy.

[12]D. Vanderbilt, Phys. Rev. B **41**, 7892 (1990).

[13]K. Laasonen, R. Car, C. Lee, and D. Vanderbilt, Phys. Rev. B **43**, 6796 (1991).

[14]K. Laasonen, A. Pasquarello, R. Car, C. Lee, and D. Vanderbilt, Phys. Rev. B **47**, 10 142 (1993).

[15]C. Lee, D. Vanderbilt, K. Laasonen, R. Car, and M. Parrinello, Phys. Rev. Lett. **69**, 462 (1992).

[16]A. Pasquarello, K. Laasonen, R. Car, C. Lee, and D. Vanderbilt, Phys. Rev. Lett. **69**, 1982 (1992).

[17]A.M. Rappe, K.M. Rabe, E. Kaxiras, and J.D. Joannopoulos, Phys. Rev. B **41**, 1227 (1990).

[18]L. Kleinman and D.M. Bylander, Phys. Rev. Lett. **48**, 1425 (1982).

[19]D.R. Hamann, M. Schlüter, and C. Chiang, Phys. Rev. Lett. **43**, 1494 (1979).

[20]M.P. Teter, Phys. Rev. B **48**, 5031 (1993).

[21]K. Kunc, R. Zeyher, A.I. Liechtenstein, M. Methfessel, and O.K. Andersen, Solid State Commun. **80**, 325 (1991).

[22]G.B. Bachelet, D.R. Hamann, and M. Schlüter, Phys. Rev. B **26**, 4199 (1982).

[23]D.D. Koelling and B.N. Harmon, J. Phys. C **10**, 3107 (1977).

[24]L. Kleinman, Phys. Rev. B **21**, 2630 (1980).

[25]H.J. Monkhorst and J.D. Pack, Phys. Rev. B **13**, 5188 (1976).

[26]D.M. Ceperley and B.J. Alder, Phys. Rev. Lett. **45**, 566 (1980).

[27]R.D. Shannon and C.T. Prewitt, Acta Crystallogr. B **25**, 925 (1969).

[28]J.C. Slater, Phys. Rev. **78**, 748 (1950).

[29]A.W. Hewat, Ferroelectrics **6**, 215 (1974).

[30]A.W. Hewat, J. Phys. C **6**, 2559 (1973).

[31]G. Shirane, R. Pepinsky, and B.C. Frazer, Acta Crystallogr. **9**, 131 (1955).

[32]R.E. Cohen (private communication).

[33]R.O. Bell and G. Rupprecht, Phys. Rev. **129**, 90 (1963).

[34]L.F. Mattheiss, Phys. Rev. B **6**, 4718 (1972).

[35]W.A. Harrison, *Electronic Structure and the Properties of Solids* (Dover, New York, 1989), Chap. 19.

[36]Ş. Ellialtioğlu and T. Wolfram, Phys. Rev. B **15**, 5909 (1977); T. Wolfram and Ş. Ellialtioğlu, *ibid.* **25**, 2697

(1981).

[37] M.P. Teter, M.C. Payne, and D.C. Allen, Phys. Rev. B **40**, 12 225 (1989).

[38] G. Galli and M. Parrinello, Phys. Rev. Lett. **69**, 3547 (1992).

[39] T.A. Arias, M.C. Payne, and J.D. Joannopoulos, Phys. Rev. Lett. **69**, 1077 (1992).

Theory of polarization of crystalline solids

R. D. King-Smith and David Vanderbilt

Department of Physics and Astronomy, Rutgers University, P. O. Box 849, Piscataway, New Jersey 08855-0849
(Received 10 June 1992)

We consider the change in polarization ΔP which occurs upon making an adiabatic change in the Kohn-Sham Hamiltonian of the solid. A simple expression for ΔP is derived in terms of the valence band wave functions of the initial and final Hamiltonians. We show that physically ΔP can be interpreted as a displacement of the center of charge of the Wannier functions. The formulation is successfully applied to compute the piezoelectric tensor of GaAs in a first-principles pseudopotential calculation.

Experimentally changes in the electrical polarization of solids can be induced by various means including application of a strain (piezoelectricity) or changes in temperature (pyroelectricity). Ferroelectrics are a technologically important class of materials whose polarization can be switched by application of an electric field.[1] To date there have been relatively few theoretical attempts to calculate these quantities from a quantum-mechanical starting point. In this paper we derive simple formulas for calculating finite changes in the polarization of a crystalline solid. The method is ideally suited to first-principles density-functional investigations of polarization effects.

We begin by considering the change in the electronic polarization per unit volume of a crystal which is induced upon making an adiabatic change in the self-consistent Kohn-Sham potential. We parametrize the change in the potential with a variable λ which is arranged to have values 0 and 1 at initial and final values of the potential, respectively. In the following we shall specialize to the case where the change in potential preserves the translational symmetry of the solid. The formalism developed below will therefore be applicable for computing ΔP with macroscopic electric field $\mathbf{E}$ held to be zero. If the material is an insulator for all values of λ in the range 0–1 then we have

$$\partial P_\alpha/\partial\lambda = -\frac{ifq_e\hbar}{N\Omega m_e}\sum_{\mathbf{k}}\sum_{n=1}^{M}\sum_{m=M+1}^{\infty}\frac{\langle\psi_{\mathbf{k}n}^{(\lambda)}|\hat{p}_\alpha|\psi_{\mathbf{k}m}^{(\lambda)}\rangle\langle\psi_{\mathbf{k}m}^{(\lambda)}|\partial V_{\mathrm{KS}}^{(\lambda)}/\partial\lambda|\psi_{\mathbf{k}n}^{(\lambda)}\rangle}{(\epsilon_{\mathbf{k}n}^{(\lambda)}-\epsilon_{\mathbf{k}m}^{(\lambda)})^2} + \text{c.c.} ,\tag{1}$$

where α is a Cartesian direction, m_e and q_e are the electron mass and charge, N is the number of unit cells in the crystal, Ω is the volume of a unit cell, f is the occupation number of states in the valence band (in spin-degenerate systems $f=2$), M is the number of occupied bands, $\hat{p}$ is the momentum operator, and $V_{\mathrm{KS}}^{(\lambda)}$ is the Kohn-Sham potential. A heuristic derivation of Eq. (1) has recently been given by Resta.[2] Resta proposes that we compute the total change in polarization per unit volume, ΔP, using

$$\Delta P = \int_0^1 (\partial P/\partial\lambda)d\lambda .\tag{2}$$

Physically, ΔP arises from the flow of polarization currents in the solid and Eq. (1) may also be regarded as the adiabatic limit of a Kubo formula for the current.[3] It is somewhat surprising that the change in polarization can be computed without explicitly stating how the crystal is terminated. The fundamental justification for taking the thermodynamic limit in Eq. (1) rests with the fact that the current response of an insulator depends only on the local environment.[4,5]

The expression for $\partial P/\partial\lambda$ can be recast in a form in which conduction-band states do not explicitly appear using an argument developed by Thouless *et al.*[6] in their analysis of the quantum Hall effect. We introduce a set of cell-periodic functions, $u_{\mathbf{k}n}^{(\lambda)}$, with a choice of phases such that $u_{\mathbf{k}n}^{(\lambda)}$ are analytic in both $\mathbf{k}$ and λ. The matrix elements in Eq. (1) can be rewritten as

$$\langle\psi_{\mathbf{k}n}^{(\lambda)}|\hat{p}_\alpha|\psi_{\mathbf{k}m}^{(\lambda)}\rangle = \frac{m_e}{\hbar}\langle u_{\mathbf{k}n}^{(\lambda)}|[\partial/\partial k_\alpha, \hat{H}_{\mathbf{k}}^{(\lambda)}]|u_{\mathbf{k}m}^{(\lambda)}\rangle\tag{3a}$$

and

$$\langle\psi_{\mathbf{k}n}^{(\lambda)}|\partial V_{\mathrm{KS}}^{(\lambda)}/\partial\lambda|\psi_{\mathbf{k}m}^{(\lambda)}\rangle = \langle u_{\mathbf{k}n}^{(\lambda)}|[\partial/\partial\lambda, \hat{H}_{\mathbf{k}}^{(\lambda)}]|u_{\mathbf{k}m}^{(\lambda)}\rangle ,\tag{3b}$$

where the $\hat{H}_{\mathbf{k}}^{(\lambda)}$ is the cell-periodic Hamiltonian

$$\hat{H}_{\mathbf{k}}^{(\lambda)} = (1/2m_e)(-i\hbar\nabla + \hbar\mathbf{k})^2 + V_{\mathrm{KS}}^{(\lambda)}(r) .\tag{3c}$$

Substituting Eqs. (3a) and (3b) into Eq. (1) it is straightforward to show by analogy with Ref. 6 that

$$\Delta P_\alpha = -(ifq_e/8\pi^3)\sum_{n=1}^{M}\int_{\mathrm{BZ}}d\mathbf{k}\int_0^1 d\lambda[\langle\partial u_{\mathbf{k}n}^{(\lambda)}/\partial k_\alpha|\partial u_{\mathbf{k}n}^{(\lambda)}/\partial\lambda\rangle - \langle\partial u_{\mathbf{k}n}^{(\lambda)}/\partial\lambda|\partial u_{\mathbf{k}n}^{(\lambda)}/\partial k_\alpha\rangle] ,\tag{4}$$

where the integral over $\mathbf{k}$ extends over any primitive cell in reciprocal space. The one-dimensional (1D) analogue of Eq. (4) has been derived previously by Thouless[7] in a

slightly different context for the case of noninteracting electrons where the formal similarities with the quantum Hall effect are particularly striking. For example, in a

1D system with period a, Stokes's theorem allows us to write the change in polarization per unit length as

$$\Delta P = -\frac{c_e}{2\pi} \sum_{n=1}^{t} \left\{ i \oint_C \sum_{j=1}^{2} d\tau_j \langle u_{\mathbf{k}n}^{(\lambda)} | \partial/\partial\tau_j | u_{\mathbf{k}n}^{(\lambda)} \rangle \right\} , \tag{5}$$

where τ is a two-component vector with elements (λ, k) and the contour of integration C is around the loop in τ space from $(0, \pi/a) \to (1, \pi/a) \to (1, -\pi/a) \to (0, -\pi/a) \to (0, \pi/a)$. The quantity in curly brackets can be recognized as the change in Berry phase for fictitious adiabatic evolution of the cell-periodic wave function around the loop C.[8,9] Thouless has observed that the contour integral in Eq. (5) is quantized in the special case where the potential is the same at $\lambda = 1$ and 0. In these circumstances the quantity in curly brackets measures the change in the phase of the wave function at any given real-space point as (λ, k) is taken around C. Given that

the cell-periodic parts of the wave function can be chosen to be analytic in k and λ this change in phase must be an integer multiple of 2π. We therefore conclude that the polarization per unit length of a 1D system can only change by an integer multiple of fe for adiabatic changes in the Hamiltonian for which $V_{KS}^{(0)} = V_{KS}^{(1)}$. An analogous result for 3D systems will be derived below.

The physical content of Eq. (4) can be made more readily apparent by working in a gauge where the wave functions are periodic in reciprocal space, i.e., $\psi_{\mathbf{k},n}^{(\lambda)}(\mathbf{r}) = \psi_{\mathbf{k}+\mathbf{G},n}^{(\lambda)}(\mathbf{r})$ for all reciprocal lattice vectors $\mathbf{G}$. In terms of the cell-periodic functions in such a gauge we have

$$u_{\mathbf{k},n}^{(\lambda)}(\mathbf{r}) = e^{i\mathbf{G}\cdot\mathbf{r}} u_{\mathbf{k}+\mathbf{G},n}^{(\lambda)}(\mathbf{r}) . \tag{6}$$

We remark that the gauge condition of Eq. (6) does not uniquely define the phase of the wave functions. Integrating Eq. (4) by parts we find that

$$\Delta P_\alpha = \frac{ifq_e}{8\pi^3} \sum_{n=1}^{M} \int_{BZ} d\mathbf{k} \left\{ [\langle u_{\mathbf{k}n}^{(\lambda)} | \partial/\partial k_\alpha | u_{\mathbf{k}n}^{(\lambda)} \rangle]_0^1 - \int_0^1 d\lambda \frac{\partial}{\partial k_\alpha} \langle u_{\mathbf{k}n}^{(\lambda)} | \partial/\partial\lambda | u_{\mathbf{k}n}^{(\lambda)} \rangle \right\} . \tag{7}$$

With our choice of gauge, $\langle u_{\mathbf{k}n}^{(\lambda)} | \partial/\partial\lambda | u_{\mathbf{k}n}^{(\lambda)} \rangle$ is periodic in $\mathbf{k}$. The gradient of this quantity integrated over the Brillouin zone (BZ) is therefore zero, so the second term in Eq. (7) makes no contribution. In the periodic gauge we therefore arrive at the conclusion that

$$\Delta \mathbf{P} = \mathbf{P}^{(1)} - \mathbf{P}^{(0)} , \tag{8a}$$

where

$$P_\alpha^{(\lambda)} = (ifq_e/8\pi^3) \sum_{n=1}^{M} \int_{BZ} d\mathbf{k} \langle u_{\mathbf{k}n}^{(\lambda)} | \partial/\partial k_\alpha | u_{\mathbf{k}n}^{(\lambda)} \rangle . \tag{8b}$$

The integral on the right-hand side of Eq. (8b) is closely related to the Berry phase of band n, a quantity which has been recently introduced by Zak and co-workers.[10] The form of Eq. (8) is particularly simple when written in terms of the Wannier functions $W_n^{(\lambda)}(\mathbf{r})$ of the occupied bands.[10] The Wannier functions depend on the particular choice of phases used in the periodic gauge. We define the Wannier function using

$$W_n^{(\lambda)}(\mathbf{r}-\mathbf{R}) = (\sqrt{N}\,\Omega/8\pi^3) \int_{BZ} d\mathbf{k}\, e^{i\mathbf{k}\cdot(\mathbf{r}-\mathbf{R})} u_{\mathbf{k}n}^{(\lambda)}(\mathbf{r}) \tag{9a}$$

which implies that

$$u_{\mathbf{k}n}^{(\lambda)}(\mathbf{r}) = (1/\sqrt{N}) \sum_{\mathbf{R}} e^{-i\mathbf{k}\cdot(\mathbf{r}-\mathbf{R})} W_n^{(\lambda)}(\mathbf{r}-\mathbf{R}) , \tag{9b}$$

where the sum over $\mathbf{R}$ runs over all real-space lattice vectors. Substituting Eq. (9b) into (8b) we find the simple result that

$$\mathbf{P}^{(\lambda)} = (fq_e/\Omega) \sum_{n=1}^{M} \int \mathbf{r} |W_n^{(\lambda)}(\mathbf{r})|^2 d\mathbf{r} . \tag{10}$$

Physically, Eqs. (8a) and (10) state that the change in polarization of the solid is proportional to the displacement

of the center of charge of the Wannier functions induced by the adiabatic change in the Hamiltonian.

Returning to the case where the Hamiltonians at $\lambda = 0$ and 1 are identical, $u_{\mathbf{k}n}^{(0)}(\mathbf{r})$ and $u_{\mathbf{k}n}^{(1)}(\mathbf{r})$ can at most differ by a phase factor so that

$$u_{\mathbf{k}n}^{(1)}(\mathbf{r}) = e^{i\theta_{\mathbf{k}n}} u_{\mathbf{k}n}^{(0)}(\mathbf{r}) . \tag{11}$$

In this limit Eq. (8) reduces to

$$\Delta P_\alpha = -(fq_e/8\pi^3) \sum_{n=1}^{M} \int_{BZ} d\mathbf{k}\, \partial\theta_{\mathbf{k}n}/\partial k_\alpha . \tag{12}$$

With our periodic choice of gauge $e^{i\theta_{\mathbf{k}n}}$ must be periodic in $\mathbf{k}$. The most general form for the phase angle under these circumstances is $\theta_{\mathbf{k}n} = \beta_{\mathbf{k}n} + \mathbf{k}\cdot\mathbf{R}_n$, where $\beta_{\mathbf{k}n}$ is periodic in $\mathbf{k}$. We thus conclude that

$$\Delta \mathbf{P} = (fq_e/\Omega) \sum_{n=1}^{M} \mathbf{R}_n . \tag{13}$$

The change in polarization per unit volume for paths where the Hamiltonian returns to itself is therefore quantized in units of $(fq_e/\Omega)\mathbf{R}$. A particularly simple case to consider is the magnitude of $\Delta \mathbf{P}$ for paths of the form $V_{KS}^{(\lambda)}(\mathbf{r}) = V_{KS}^{(0)}(\mathbf{r}-\lambda\mathbf{R})$, which physically corresponds to a translation of the crystal. In this case it is straightforward to verify by explicit calculation that Eq. (8) yields $\Delta \mathbf{P} = (fq_e/\Omega)M\mathbf{R}$, as one would expect on physical grounds.

We have in Eqs. (8) and (13) the rather remarkable result that $\Delta \mathbf{P}$ for a crystal can in principle be determined, to within a factor of $(fe/\Omega)\mathbf{R}$, from a knowledge of the valence-band Kohn-Sham wave functions at $\lambda = 0$ and 1. In practice the arbitrary factor of $(fe/\Omega)\mathbf{R}$ can often be eliminated by inspection because one is usually interested in polarization changes where $|\Delta \mathbf{P}| \ll |(fe/\Omega)\mathbf{R}_1|$ where $\mathbf{R}_1$ is the shortest nonzero real-space lattice vector. In

other cases any uncertainties introduced by this factor can always be removed by dividing the change in the Hamiltonian into a number of subintervals.

Direct evaluation of $\Delta\mathbf{P}$ via Eq. (8) is cumbersome in numerical calculations, because in practice we only compute the wave functions at a finite number of points in the Brillouin zone, and in general there will be no particular phase relationship between the eigenvectors generated by the diagonalization routine. In actual calculations we circumvent this difficulty using the following strategy. First we pick a direction parallel to a short reciprocal-lattice vector of the solid, $\mathbf{G}_{\parallel}$. We choose the primitive cell for the $\mathbf{k}$-space integration to be a prism with its axis aligned along $\mathbf{G}_{\parallel}$. The component of $\Delta\mathbf{P}$ directed along $\mathbf{G}_{\parallel}$ can be written

$$\Delta P_{\parallel} = P_{\parallel}^{(1)} - P_{\parallel}^{(0)} \; , \qquad (14a)$$

where, in an obvious notation

$$P_{\parallel}^{(\lambda)} = \frac{ifq_e}{8\pi^3} \int_A d\mathbf{k}_{\perp} \sum_{n=1}^{M} \int_0^{|\mathbf{G}_{\parallel}|} dk_{\parallel} \left\langle u_{\mathbf{k}n}^{(\lambda)} \left| \frac{\partial}{\partial k_{\parallel}} \right| u_{\mathbf{k}n}^{(\lambda)} \right\rangle . \qquad (14b)$$

The integration in the perpendicular direction poses no special problems and can be performed by sampling over a 2D mesh of k points generated, for example, using the Monkhorst-Pack method.[12] To perform the integral over $k_{\parallel}$ at each point in the $k_{\perp}$ mesh we compute the cell-periodic parts of the wave functions at the string of J k points at $\mathbf{k}_j = \mathbf{k}_{\perp} + j\mathbf{G}_{\parallel}/J$ where j runs from 0 to $J-1$. We then compute the variable $\phi_J^{(\lambda)}(\mathbf{k}_{\perp})$ defined through

$$\phi_J^{(\lambda)}(\mathbf{k}_{\perp}) = \mathrm{Im}\left\{ \ln \prod_{j=0}^{J-1} \det(\langle u_{\mathbf{k}_j,m}^{(\lambda)} | u_{\mathbf{k}_{j+1},n}^{(\lambda)} \rangle) \right\} , \qquad (15)$$

where it is understood that $u_{\mathbf{k}_j,n}^{(\lambda)} = e^{-i\mathbf{G}_{\parallel}\cdot\mathbf{r}} u_{\mathbf{k}_0,n}^{(\lambda)}$. The determinant in Eq. (15) is that of the $M \times M$ matrix formed by allowing n and m to run over all valence bands. With an analytic choice of cell-periodic wave functions it can be verified that

$$\phi^{(\lambda)}(\mathbf{k}_{\perp}) \equiv \lim_{J\to\infty} \phi_J^{(\lambda)}(\mathbf{k}_{\perp})$$

$$= -i \sum_{n=1}^{M} \int_0^{|\mathbf{G}_{\parallel}|} dk_{\parallel} \langle u_{\mathbf{k}n}^{(\lambda)} | \partial/\partial k_{\parallel} | u_{\mathbf{k}n}^{(\lambda)} \rangle \qquad (16a)$$

so our expression for $P_{\parallel}^{(\lambda)}$ becomes

$$P_{\parallel}^{(\lambda)} = -(fq_e/8\pi^3) \int_A d\mathbf{k}_{\perp} \phi^{(\lambda)}(\mathbf{k}_{\perp}) . \qquad (16b)$$

It is straightforward to confirm that the product over j in Eq. (15) is independent of how the phases of the wave functions are chosen. Changes of the phase of $u_{\mathbf{k}n}^{(\lambda)}$ can change the value of the integral in Eq. (16) by an integer multiple of 2π. Correspondingly the arbitrary constant in the definition of $\phi_J^{(\lambda)}(\mathbf{k}_{\perp})$ given in Eq. (15) arises from the fact that the imaginary part of the log of a complex number is only defined up to a constant multiple of 2π. In practice the arbitrary constant is removed by comparing $\phi_J^{(1)}(\mathbf{k}_{\perp})$ with $\phi_J^{(0)}(\mathbf{k}_{\perp})$ using the argument outlined in the previous paragraph.

We have in Eqs. (14)–(16) all the ingredients necessary for computing polarization changes in a practical calculation. Within this approach the need for supercells or linear-response techniques is completely avoided.[1] The method is ideally suited to modern electronic structure methods based on iterative diagonalization techniques, which concentrate on computing the valence-band wave functions only.[13]

We illustrate the approach by computing the transverse effective charge tensor and piezoelectric constant of GaAs in a first-principles pseudopotential calculation. The effective charge of GaAs may be determined by computing the change in polarization which is induced on making a small displacement of one sublattice with the boundary condition $\mathbf{E}=0$. For example, if we move the Ga sublattice by a vector $\mathbf{u}$, then the electronic contribution to the polarization difference between the distorted and undistorted structures is

$$\Delta\mathbf{P} = (e/\Omega)Z_{\mathrm{Ga}}^{*(\mathrm{el})}\mathbf{u} \; , \qquad (17)$$

where $Z_{\mathrm{Ga}}^{*(\mathrm{el})}$ is the electronic contribution to the effective charge. The piezoelectric tensor γ is the strain derivative of the polarization under boundary conditions of $\mathbf{E}=0$. In the zinc-blende structure there is only one independent component of the piezoelectric tensor, γ_{14}. The piezoelectric tensor can be thought of as the sum of two independent terms. The first term, which we denote by $\gamma_{14}^{(0)}$ following Ref. 11, arises from the change in polarization when the ions are subjected to a homogeneous strain. The second contribution owes its origin to the relative displacement of the sublattices, and can be expressed in terms of the effective charges and internal strain parameters.[4,11] It is shown in Ref. 11 that

$$(a^2/e)\gamma_{14} \equiv \bar{\gamma}_{14} = (a^2/e)\gamma_{14}^{(0)} + Z_{\mathrm{Ga}}^{*}\xi \; , \qquad (18)$$

where ξ is the internal strain parameter.

Our first-principles calculations used norm-conserving nonlocal pseudopotentials.[14] We note in passing that, strictly speaking, a nonlocal potential causes a modification to the momentum operator in Eq. (1).[2] However, in this situation there is a precisely compensating change to the Hamiltonian for the cell-periodic part of the wave function, and equations from Eq. (4) on remain correct at they stand. Our calculation treated exchange and correlation in the local-density approximation using the Wigner form. The wave functions were expanded using a 20-Ry plane-wave cutoff. All calculations of the self-consistent Kohn-Sham potential were performed with a (4,4,4) Monkhorst-Pack mesh.[12] Calculations in the cubic structure were performed at the theoretical lattice constant a, which came out to be 5.576 Å with the above parameters. For the calculations of the effective charge we displaced the Ga atom a distance of $0.01a$ in the (001) direction and computed the polarization change in the z direction. The integration mesh for computing $\Delta\mathbf{P}$ used 16 k points in the $\mathbf{k}_{\perp}$ mesh and a string of 10 k points in the parallel direction. We obtained $\gamma_{14}^{(0)}$ by computing the change in polarization in the z directions induced by applying a 1% xy shear strain to the crystal.

The results of our calculation are summarized in Table

The total value of Z_{Ga}^* (electronic plus ionic contributions) came out to be 1.984, in excellent agreement with the value of 1.994 obtained from pseudopotential linear-response calculations.[11] Both sets of theoretical values of Z_{Ga}^* are about 8% smaller than the experimental value. Our calculations on the strained crystal yielded a $(a^2/e)\gamma_{14}^{(0)}$ of -1.352. The value agrees to better than 5% with the result obtained from linear-response methods.[11] Our overall value for the piezoelectric constant $\bar\gamma_{14}$ was -0.28, compared with an experimental value of -0.32. The agreement between our calculation and experiment is reasonable, given that the two terms in Eq. (18) show a strong tendency to cancel. We have checked that our calculation is converged with respect to k-point set and plane-wave cutoff, and that the polarization response is linear in the applied perturbation. We attribute the small differences between our results and those of Gironcoli, Baroni, and Resta[11] to the use of different pseudopotentials and parametrizations of the exchange and correlation potential.

Before closing we note that it is tempting to physically identify the quantity $\mathbf{P}^{(\lambda)}$ defined in Eq. (8b) as the absolute polarization of the perturbed crystal. Of course it would have to be understood that the polarization, defined in this way, would only be well defined modulo $e f \mathbf{R}/\Omega$. The conditions under which such an identification is useful will be the subject of a future com-

munication.

In conclusion, we have shown that adiabatic changes in the Kohn-Sham Hamiltonian lead to polarization changes in the solid which can be computed in terms of the initial and final valence-band wave functions of the system. This result forms the basis for a scheme for computing polarization changes of solids within the context of first-principles total-energy calculations.

TABLE I. Theoretical and experimental piezoelectric response of GaAs.

	This work	Linear response[a]	Experiment
a (Å)	5.576	5.496	5.642
ξ	0.542	0.528	0.55
Z_{Ga}^*	1.984	1.994	2.16
$(a^2/e)\gamma_{14}^{(0)}$	-1.352	-1.405	
$\bar\gamma_{14}$	-0.28	-0.35	-0.32

[a]Reference 11.

[1]M. E. Lines and A. M. Glass, *Principles and Applications of Ferroelectrics and Related Materials* (Clarendon, Oxford, 1977).

[2]R. Resta, Ferroelectrics (to be published).

[3]E. Fradkin, *Field Theories of Condensed Matter Systems* (Addison Wesley, Redwood City, CA, 1991).

[4]R. M. Martin, Phys. Rev. B **5**, 1607 (1972); **6**, 4874 (1972).

[5]C. Kallin and B. I. Halperin, Phys. Rev. B **29**, 2175 (1984).

[6]D. J. Thouless, M. Kohmoto, M. P. Nightingale, and M. den Nijs, Phys. Rev. Lett. **49**, 405 (1982).

[7]D. J. Thouless, Phys. Rev. B **27**, 6083 (1983).

[8]M. V. Berry, Proc. R. Soc. London Ser. A **392**, 45 (1984).

[9]B. Simon, Phys. Rev. Lett. **51**, 2167 (1983).

[10]J. Zak, Phys. Rev. Lett. **62**, 2747 (1989); L. Michel and J. Zak, Europhys. Lett. **18**, 239 (1992).

[11]S. de Gironcoli, S. Baroni, and R. Resta, Phys. Rev. Lett. **62**, 2853 (1989).

[12]H. J. Monkhorst and J. D. Pack, Phys. Rev. B **13**, 5188 (1976).

[13]R. Natarajan and D. Vanderbilt, J. Comput. Phys. **82**, 218 (1989).

[14]D. R. Hamann, M. Schlüter, and C. Chiang, Phys. Rev. Lett. **43**, 1494 (1979).

Giant LO-TO Splittings in Perovskite Ferroelectrics

W. Zhong, R.D. King-Smith,* and David Vanderbilt

Department of Physics and Astronomy, Rutgers University, Piscataway, New Jersey 08855-0849
(Received 30 November 1993)

We perform a first-principles investigation of the role of Coulomb interactions in eight ABO_3 cubic perovskite compounds. The predicted spontaneous polarization and the LO and TO phonon frequencies are found to be in good agreement with experiment. Anomalously large dynamical effective charges give rise to very strong mixing of the mode eigenvectors on going from the TO to the LO case, resulting in a "giant LO-TO splitting" in the sense that the soft TO mode is most closely related to the hardest LO modes. The results help explain the extreme sensitivity of these compounds to electrostatic boundary conditions.

PACS numbers: 77.84.Dy, 63.20.Dj, 77.22.Ej

Ferroelectric materials are characterized by a switchable macroscopic polarization. Their importance stems not only from technological considerations, but also from a fundamental interest in understanding the structural phase transitions and symmetry breaking involved [1]. The perovskite compounds are an extremely important group of ferroelectric materials. Their simple structures allow extensive theoretical investigation. The ferroelectric transition occurs as a result of a delicate balance between long-range Coulomb interactions and short-range forces. Of particular interest is the fact that the long range of the Coulomb interaction can make the ferroelectric instability very sensitive to details of domain structure, defects, and boundary conditions. The splitting between the frequencies of the longitudinal optical (LO) and transverse optical (TO) phonons is another direct effect of such interaction. The Born dynamical effective charges, which reflect the local dipole moments which develop as atoms are moved, play a central role in the study of these Coulomb effects.

The role of Coulomb interactions in perovskites aroused interest as early as the 1960s. The seminal work by Axe suggested anomalous effective charges, based on empirical fitting to experimental mode strengths [2]. However, the quantitative accuracy of that approach is limited by the approximations involved, and by uncertainties in the interpretation of experiment. It is natural to turn to first-principles calculations for a deeper understanding and more accurate predictions. However, early band-structure calculations [3] and more recent work focusing on total energies [4–8] do not directly address the role of Coulomb interactions. In part, this is because a method for direct calculation of electric polarization has only recently become available [9]. Recent work using this new method [10] and linear response theory [11] confirmed anomalous effective charges, but the results were limited to two compounds, and their effects on the dynamical properties and soft phonon instability were not addressed.

In this Letter, we report a systematic series of first-principles calculations of Born effective charges Z^* and

their effect on the optical phonon modes. We find the anomalously large Z^* to be a general feature of perovskite compounds. This leads to large spontaneous polarization for small distortions. Our calculated optical phonon frequencies at the Γ point for both TO and LO modes are in good agreement with experiment. The eigenvector analysis reveals that, in general, there is no correspondence between individual TO and LO modes. However, the softest TO mode usually involves the largest mode effective charge and can couple strongly with the electric field, thus giving an unexpectedly large LO-TO splitting. The strong coupling to the electric field can easily destroy the ferroelectric state. We find that the calculated critical depolarization factor is only ≈ 0.1. This explains the remarkable sensitivity of the ferroelectric state to domain structure and boundary conditions.

The perfect perovskite structure shown in Fig. 1 is cubic with general formula ABO_3, where A and B are metal atoms. We concentrate on eight perovskite compounds: $BaTiO_3$, $SrTiO_3$, $CaTiO_3$, $KNbO_3$, $NaNbO_3$, $PbTiO_3$, $PbZrO_3$, and $BaZrO_3$. We begin with a calculation of
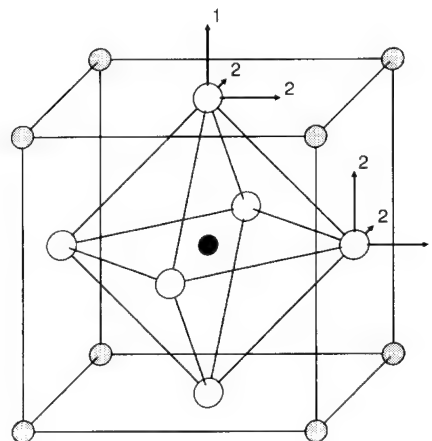

FIG. 1. The structure of cubic perovskite compounds ABO_3. Atoms A, B, and O are represented by shaded, solid, and empty circles, respectively. The small vectors indicate two inequivalent directions for the O atoms.

the Born effective charges from finite differences of the bulk polarization $\mathbf{P}$ under small distortions. The Born effective charge tensor Z_m^* is defined through the equation

$$\delta\mathbf{P} = \frac{e}{\Omega} \sum_{m=1}^{N} Z_m^* \cdot \delta\mathbf{u}_m . \tag{1}$$

Here, N is the number of atoms in the primitive unit cell, $\delta\mathbf{u}_m$ is the first-order change of the position vector of the mth basis atom, and Ω is the volume of the unit cell. Resta et al. [10] have shown that $\mathbf{P}$ is linear in $\mathbf{u}_m$ to a good approximation.

The calculation of polarization follows the new procedure recently introduced in Ref. [9]. The electronic wave functions are obtained from density-functional theory in the local density approximation (LDA), using Vanderbilt's ultrasoft pseudopotential [9,12,13], which allows highly accurate calculations to be performed with a low energy cutoff. A generalized Kohn-Sham functional [8,14] is directly minimized using a preconditioned conjugate gradient method [8,15]. Calculations of structural properties and convergence tests have been presented previously [8]. The electronic polarization $\mathbf{P}$ is calculated using a $4 \times 4 \times 20$ k-point mesh with the dense grid in the direction parallel to $\mathbf{P}$ to achieve high accuracy. The effective charge tensors for the ABO_3 perovskite compounds are then calculated from the polarization differences between perfect and distorted structures.

For the cubic structure, the metal atoms A or B are located at centers of cubic symmetry, so that their effective charge tensors are isotropic. The oxygen atoms are located at the face centers and thus have two inequivalent directions either perpendicular or parallel to the cubic face, labeled 1 or 2, respectively, in Fig. 1. The oxygen effective charge tensors are thus diagonal, with element Z_1^* for direction 1 and Z_2^* for directions 2. Since the formulation we use here satisfies the acoustic sum rule $\sum_m Z_m^* = 0$ exactly, we need three distorted structures to get all the Z_m^*'s. The amplitudes of our distortions are typically 0.2% of the lattice constants.

The calculated Born effective charges are listed in Table I, together with results from other groups. Our results are in good agreement with previous calculations for $KNbO_3$ using finite differences of polarization [10], and for $BaTiO_3$ using variational linear-response theory [11]. The agreement with the empirical approach of Axe [2] is also surprisingly good, suggesting that his modeling was reasonable. The calculations were performed in the theoretical cubic structures. In two cases, we also did the calculations for experimental tetragonal structures, showing that the Z^* are quite insensitive to structural details.

As shown in Table I, the anomalously large $Z^*(B)$ and $Z_1^*(O)$ reported previously for $KNbO_3$ [10] and $BaTiO_3$ [11] are generic to all the perovskites studied here. However, with the exception of the Pb compounds, $Z^*(A)$ and $Z_2^*(O)$ are close to their nominal ionic valence (+1 for Na and K, +2 for Ca, Sr, and Ba, and −2 for O). We find a

TABLE I. Born effective charges for ABO_3 perovskites. $Z_1^*(O)$ and $Z_2^*(O)$ refer to O displacements 1 and 2 of Fig. 1.

	$Z^*(A)$	$Z^*(B)$	$Z_1^*(O)$	$Z_2^*(O)$	Structure
$BaTiO_3$	2.75	7.16	−5.69	−2.11	Cubic
	2.70	7.10	−5.56	−2.12	Cubic[a]
	2.9	6.7	−4.8	−2.4	Cubic[b]
$SrTiO_3$	2.54	7.12	−5.66	−2.00	Cubic
	2.4	7.0	−5.8	−1.8	Cubic[b]
$CaTiO_3$	2.58	7.08	−5.65	−2.00	Cubic
$KNbO_3$	1.14	9.23	−7.01	−1.68	Cubic
	1.14	9.36	−7.10	−1.70	Tetragonal
	0.82	9.13	−6.58	−1.68	Tetragonal[c]
$NaNbO_3$	1.13	9.11	−7.01	−1.61	Cubic
$PbTiO_3$	3.90	7.06	−5.83	−2.56	Cubic
	3.92	6.71	−5.51	−2.56	Tetragonal
$PbZrO_3$	3.92	5.85	−4.81	−2.48	Cubic
$BaZrO_3$	2.73	6.03	−4.74	−2.01	Cubic

[a]Reference [11], using density functional perturbation theory.
[b]Reference [2], empirical approach.
[c]Reference [10], using finite differences of polarization.

strong correlation between the effective charge and chemical species of the metal atoms, i.e., $Z^*(B)$ is independent of A and vice versa. For example, $Z^*(Ti)$ are 7.16, 7.12, 7.08, and 7.06, in compounds $BaTiO_3$, $SrTiO_3$, $CaTiO_3$, and $PbTiO_3$, respectively. Another observation is the strong correlation between $Z^*(B)$ and $Z_1^*(O)$, as well as between $Z^*(A)$ and $Z_2^*(O)$. This is obviously associated with the fact that displacement O_1 modulates the O-B bond, while O_2 modulates the O-A bond.

The anomalously large values of $Z^*(B)$ and $Z_1^*(O)$ indicate that a strong dynamic charge transfer takes place along the O-B bond as the bond length is varied. This can be understood as arising from the weakly ionic character of the bond as follows. At rest, the bonding orbital has most of its character on the O $2p$ orbital; but as it is compressed and the hopping integral increases, the bond becomes more covalent, and the admixture of B d character increases, corresponding to an electron transfer from O to B [16]. It is easily seen that this effect will be strongest for bonds which are on the borderline between ionic and covalent behavior. Thus, we suspect that such anomalous Z^* values will be generic to weakly ionic oxides.

The effective charges can be used to predict the spontaneous polarization P_s for ferroelectric or antiferroelectric materials, given the ground state structure. As a test, we calculate P_s for some structures and compare with experiment. All the structural information is obtained from Landolt-Bornstein [17]. For $BaTiO_3$, the calculated P_s are 0.30, 0.26, and 0.44 C/m^2 for tetragonal, orthorhombic, and rhombohedral phases, compared with experimental values of 0.27, 0.30, and 0.33 C/m^2, respectively [18]. The agreement is very good, except for the rhombohedral phase, where the complicated twinning effect in the sample may have caused the too small observed P_s [18]. For $KNbO_3$ in the tetragonal phase, the

calculated $P_s = 0.40$ C/m^2 is in good agreement with the experimental result of 0.40 C/m^2. We calculated P_s for PbTiO$_3$ in the tetragonal structures for two different temperatures; the resulting values are 1.04 C/m^2 at 295 K, and 0.74 C/m^2 at 700 K, to be compared with experimental values of 0.75 and 0.50 C/m^2, respectively [19]. We suspect these discrepancies may be related in part to cracking and charge leakage problems in the experiment [17].

The Born effective charge tensor reflects the effect of Coulomb interactions and is directly related to the LO-TO splitting. The dynamical matrix can be shown to take the form [20]

$$D_{\substack{mn\\\mu\nu}}(\mathbf{q}) = D_{\substack{mn\\\mu\nu}}^{(0)}(\mathbf{q}) + \frac{4\pi e^2}{\Omega} \frac{(\mathbf{Z}_m^* \cdot \hat{\mathbf{q}})_\mu (\mathbf{Z}_n^* \cdot \hat{\mathbf{q}})_\nu}{\epsilon_\infty(\mathbf{q})} , \quad (2)$$

where $\mathbf{q}$ is the wave vector, $\epsilon_\infty(\mathbf{q})$ is the optical macroscopic dielectric function, and $D^{(0)}$ is an analytic function of $\mathbf{q}$. The difference between the LO and TO frequencies for an ionic crystal arises from the last term in Eq. (2), which accounts for the effect of the macroscopic electric field which is only present for the LO modes.

We are specifically interested in the LO-TO splitting at $\mathbf{q} = 0$. The dynamical matrix $D^{(0)}(\mathbf{q} = 0)$ has been previously calculated in investigating the soft phonon modes [8]. We take experimental values for $\epsilon_\infty(0)$. The observed values in the visible light range [17] are extrapolated to the optical $\omega = 0$ limit using the dispersion relation $\epsilon - 1 = C/(\omega_0^2 - \omega^2)$, where C and ω_0 are constants. The resulting values of $\epsilon_\infty(0)$ are 5.24 (BaTiO$_3$), 5.18 (SrTiO$_3$), 5.81 (CaTiO$_3$), 4.69 (KNbO$_3$), 4.96 (NaNbO$_3$), and 8.64 (PbTiO$_3$). The fact that these experimental values are obtained for the cubic phase at high temperature, or for a lower-symmetry phase, introduces some uncertainty into the calculated LO mode frequencies. We could not find corresponding data for PbZrO$_3$ and BaZrO$_3$.

For the perfect cubic perovskite structure at $\mathbf{q} = 0$, there are 15 phonon modes: 3 acoustic modes, 4 LO modes, and 4 doubly degenerate TO modes. One pair of TO and LO modes are not split by the Coulomb interaction; not being infrared (IR) active, we do not consider them further. The calculated IR-active TO and LO mode frequencies are shown in Table II, together with experimental observed values. The experimental values quoted are either for the F_{1u} modes in the cubic structure, or the corresponding E modes in the tetragonal structure. The agreement with experimental values is typically within 5%–10%, which is very good for an *ab initio* calculation. The less satisfying agreement for PbTiO$_3$ and PbZrO$_3$ is partly due to the big difference between the experimental tetragonal phase and the theoretical cubic phase.

The eigenvector analysis shows that generally there is no correspondence between individual TO and LO phonon modes. For convenience we consider only modes of a given Cartesian polarization, say along $\hat{\mathbf{z}}$, for the remainder of this paper. The dynamical matrices for LO and TO modes at $\mathbf{q} = 0$ are then related by

$$D_{mn}^{\text{LO}} = D_{mn}^{\text{TO}} + \frac{4\pi e^2}{\Omega} \frac{Z_m^* Z_n^*}{\epsilon_\infty(0)} . \quad (3)$$

The correlation between the LO and TO modes can be measured by the matrix $c_{ij} = \langle \xi_i^{\text{TO}} | M | \xi_j^{\text{LO}} \rangle$, where $M_{mn} = M_m \delta_{mn}$ is the mass matrix and ξ_i are the IR-active mode eigenvectors. The c_{ij} matrix for KNbO$_3$ is typical:

$$c = \begin{pmatrix} 0.19 & 0.63 & 0.75 \\ 0.98 & 0.14 & 0.13 \\ 0.03 & 0.76 & 0.65 \end{pmatrix} , \quad (4)$$

where rows label TO modes and columns label LO modes. Note that c_{13} is the largest element in the first row, which means that the *softest TO mode (TO1) is most closely associated with the hardest LO mode (LO3)*.

TABLE II. Calculated IR-active optical phonon frequencies (cm^{-1}) in comparison with experimental values. Measured E modes of tetragonal structures are listed for BaTiO$_3$, PbTiO$_3$, and PbZrO$_3$. Imaginary frequencies indicate soft modes.

	TO1		TO2		TO3		LO1		LO2		LO3	
	Theor.	Expt.	Theor.	Expt.	Theor.	Expt.	Theor.	Expt.	Theor.	Expt.	Theor.	Expt.
BaTiO$_3$	178i		177	181[a]	468	487[a]	173	180[a]	453	468[a]	738	717[a]
SrTiO$_3$	41i		165	175[b]	546	545[b]	158	171[b]	454	474[b]	829	795[b]
CaTiO$_3$	153i		188		610		133		427		866	
KNbO$_3$	143i		188	198[c]	506	521[c]	183	190[c]	407	418[c]	899	826[c]
NaNbO$_3$	152i		115		556	535[d]	101		379	411[d]	928	876[d]
PbTiO$_3$	144i		121	210[e]	497	500[e]	104		410		673	750[e]
PbZrO$_3$	131i		63	221[f]	568	508[f]						
BaZrO$_3$	95	115[f]	193	210[f]	514	505[f]						

[a]T. Nakamura, Ferroelectrics **137**, 65 (1992).
[b]J.L. Servoin, Y. Luspin, and F. Gervais, Phys. Rev. B **22**, 5501 (1980).
[c]M.D. Fontana, G. Métrat, J.L. Servoin, and F. Gervais, J. Phys. C **17**, 483 (1984).
[d]F. Gervais, J.L. Servoin, J.F. Baumard, and F. Denoyer, Solid State Commun. **41**, 345 (1982).
[e]Reference [17].
[f]C.H. Perry, D.J. McCarthy, and G. Ruprecht, Phys. Rev. **138**, A1537 (1965).

TABLE III. The effective charges associated with IR-active TO modes. Last column: critical depolarization factor.

	$\bar{Z}$(TO1)	$\bar{Z}$(TO2)	$\bar{Z}$(TO3)	L_c
$BaTiO_3$	8.95	1.69	1.37	0.062
$SrTiO_3$	7.37	3.22	3.43	0.003
$CaTiO_3$	6.25	4.94	4.50	0.112
$KNbO_3$	8.58	1.70	4.15	0.040
$NaNbO_3$	6.95	2.32	5.21	0.071
$PbTiO_3$	7.58	4.23	3.21	0.083
$PbZrO_3$	4.83	4.86	4.30	
$BaZrO_3$	4.01	5.57	3.84	

This remarkable behavior is also clearly evident in the values of the mode effective charges, defined as $\bar{Z}_j^* = \sum_m M_m^{1/2} Z_m^* \xi_{jm}^{TO}$. If the last term of Eq. (3) did not cause any mixing of the mode eigenvectors, this value would directly reflect the LO-TO splitting. Table III lists the calculated mode effective charges for all 8 compounds. We find that $\bar{Z}^*$ for the soft mode is usually the largest, which means that the soft mode will couple most strongly with the **E** field. In fact, we find that if we construct an LO mode with an eigenvector identical to that of the soft TO mode (TO1), its frequency would generally lie between those of the LO2 and LO3 modes. The extreme case is $BaTiO_3$, for which the LO frequency associated with TO1 is 708 cm^{-1}, only 3% smaller than that of LO3. This giant LO-TO splitting reflects the importance of the Coulomb interaction. Most compounds have a large $\bar{Z}^*$ for more than one mode. These modes will be strongly mixed by the Coulomb interaction in going to the LO case. Since the LO and TO modes have quite different eigenvectors, any model that assumes a one-to-one correspondence between LO and TO modes would be highly unjustified for perovskite compounds.

The role of Coulomb interaction depends on the **E** field inside the material. With no external field, $\mathbf{E} = -4\pi L \mathbf{P}$, where L is the depolarization factor which depends on the geometry of the material ($L = 1/3$ for a sphere, $L = 0$ for a needle, and $L = 1$ perpendicular to a thin film). We calculate the critical depolarization factor L_c, above which the ferroelectric state becomes unstable. It is the value which makes the matrix

$$D_{mn}^{TO}(0) + L_c \frac{4\pi e^2}{\Omega} \frac{Z_m^* Z_n^*}{\epsilon_\infty(0)} \qquad (5)$$

have a second zero eigenvalue, besides that for translation. The calculated L_c's, listed in Table III, are found to be remarkably small. Thus, it is clear that electric-field effects will be critical and that the boundary conditions and/or domain structures will play a very important role in the occurrence of ferroelectricity. In other words, the ferroelectric state can only develop when the depolarization field is close to zero.

In conclusion, we calculate the effective charge ten-

sors Z^* for cubic perovskite materials ABO_3 using ultra-soft pseudopotentials and a preconditioned conjugate-gradient method. We find, for all the compounds studied, that $Z^*(B)$ and $Z^*(O)$ are anomalously large. The LO and TO phonon frequencies are calculated and found to be in good agreement with experimental observations. The giant LO-TO splittings which emerge from the calculation indicate the importance of Coulomb interactions, resulting in a remarkably small critical depolarization field and a great sensitivity of the ferroelectricity to the domain structure and boundary conditions.

* Permanent address: Biosym Technologies Inc., 9685 Scranton Rd., San Diego, CA 92122.

[1] M.E. Lines and A.M. Glass, *Principles and Applications of Ferroelectrics and Related Materials* (Clarendon Press, Oxford, 1977).

[2] J.D. Axe, Phys. Rev. **157**, 429 (1967).

[3] L.F. Mattheiss, Phys. Rev. B **6**, 4718 (1972).

[4] R.E. Cohen, Nature (London) **358**, 136 (1992).

[5] K.H. Weyrich and R. Siems, Jpn. J. Appl. Phys. **24**, Suppl. 24-2, 206 (1985).

[6] D.J. Singh and L.L. Boyer, Ferroelectrics **136**, 95 (1992).

[7] R.D. King-Smith and D. Vanderbilt, Ferroelectrics **136**, 85 (1992).

[8] R.D. King-Smith and D. Vanderbilt, Phys. Rev. B **49**, 5828 (1994).

[9] R.D. King-Smith and D. Vanderbilt, Phys. Rev. B **47**, 1651 (1993).

[10] R. Resta, M. Posternak, and A. Baldereschi, Phys. Rev. Lett. **70**, 1010 (1993).

[11] Ph. Ghosez, X. Gonze, and J. -P. Michenaud, in Proceedings of the 8th International Meeting on Ferroelectrics (to be published).

[12] D. Vanderbilt, Phys. Rev. B **41**, 7892 (1990).

[13] K. Laasonen, A. Pasquarello, R. Car, C. Lee, and D. Vanderbilt, Phys. Rev. B **47**, 10 142 (1993).

[14] T.A. Arias, M.C. Payne, and J.D. Joannopoulos, Phys. Rev. Lett. **69**, 1077 (1992).

[15] M.C. Payne, M.P. Teter, D.C. Allan, T.A. Arias, and J.D. Joannopoulos, Rev. Mod. Phys. **64**, 1045 (1992).

[16] W.A. Harrison, *Electronic Structure and the Properties of Solids* (Dover, New York, 1980).

[17] T. Mitsui *et al.*, *Oxides*, Landolt-Bornstein Numerical Data and Functional Relationships in Science and Technology, Group III, Vol. 16, Pt. a (Springer-Verlag, Berlin, 1981); E. Nakamura *et al.*, *ibid.* Group III, Vol. 28 (to be published).

[18] H.H. Wieder, Phys. Rev. **99**, 1161 (1955).

[19] V.G. Gavrilyachenko *et al.*, Fiz. Tverd. Tela **12**, 1532 (1970) [Sov. Phys. Solid State **12**, 1203 (1970)].

[20] R.M. Pick, M.H. Cohen, and R.M. Martin, Phys. Rev. B **1**, 910 (1970).

Phase Transitions in BaTiO₃ from First Principles

W. Zhong and David Vanderbilt

Department of Physics and Astronomy, Rutgers University, Piscataway, New Jersey 08855-0849

K. M. Rabe

Department of Applied Physics, Yale University, New Haven, Connecticut 06520
(Received 13 June 1994; revised manuscript received 4 August 1994)

We develop a first-principles scheme to study ferroelectric phase transitions for perovskite compounds. We obtain an effective Hamiltonian which is fully specified by first-principles ultrasoft pseudopotential calculations. This approach is applied to BaTiO₃, and the resulting Hamiltonian is studied using Monte Carlo simulations. The calculated phase sequence, transition temperatures, latent heats, and spontaneous polarizations are all in good agreement with experiment. The order-disorder versus displacive character of the transitions and the roles played by different interactions are discussed.

PACS numbers: 77.80.Bh, 61.50.Lt, 64.60.Cn, 64.70.–p

Because of their simple crystal structure, the cubic ferroelectric perovskites present a special opportunity for the development of a detailed theoretical understanding of the ferroelectric phase transition. However, even in BaTiO₃, a much-studied prototypical example of this class of compounds [1], many aspects of the phase behavior are far from simple. BaTiO₃ undergoes a succession of phase transitions, from the high-temperature high-symmetry cubic perovskite phase (Fig. 1) to slightly distorted ferroelectric structures with tetragonal, orthorhombic, and rhombohedral symmetry. There is increasing evidence that the cubic-tetragonal transition, at first thought to be of the simple displacive kind, may instead be better described as of the order-disorder type.

A comparison with the related cubic perovskites indicates that this and other aspects of the phase transformation behavior in BaTiO₃ are not universal, but rather must depend on details of the chemistry and structural energetics of the particular compound. Therefore, it is of the first
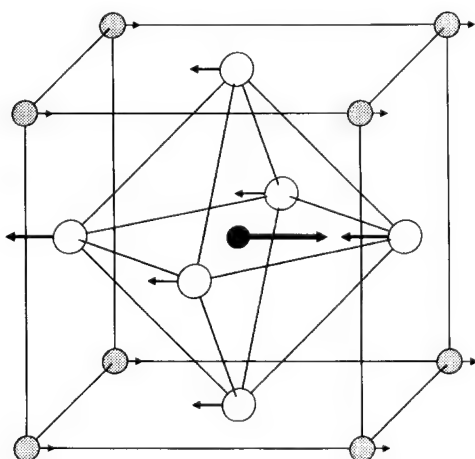

FIG. 1. The structure of cubic perovskite compounds BaTiO₃. Atoms Ba, Ti, and O are represented by shaded, solid, and empty circles, respectively. The areas of the vectors indicate the magnitudes of the displacements for a local mode polarized along $\hat{x}$.

importance to develop a microscopic theory of the relevant materials properties. The value of a microscopic approach has long been appreciated, but its realization was hindered by the difficulty of determining microscopic parameters for individual compounds. The forms of phenomenological model Hamiltonians [1–4] were limited by the available experimental data, leading to oversimplification and ambiguities in interpretation. For the perovskite oxides, empirical [5] and nonempirical pair potential methods [6] did not offer the high accuracy needed for the construction of realistic models. Recently, high quality first-principles calculations within the local density approximation (LDA) have been shown to provide accurate total-energy surfaces for perovskites [7–10]. While an *ab initio* molecular-dynamics simulation of the structural phase transition is not computationally feasible at present, the application of these first-principles methods can clearly form a foundation for the realistic study of the finite-temperature phase transitions.

In this paper, we pursue a completely first-principles approach to study the ferroelectric phase transitions in BaTiO₃. In particular, we (i) construct an effective Hamiltonian to describe the important degrees of freedom of the system [11,12], (ii) determine all the parameters of this effective Hamiltonian from high-accuracy *ab initio* LDA calculations [9,13,14], and (iii) carry out Monte Carlo (MC) simulations to determine the phase transformation behavior of the resulting system. We find the correct succession of phases, with transition temperatures and spontaneous polarization in reasonable agreement with experiment. Strain coupling is found to be crucial in producing the correct succession of low-symmetry phases. Finally, by analyzing the local distortions and phonon softening, we find the cubic-tetragonal transition in BaTiO₃ to be intermediate between the displacive and order-disorder limits.

Briefly, the effective Hamiltonian is constructed as follows. Since the ferroelectric transition involves only small structural distortions, we represent the energy surface by a Taylor expansion around the high-symmetry cubic

perovskite structure, including fourth-order anharmonic terms. Because the contribution to the partition function decays exponentially with increasing energy, we simplify this expansion by including only low energy distortions. Among all the possible phonon excitations, the long-wavelength acoustic modes (strain) and lowest transverse-optical phonon modes (soft modes) have the lowest energy. It is therefore our approximation to include only these two kinds of phonon excitations, thus reducing the number of degrees of freedom per unit cell from 15 to 6. This approximation could later be systematically improved, or entirely removed, by including higher-energy phonons.

It is straightforward to describe the strain degrees of freedom associated with the acoustic modes in terms of displacement vectors $\mathbf{v}_l$ associated with each unit cell l. In a similar manner, we introduce variables $\mathbf{u}_l$ to describe the amplitude of a "local mode" associated with cell l. The properly chosen local mode should reproduce the soft-mode phonon dispersion relation throughout the Brillouin zone, preserve the symmetry of the crystal, and minimize interactions between adjacent local modes. The local mode chosen for $BaTiO_3$ is shown in Fig. 1. The terms in our Taylor expansion of the energy in the variables $\{\mathbf{u}\}$ and $\{\mathbf{v}\}$ are organized as follows: (i) a soft-mode self-energy $E^{\text{self}}(\{\mathbf{u}\})$ containing intrasite interactions to quartic anharmonic order; (ii) a long-range dipole-dipole coupling $E^{\text{dpl}}(\{\mathbf{u}\})$ and a short-range (up to third neighbor) correction $E^{\text{short}}(\{\mathbf{u}\})$ to the intersite coupling, both at harmonic order; (iii) a harmonic elastic energy $E^{\text{elas}}(\{\mathbf{v}\})$; and (iv) an anharmonic strain–soft-mode coupling $E^{\text{int}}(\{\mathbf{u}\},\{\mathbf{v}\})$ containing Gruneisen-type interactions (i.e., linear in strain and quadratic in soft-mode variables). The cubic symmetry greatly reduces the number of expansion coefficients needed. All the expansion parameters are determined from highly accurate first-principles LDA calculations applied to supercells containing up to four primitive cells (20 atoms). The calculation of the needed microscopic parameters within LDA for $BaTiO_3$ has been made possible by the use of Vanderbilt ultrasoft pseudopotentials [13], which make large-scale calculations tractable at the high level of accuracy needed, and by the recent theory of polarization of King-Smith and Vanderbilt [15], which provides a convenient method of calculating the dipolar interaction strengths [14]. The details of the Hamiltonian, the first-principles calculations, and the values of the expansion parameters will be reported elsewhere [16].

We solve the Hamiltonian using Metropolis Monte Carlo simulations [17,18] on an $L \times L \times L$ cubic lattice with periodic boundary conditions. Since most energy contributions (except E^{dpl}) are local, we choose the single-flip algorithm and define one Monte Carlo sweep (MCS) as L^3 flip attempts.

The ferroelectric phase transition is very sensitive to hydrostatic pressure, or, equivalently, to lattice constant. The LDA-calculated lattice constants are typically 1% too small, and even this small error can lead to large errors

in the zero-pressure transition temperatures. The effect of this systematic error can largely be compensated by exerting a negative pressure that expands the lattice constant to the experimental value. For BaTiO3, we choose $P = -4.8$ GPa which gives the best overall agreement for the computed volumes for the four phases with their experimental values. The following simulations and analysis are for this pressure.

In our simulation, we concentrate on identifying the succession of different phases, determining the phase transition temperatures, and extracting qualitative features of the transitions. We also focus on identifying the features of the Hamiltonian which most strongly affect the transition properties. For these purposes, it is most convenient to monitor directly the behavior of the order parameter. In the case of the ferroelectric phase transition, this is just the polarization vector (or, equivalently, the soft-mode amplitude vector $\mathbf{u}$) averaged over the simulation cell. To avoid effects of possible rotation of the polarization vector and to identify the different phases clearly, we choose to accumulate the absolute values of the largest, middle, and smallest components of the averaged local-mode vector for each step, denoted by u_1, u_2, and u_3, respectively ($u_1 > u_2 > u_3$). The cubic (C), tetragonal (T), orthorhombic (O), and rhombohedral (R) phases are then characterized by zero, one, two, and three nonzero order-parameter components, respectively. As a reference, the average local-mode amplitude $u = \sum_i |\mathbf{u}_i|/N$ is also monitored. Here, $\mathbf{u}_i$ is the local mode vector at site i and N is the total number of sites.

Figure 2 shows the quantities u_1, u_2, u_3, and u as functions of temperature in a typical simulation for an $L = 12$ lattice. For clarity, we show only the cooling down process. The values are averaged over 7000 MCS's after the system reaches equilibrium, so that the typical fluctuation of order parameter components is less than 10%. We find that u_1, u_2, and u_3 are all very close to zero at high temperature. As the system cools down past 295 K, u_1 increases and becomes significantly larger than u_2 or u_3.
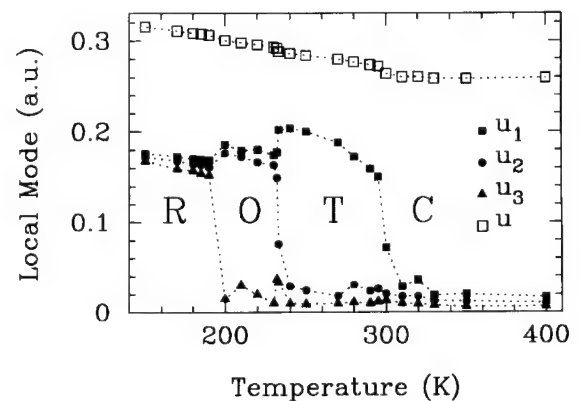
FIG. 2. The averaged largest, middle, and smallest components u_1, u_2, u_3 and amplitude u of local modes as a function of temperature in a cooling-down simulation of a $12 \times 12 \times 12$ lattice. The dotted lines are guides to the eyes.

This indicates the transition to the tetragonal phase. The homogeneous-strain variables confirm that the shape of the simulation cell becomes tetragonal. Two other phase transitions occur as the temperature is reduced further. The T-O transition occurs at 230 K (sudden increase of u_2) and the O-R transition occurs at 190 K (sudden increase of u_3). The shape of the simulation cell also shows the expected changes. The sequence of transitions exhibited by the simulation is the same as that observed experimentally.

The transition temperatures are located by careful cooling and heating sequences. We start our simulation at a high temperature and equilibrate in the cubic phase. The temperature is then reduced in small steps. At each temperature, the system is allowed to relax for 10 000 MCS's (increased to 25 000 and then to 40 000 MCS's close to the transition). After each transition is complete, the system is reheated slowly to detect any possible hysteresis. The calculated transition temperatures are shown in Table I. Simulations for three lattice sizes are performed; the error estimates in the table reflect the hysteretic difference between cooling and heating, which persists even after significant increase of the simulation time. The calculated transition temperatures are well converged with respect to system size, and are in good agreement with experiment. The saturated spontaneous polarization P_s in different phases can be calculated from the average local-mode variable. The results are also shown in Table I. We find almost no finite-size effect, and the agreement with experiment is very good for the O and T phases. The disagreement for the R phase may be due in part to twinning effects in the experimental sample [19].

One way to determine the order of the transition is to calculate the latent heat. An accurate determination of the latent heat would require considerable effort; here, we only try to provide good estimates. We approach the transition from both high-temperature and low-temperature sides until the point is reached where both phases appear equally stable. The difference of the average total energy is then the latent heat [20]. This estimate should be good as long as some hysteresis is present. The calculated latent heat (Table I) is in rough agreement with the rather scattered experimental data. We find that, taking into account finite-size effects, the latent heats for all three transitions are significantly nonzero, suggesting all transitions are first order. For the T-O and O-R transitions, this is consistent with Landau theory, which requires a transition to be first order when the subgroup relation does not hold between the symmetry groups below and above T_c.

Next, we investigate the extent to which the cubic-tetragonal transition can be characterized as order disorder or displacive. In real space, these possibilities can be distinguished by inspecting the distribution of the local-mode vector $\mathbf{u}_i$ in the cubic phase just above the transition. A displacive (microscopically nonpolar) or order-disorder (microscopically polar) transition should be characterized by a single-peak or double-peak struc-

TABLE I. Calculated transition temperatures T_c, saturated spontaneous polarization P_s, and estimated latent heat l, as a function of simulation cell size.

	Phase	$L = 10$	$L = 14$	Expt.[a]
T_c (K)	O-T	197 ± 3	200 ± 5	183
	T-O	230 ± 10	230 ± 10	278
	C-T	~ 290	297 ± 1	403
P_s (C/m^2)	R	0.43	0.43	0.33
	O	0.35	0.35	0.36
	T	0.28	0.28	0.27
l (J / mol)	O-R	50	60	33-60
	T-O	90	100	65-92
	C-T	$\cdots$	150	196-209

[a]T. Mitsui *et al., Landolt-Bornstein Numerical Data and Functional Relationships in Science and Technology (Springer-Verlag, 1981)*, NS, III/**16**.

ture, respectively. The distribution of u_x at $T = 320$ K is shown in Fig. 3. It exhibits a rather weak tendency to a double-peaked structure, indicating a transition which has some degree of order-disorder character. We also see indications of this in the u-T relation in Fig. 2; even in the cubic phase, the magnitude of the local-mode vector u is significantly nonzero and close to that of the rhombohedral phase. Although the components of the local modes change dramatically during the phase transition, u only changes slightly.

In reciprocal space, a system close to a displacive transition should show large and strongly temperature-dependent fluctuations of certain phonons (soft modes) confined to a small portion of the Brillouin zone (BZ). For an extreme order-disorder transition, on the other hand, one expects the fluctuations to be distributed over the whole BZ. For BaTiO$_3$, we calculated the average Fourier modulus of the soft T-O mode $\langle |u(q)|^2 \rangle$ at several temperatures just above the C-T transition. A strong increase of $\langle |u(q)|^2 \rangle$ as $T \to T_c$ would indicate phonon softening. As expected, we do observe this behavior for modes at Γ. While these modes become "hard" rather quickly along most directions away from Γ, they remain
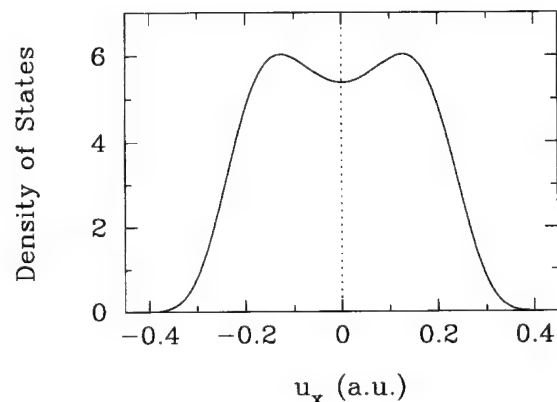

FIG. 3. The distribution of a Cartesian component of the local mode variable in the cubic phase at $T = 320$ K.

soft at least halfway to the BZ boundaries along the {100} directions, again indicating some order-disorder character.

Our theoretical approach allows us to investigate the roles played by different types of interaction in the phase transition. First, we study the effect of strain. The strain degrees of freedom were separated into local and homogeneous parts, representing finite- and infinite-wavelength acoustic modes, respectively. Both parts were included in the simulations. If we eliminate the local strain (while still allowing homogeneous strain), we find almost no change in the transition temperatures. This indicates that the effect of the short-wavelength acoustic modes may not be important for the ferroelectric phase transition. If the homogeneous strain is frozen, however, we find a direct cubic–rhombohedral phase transition, instead of the correct series of three transitions. This demonstrates the important role of homogeneous strain. Second, we studied the significance of the long-range Coulomb interaction in the simulation. To do this, we changed the effective charge of the local mode (and thus the dipole-dipole interaction), while modifying other parameters so that the frequencies of the zone-center and zone-boundary phonons remain in agreement with the LDA values. We found only a slight change (10%) of the transition temperatures when the dipole-dipole interaction strength doubled, but elimination of dipole-dipole interaction results in a dramatic change (in fact the ground state becomes a complex antiferroelectric structure). This result shows that it is essential to include the long-range interaction, although small inaccuracies in the calculated values of the effective charges or dielectric constants may not be very critical. On the other hand, our tests do indicate a strong sensitivity of the T_c's to any deviation of the fitted zone-center or zone-boundary phonon frequencies away from the LDA results. Thus, highly accurate LDA calculations do appear to be a prerequisite for an accurate determination of the transition temperatures.

Our approach opens several avenues for future study. Allowing a higher-order expansion of the energy surface might allow an accurate determination of the phase diagram. More extensive Monte Carlo simulations on larger systems, and with careful analysis of finite-size scaling, could provide more precise transition temperatures, free energies, and latent heats [21]. Finally, the theory would be more satisfying if the 1% underestimate of the lattice constant in the LDA calculation could be reduced or eliminated.

In conclusion, we have obtained the transition sequence, transition temperatures, and spontaneous polarizations of $BaTiO_3$ and found them to be in good agreement with experiment. We find that long-wavelength acoustic modes and long-range dipolar interactions both play an important role in the phase transition, while short-wavelength acoustic modes are not as relevant. The C-T

phase transition is not found to be well described as a simple displacive transition.

[1] M. E. Lines and A. M. Glass, *Principles and Applications of Ferroelectrics and Related Materials* (Clarendon Press, Oxford, 1977).

[2] M. T. Dove, A. P. Giddy, and V. Heine, Ferroelectrics **136**, 33 (1992).

[3] E. Pytte, Phys. Rev. B **5**, 3758 (1972).

[4] A. D. Bruce and R. A. Cowley, *Structural Phase Transitions* (Taylor & Francis, London, 1981).

[5] H. Bilz, G. Benedek, and A. Bussmann-Holder, Phys. Rev. B **35**, 4840 (1987), and references therein.

[6] G. Gordon and Y. S. Kim, J. Chem. Phys. **56**, 3122 (1972); L. L. Boyer et al., Phys. Rev. Lett. **54**, 1940 (1985); P. J. Edwardson et al., Phys. Rev. B **39**, 9738 (1989).

[7] R. E. Cohen and H. Krakauer, Phys. Rev. B **42**, 6416 (1990); R. E. Cohen and H. Krakauer, Ferroelectrics **136**, 65 (1992); R. E. Cohen, Nature (London) **358**, 136 (1992).

[8] D. J. Singh and L. L. Boyer, Ferroelectrics **136**, 95 (1992).

[9] R. D. King-Smith and D. Vanderbilt, Ferroelectrics **136**, 85 (1992).

[10] R. D. King-Smith and D. Vanderbilt, Phys. Rev. B **49**, 5828 (1994).

[11] K. M. Rabe and J. D. Joannopoulos, Phys. Rev. Lett. **59**, 570 (1987); Phys. Rev. B **36**, 6631 (1987).

[12] K. M. Rabe and U. V. Waghmare (to be published).

[13] D. Vanderbilt, Phys. Rev. B **41**, 7892 (1990).

[14] W. Zhong, R. D. King-Smith, and D. Vanderbilt, Phys. Rev. Lett. **72**, 3618 (1994).

[15] R. D. King-Smith and D. Vanderbilt, Phys. Rev. B **47**, 1651 (1993); D. Vanderbilt and R. D. King-Smith, Phys. Rev. B **48**, 4442 (1993).

[16] W. Zhong, D. Vanderbilt, and K. M. Rabe (unpublished).

[17] N. Metropolis et al., J. Chem. Phys. **21**, 1087 (1953).

[18] M. P. Allen and D. J. Tildesley, *Computer Simulation of Liquids* (Oxford, New York, 1990); K. Binder and D. W. Heermann, *Monte Carlo Simulation in Statistical Physics* (Springer-Verlag, Berlin, 1988); *The Monte Carlo Method in Condensed Matter Physics*, edited by K. Binder (Springer-Verlag, Berlin, 1992).

[19] H. H. Wieder, Phys. Rev. **99**, 1161 (1955).

[20] Under a *physical* applied pressure, the latent heat would be the change of enthalpy, not energy. If this were applied to our case of a *fictitious* pressure, the calculated latent heats would be approximately twice as large.

[21] J. Lee and J. M. Kosterlitz, Phys. Rev. Lett. **65**, 137 (1990); Phys. Rev. B **43**, 3265 (1991); A. M. Ferrenberg and R. H. Swendsen, Phys. Rev. Lett. **61**, 2635 (1988); **63**, 1195 (1989).

First-principles theory of ferroelectric phase transitions for perovskites: The case of BaTiO₃

W. Zhong and David Vanderbilt

Department of Physics and Astronomy, Rutgers University, Piscataway, New Jersey 08855-0849

K. M. Rabe

Department of Applied Physics, Yale University, New Haven, Connecticut 06520-8284

(Received 13 February 1995; revised manuscript received 19 April 1995)

We carry out a completely first-principles study of the ferroelectric phase transitions in BaTiO₃. Our approach takes advantage of two features of these transitions: the structural changes are small, and only low-energy distortions are important. Based on these observations, we make systematically improvable approximations which enable the parametrization of the complicated energy surface. The parameters are determined from first-principles total-energy calculations using ultrasoft pseudopotentials and a preconditioned conjugate-gradient scheme. The resulting effective Hamiltonian is then solved by Monte Carlo simulation. The calculated phase sequence, transition temperatures, latent heats, and spontaneous polarizations are all in good agreement with experiment. We find the transitions to be intermediate between order-disorder and displacive character. We find all three phase transitions to be of first order. The roles of different interactions are discussed.

I. INTRODUCTION

Because of their simple crystal structure, the perovskite oxides present a special opportunity for the development of a detailed theoretical understanding of the ferroelectric phase transition. Within this family of materials, one finds transitions to a wide variety of low-symmetry phases, including ferroelectric and antiferroelectric transitions. Both first- and second-order transitions are observed, with a full spectrum of transition behavior ranging from displacive to order-disorder behavior. The properties of BaTiO₃, a much-studied prototypical example of this class of compounds,[1] exemplify this rich behavior. BaTiO₃ undergoes a succession of first-order phase transitions, from the high-temperature high-symmetry cubic perovskite phase to slightly distorted ferroelectric structures with tetragonal, orthorhombic, and rhombohedral symmetry. There is increasing evidence that the cubic-to-tetragonal transition, at first thought to be of the simple displacive kind, may instead be better described as of the order-disorder type.

The variety exhibited by the perovskite oxides shows that the phase transformation behavior depends on details of the chemistry and structural energetics of each particular compound. Therefore, it is of the first importance to develop a microscopic theory of the materials properties which determine the ordering of the phases, the character and thermodynamic order of the transitions, and the transition temperatures. The value of a microscopic approach has long been appreciated, but its realization was hindered by the difficulty of determining microscopic parameters for individual compounds. The forms of phenomenological model Hamiltonians[1-4] were limited by the available experimental data, leading to oversimplification and ambiguities in interpretation.

For the perovskite oxides, empirical[5] and nonempirical pair potential methods[6] did not offer the high accuracy needed for the construction of realistic models.

First-principles density-functional calculations offer an attractive approach for enhancing our microscopic understanding of perovskites and other ferroelectrics. The all-electron full-potential linearized-augmented-plane-wave (FLAPW) method has been used by several groups to study ferroelectricity in perovskites within the local density approximation (LDA).[7,8] Recently, King-Smith and Vanderbilt performed a systematic study of structural and dynamical properties and energy surfaces for eight common perovskites,[9,10] using the first-principles ultrasoft pseudopotential method and the LDA. These calculations demonstrate that ferroelectricity in the perovskites reflects a delicate balance between long-range electrostatic forces which favor the ferroelectric state and short-range repulsions which favor the cubic phase. While constrained to calculations of zero-temperature properties, these calculations yield correct predictions of ground state structures and the occurrence of ferroelectric phases for certain materials. They show that high-quality LDA calculations can provide considerable insight into the nature of the total-energy surface in the perovskites. For further insight into the energetics of ferroelectric compounds, the polarization generated by various distortions can be studied directly, using a recent first-principles method by King-Smith and Vanderbilt.[11] This approach has been applied to the investigation of the zone-center phonons in the common perovskite oxides.[12]

The application of these first-principles methods can clearly form a foundation for the realistic study of the finite-temperature phase transitions. While an *ab initio* molecular-dynamics simulation of the structural phase transition is not computationally feasible at present, we

pursue an alternative first-principles approach to study ferroelectric phase transitions and demonstrate its application to BaTiO$_3$. In particular, we (i) construct an effective Hamiltonian to describe the important degrees of freedom of the system,[13,14] (ii) determine all the parameters of this effective Hamiltonian from high-accuracy *ab initio* LDA calculations,[9,12,15] and (iii) carry out Monte Carlo (MC) simulations to determine the phase transformation behavior of the resulting system. An abbreviated presentation of this work has already appeared in Ref. 16.

The remainder of this paper is organized as follows. In Sec. II, we go through the detailed procedure for the construction of the effective Hamiltonian and give the explicit formula. In Sec. III, we describe our first-principles calculations and the determination of the expansion parameters in the Hamiltonian. The technical details of the Monte Carlo simulation are presented in Sec. IV. In Sec. V, we report our calculated transition temperatures, order parameters, and phase diagram, as well as thermodynamic order and nature of the phase transitions. The role of different interactions in determining the phase transition behavior is also discussed. Section VI concludes the paper.

II. CONSTRUCTION OF THE HAMILTONIAN

A. Approximations and local modes

The central quantity for studying the equilibrium properties of a system at finite temperature is its partition function. This can be determined from the energy surface, i.e., the total potential energy as a functional of the atomic coordinates. Since the contribution to the partition function decreases exponentially with increasing energy, it is possible to obtain an accurate partition function for low-temperature applications from a simplified energy surface including only low-energy configurations. Our goal is to construct a parametrized Hamiltonian which (i) is *ab initio*, involving no empirical or semiempirical input; (ii) results in an accurate partition function for the temperature range of interest; (iii) is fully specified by a few *ab initio* total-energy calculations; and (iv) involves only approximations that are systematically improvable and removable.

Our first fundamental approximation is to use an energy surface represented by a low-order Taylor expansion. Both experiments and first-principles total-energy calculations suggest that the ferroelectric (FE) phase transition involves only very small atomic displacements and strain deformations from the equilibrium cubic structure. It is reasonable to assume that all the atomic configurations with significant contributions to the partition function would be close to this cubic structure in the temperature range of interest. Thus, it is natural to represent the energy surface by a Taylor series in the displacements from the cubic structure. We include up to fourth-order terms in our expansion; this is clearly a minimum, since ferroelectricity is intrinsically an anharmonic

phenomenon. By including higher-order terms, this approximation could later be systematically improved.

It is convenient to describe the small distortions from the cubic structure in terms of the 3 acoustic and 12 optical normal-mode coordinates per k point. While this could be regarded as only a change of basis, it motivates our second fundamental approximation, which is to restrict the expansion to include only low-energy distortions. To achieve this separation, we note that both experimentally measured and LDA-calculated phonon dispersion relations[1,12] show that only the lowest TO modes (soft modes) and long-wavelength acoustic phonons (strain variables) make significant contributions to the phonon density of states at low energy. Experimental studies also suggest that the FE phase transitions are accompanied by a softening of the lowest TO mode and the appearance of a strain. All other phonons are hardly affected by the transitions. It is then our second approximation to express the energy surface only as a function of the soft-mode amplitudes and strain. This approximation reduces the number of degrees of freedom per cell from 15 to 6, and greatly reduces the number of interaction parameters needed. If necessary, this approximation could later be relaxed by including additional modes.

It is convenient to describe the soft mode over the whole Brillouin zone (BZ) in terms of a collective motion of "local modes," just as one describes an acoustic phonon in terms of a collective displacement of individual atoms. However, there is more than one choice of local mode which will generate the same soft mode throughout the BZ; an intelligent choice can simplify the Hamiltonian and reduce the number of calculations needed.[17] First, the local mode should be as symmetric as possible, so as to minimize the number of expansion parameters needed. Second, the interactions between local modes at different sites are more difficult to treat than their on-site energy, and so the local mode should be chosen so as to minimize intersite interactions. For perovskite ABO_3 compounds, the highest symmetry is achieved by centering the local mode on either atom A or B. In the case of BaTiO$_3$, the Ti-O bond is much stronger than the Ba-O bond and the motion of the Ti is more important in the FE transition; so we choose the local mode which is centered on the Ti atom.

The soft zone-center ($\mathbf{k}=0$) FE mode in BaTiO$_3$ is a Γ_{15} mode which can be characterized by the four parameters ξ_A, ξ_B, $\xi_{O\parallel}$, and $\xi_{O\perp}$ (for a mode polarized along the jth Cartesian direction, these refer to the displacements of the A atom, the B atom, the O atom that form a B-O bond along direction j and the other two O atoms, respectively). We take the corresponding local mode to consist of a motion of the central A atom by amount ξ_A, the eight neighboring B atoms by amounts $\xi_B/8$, and the six neighboring O atoms by amounts $\xi_{O\parallel}/2$ or $\xi_{O\perp}/2$, along the jth Cartesian direction. This mode is illustrated in Fig. 1 of Ref. 16; its amplitude is denoted u_j. An arbitrary $k = 0$ soft mode can then be realized as a linear superposition of these local modes having identical amplitudes $(u_x, u_y, u_z) = \mathbf{u}$ in every cell.

The harmonic interactions between the local-mode am-

plitudes $\mathbf{u}_i$ connecting neighboring cells i must be chosen to reproduce the harmonic behavior of the soft-mode branch throughout the BZ. Long-range Coulomb forces are known to play an important part in these interactions; they are characterized in terms of the calculated Born (or "transverse") effective charges.[12] Thus, the harmonic intersite interactions are represented by a sum of two contributions: an infinite-range piece that is precisely the interaction of point dipoles whose magnitude is given by the Born effective charge and corrections which we take to be of covalent origin and therefore local.

To be completely general, anharmonic intercell interactions between neighboring $\mathbf{u}_i$ would likewise have to be included. Instead, we include only *on-site* anharmonic interactions, which are chosen in such a way that the anharmonic couplings for $k = 0$ modes of the real system are correctly reproduced. This "local anharmonicity approximation" is an important feature which helps make our scheme tractable and efficient. To go beyond this approximation, one could carry out a careful series of frozen-phonon LDA calculations on supercells to determine anharmonic couplings at other points in the BZ. However, past experience has shown that calculations of this kind are very cumbersome because of the large number of parameters which has to be determined.[18]

With these approximations, our Hamiltonian consists of five parts: a local-mode self-energy, a long-range dipole-dipole interaction, a short-range interaction between soft modes, an elastic energy, and an interaction between the local modes and local strain. Symbolically,

$$
\begin{aligned}
E^{\mathrm{tot}} &= E^{\mathrm{self}}(\{\mathbf{u}\}) + E^{\mathrm{dpl}}(\{\mathbf{u}\}) + E^{\mathrm{short}}(\{\mathbf{u}\}) \\
&\quad + E^{\mathrm{elas}}(\{\eta_l\}) + E^{\mathrm{int}}(\{\mathbf{u}\}, \{\eta_l\}) ,
\end{aligned} \tag{1}
$$

where $\mathbf{u}$ is the local soft-mode amplitude vector and η_l is the six-component local strain tensor in Voigt notation ($\eta_1 = e_{11}$, $\eta_4 = 2e_{23}$). In the following subsections, we present the explicit formulas for these five contributions.

B. Local mode self energy

The first term is

$$
E^{\mathrm{self}}(\{\mathbf{u}\}) = \sum_i E(\mathbf{u}_i) , \tag{2}
$$

where $E(\mathbf{u}_i)$ is the energy of an isolated local mode at cell $\mathbf{R}_i$ with amplitude $\mathbf{u}_i$, relative to that of the perfect cubic structure. To describe the FE phase, $E(\mathbf{u}_i)$ must contain

anharmonic as well as harmonic contributions. Since the reference structure is cubic, only even-order terms can enter; we choose to truncate at fourth order. Symmetry considerations then require that it take the form

$$
E(\mathbf{u}_i) = \kappa_2 u_i^2 + \alpha u_i^4 + \gamma(u_{ix}^2 u_{iy}^2 + u_{iy}^2 u_{iz}^2 + u_{iz}^2 u_{ix}^2) , \tag{3}
$$

where $u_i = |\mathbf{u}_i|$ and κ_2, α, and γ are expansion parameters to be determined from first-principles calculations.

C. Dipole-dipole interaction

The second term in the effective Hamiltonian represents long-range interactions between local modes. Only dipole-dipole interactions are considered, since higher-order terms tend to be of short range and their effect will be included in the short-range contribution $E^{\mathrm{short}}(\{\mathbf{u}\})$. The dipole moment associated with the local mode in cell i is $\mathbf{d}_i = Z^* \mathbf{u}_i$. Here, Z^* is the Born effective charge for the soft mode, which can be obtained as

$$
Z^* = \xi_A Z_A^* + \xi_B Z_B^* + \xi_{\mathrm{O}\parallel} Z_{\mathrm{O}\parallel}^* + 2\xi_{\mathrm{O}\perp} Z_{\mathrm{O}\perp}^* \tag{4}
$$

from the eigenvector of the soft mode, once the Born effective charges for the ions are known.[12] In atomic units (energy in Hartree), we have

$$
E^{\mathrm{dpl}}(\{\mathbf{u}\}) = \frac{Z^{*2}}{\epsilon_\infty} \sum_{i<j} \frac{\mathbf{u}_i \cdot \mathbf{u}_j - 3(\hat{\mathbf{R}}_{ij} \cdot \mathbf{u}_i)(\hat{\mathbf{R}}_{ij} \cdot \mathbf{u}_j)}{R_{ij}^3} . \tag{5}
$$

Here, ϵ_∞ is the optical dielectric constant of the material, $R_{ij} = |\mathbf{R}_{ij}|$, $\mathbf{R}_{ij} = \mathbf{R}_i - \mathbf{R}_j$, and $\hat{\mathbf{R}}_{ij} = \mathbf{R}_{ij}/R_{ij}$.

In practice, Eq. (5) is not directly useful for three-dimensional systems with periodic boundary conditions; instead, we use an Ewald construction to evaluate E^{dpl}. We effectively terminate the sum in such a way that the $k = 0$ modes of the supercell will represent physical TO(Γ) modes. For a TO mode, the induced depolarization electric field is zero; from the point of view of the dipole sum, it is as though the material were surrounded by a layer of metal. In the Ewald construction, this is equivalent to setting the surface terms to zero.[19] Under these conditions and choosing the decay λ of the Gaussian charge packets to be small enough so that the real-space summation can be entirely neglected, we have

$$
E^{\mathrm{dpl}} = \frac{2Z^{*2}}{\epsilon_\infty} \left[\frac{\pi}{\Omega_c} \sum_{\mathbf{G}\neq 0} \frac{1}{|\mathbf{G}|^2} \exp\left(-\frac{|\mathbf{G}|^2}{4\lambda^2}\right) \sum_{ij} (\mathbf{G} \cdot \mathbf{u}_i)(\mathbf{G} \cdot \mathbf{u}_j) \cos(\mathbf{G} \cdot \mathbf{R}_{ij}) - \sum_i \frac{\lambda^3 u_i^2}{3\sqrt{\pi}} \right] , \tag{6}
$$

where Ω_c is the cell volume and $\mathbf{G}$ is the reciprocal lattice vector.

Because of its long-range nature, the calculation of E^{dpl} is the most time-consuming part of our Monte Carlo simulations. It is thus worth some special treatment to reduce the computational load. In principle, the term R_{ij} appearing in the denominator of Eq. (5) should be strain dependent. However, as we have chosen to expand the intersite interactions between local modes only up to harmonic order, it is consistent to ignore this effect, since strain-induced changes of the dipole-dipole interaction will enter only at higher order. This is equivalent to fixing the

reciprocal lattice vectors $\mathbf{G}$ and all the atomic position vectors $\mathbf{R}_i$. The dipole energy can then be written as

$$E^{\mathrm{dpl}} = \sum_{ij,\alpha\beta} Q_{ij,\alpha\beta} u_{i,\alpha} u_{j,\beta}, \tag{7}$$

with

$$Q_{ij,\alpha\beta} = \frac{2Z^{*2}}{\epsilon_\infty} \left[\frac{\pi}{\Omega_c} \sum_{\mathbf{G}\neq 0} \frac{1}{|\mathbf{G}|^2} \exp\left(-\frac{|\mathbf{G}|^2}{4\lambda^2} \right) \cos(\mathbf{G}\cdot\mathbf{R}_{ij}) G_\alpha G_\beta - \frac{\lambda^3}{3\sqrt{\pi}} \delta_{\alpha\beta}\delta_{ij} \right] . \tag{8}$$

Here, α and β denote Cartesian components. The matrix Q is thus treated as a constant; it is calculated once and for all, and stored for later calculation of the dipole energy. This strategy increases the computational efficiency by at least one order of magnitude.

D. Short-range interaction

$E^{\mathrm{short}}(\{\mathbf{u}\})$ is the energy contribution due to the short-range interactions between neighboring local modes, with dipole-dipole interactions excluded. This contribution stems from differences of the short-range repulsion and electronic hybridization between two adjacent local modes and two isolated local modes. Together with the dipole-dipole interaction, this interaction determines the soft-mode energy away from the zone center. Expanded up to second order, it can be written as

$$E^{\mathrm{short}}(\{\mathbf{u}\}) = \frac{1}{2} \sum_{i\neq j} \sum_{\alpha\beta} J_{ij,\alpha\beta} u_{i\alpha} u_{j\beta} . \tag{9}$$

The coupling matrix $J_{ij,\alpha\beta}$ is a function of $\mathbf{R}_{ij}$ and should decay very fast with increasing $|\mathbf{R}_{ij}|$. Here, we consider the short-range interaction up to third nearest neighbor (NN), whose local mode shares atoms with the local mode on the origin. Local modes between further neighbors involve displacements of atoms at least two hops away (in tight-binding language) and their core-core repulsion or hybridization should be much less important than the dipole-dipole interaction which is taken care of in E^{dpl}.

The interaction matrix $J_{ij,\alpha\beta}$ can be greatly simplified by symmetry. For a cubic lattice, we have

first NN : $J_{ij,\alpha\beta} = (j_1 + (j_2 - j_1)|\hat{R}_{ij,\alpha}|)\delta_{\alpha\beta}$;

second NN : $J_{ij,\alpha\beta} = (j_4 + \sqrt{2}(j_3 - j_4)|\hat{R}_{ij,\alpha}|)\delta_{\alpha\beta}$
$\qquad\qquad + 2j_5 \hat{R}_{ij,\alpha}\hat{R}_{ij,\beta}(1-\delta_{\alpha\beta})$;

third NN : $J_{ij,\alpha\beta} = j_6\delta_{\alpha\beta} + 3j_7 \hat{R}_{ij,\alpha}\hat{R}_{ij,\beta}(1-\delta_{\alpha\beta})$,

$$\tag{10}$$

where $\hat{R}_{ij,\alpha}$ is the α component of $\mathbf{R}_{ij}/R_{ij}$. So we have only seven interaction parameters for a cubic lattice. The coefficients $j_1, j_2, ..., j_7$ in the above equations have physical meanings that are sketched schematically in Fig. 1. For example, j_1 represents the interaction strength of "π"-like interactions between first neighbors.

E. Elastic energy

We will describe the state of elastic deformation of the BaTiO$_3$ crystal using local strain variables $\eta_l(\mathbf{R}_i)$, where the Voigt convention is used ($l = 1,...,6$) and $\mathbf{R}_i$ labels a cell center (Ti) site. In fact, the six variables per unit cell $\{\eta_l(\mathbf{R}_i)\}$ are not independent, but are obtained from three independent displacement variables per unit cell. In our analysis, these are taken as the dimensionless displacements $\mathbf{v}(\mathbf{R}_i)$ (in units of the lattice constant a) defined at the unit cell corner (Ba) positions $\mathbf{R}_i + (a/2, a/2, a/2)$. In terms of these, the *inhomogeneous* strain variables $\eta_{I,l}(\mathbf{R}_i)$ are defined in the next subsection. Because of our use of a periodic supercell in the Monte Carlo simulations, however, homogeneous strain deformations are not included in the configuration space $\{\mathbf{v}(\mathbf{R}_i)\}$. Therefore, we introduce six additional *homogeneous* strain components $\eta_{H,l}$ to allow the simulation cell to vary in shape. The total elastic energy is expanded to quadratic order as

$$E^{\mathrm{elas}}(\{\eta_l\}) = E_I^{\mathrm{elas}}(\{\eta_{I,l}\}) + E_H^{\mathrm{elas}}(\{\eta_{H,l}\}) , \tag{11}$$

where the homogeneous strain energy is simply given by

$$E_H^{\mathrm{elas}}(\{\eta_{H,l}\}) = \frac{N}{2} B_{11}(\eta_{H,1}^2 + \eta_{H,2}^2 + \eta_{H,3}^2)$$
$$+ N B_{12}(\eta_{H,1}\eta_{H,2} + \eta_{H,2}\eta_{H,3} + \eta_{H,3}\eta_{H,1})$$
$$+ \frac{N}{2} B_{44}(\eta_{H,4}^2 + \eta_{H,5}^2 + \eta_{H,6}^2). \tag{12}$$
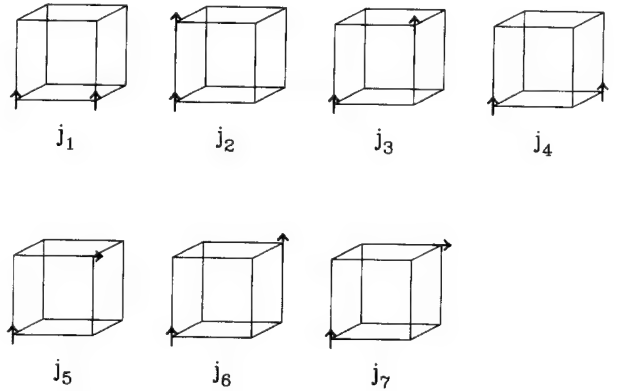

FIG. 1. The independent intersite interactions corresponding to the parameters j_1, j_2 (first neighbor), j_3, j_4, j_5 (second neighbor), and j_6 and j_7 (third neighbor).

Here B_{11}, B_{12}, and B_{44} are the elastic constants expressed in energy units ($B_{11} = a^3 C_{11}$, etc.), and N is the number of primitive cells in the supercell.

Rather than use an expression like (12) for the inhomogeneous strain energy, we have found it preferable to express this part directly in terms of the $\mathbf{v}(\mathbf{R}_i)$.[20] This approach keeps the acoustic phonon frequencies well behaved throughout the Brillouin zone. To satisfy requirements of invariance under translations and rotations of the crystal as a whole, the energy is expanded in scalar products of differences between the $\mathbf{v}(\mathbf{R}_i)$. The cubic crystal symmetry leads to a great reduction of the independent parameters in the expansion. The energies of the long-wavelength strain deformations can be reproduced by an expansion of the form

$$
\begin{aligned}
E_I^{\text{elas}} = \sum_i \Big\{ &\gamma_{11}[v_x(\mathbf{R}_i) - v_x(\mathbf{R}_i \pm \mathbf{x})]^2 \\
&+ \gamma_{12}[v_x(\mathbf{R}_i) - v_x(\mathbf{R}_i \pm \mathbf{x})][v_y(\mathbf{R}_i) - v_y(\mathbf{R}_i \pm \mathbf{y})] \\
&+ \gamma_{44}[v_x(\mathbf{R}_i) - v_x(\mathbf{R}_i \pm \mathbf{y}) + v_y(\mathbf{R}_i) \\
&- v_y(\mathbf{R}_i \pm \mathbf{x})]^2 + \text{cyclic permutations} \Big\} ,
\end{aligned}
\tag{13}
$$

corresponding to bond stretching, bond correlation, and bond bending, respectively. Here, $\mathbf{x} \equiv a\hat{\mathbf{x}}$, $\mathbf{y} \equiv a\hat{\mathbf{y}}$, $\mathbf{z} \equiv a\hat{\mathbf{z}}$, and $\pm$ indicates multiple terms to be summed. The γ coefficients are related to the elastic constants by $\gamma_{11} = B_{11}/4$, $\gamma_{12} = B_{12}/8$, and $\gamma_{44} = B_{44}/8$.

F. Elastic-mode interaction

To describe the coupling between the elastic deformations and the local modes, we use the on-site interaction

$$
E^{\text{int}}(\{\mathbf{u}\}, \{\eta_l\}) = \frac{1}{2} \sum_i \sum_{l\alpha\beta} B_{l\alpha\beta} \eta_l(\mathbf{R}_i) u_\alpha(\mathbf{R}_i) u_\beta(\mathbf{R}_i) .
\tag{14}
$$

As a result of cubic symmetry, there are only three independent coupling constants $B_{l\alpha\beta}$:

$$
\begin{aligned}
B_{1xx} &= B_{2yy} = B_{3zz} , \\
B_{1yy} &= B_{1zz} = B_{2xx} = B_{2zz} = B_{3xx} = B_{3yy} , \\
B_{4yz} &= B_{4zy} = B_{5xz} = B_{5zx} = B_{6xy} = B_{6yx} .
\end{aligned}
$$

The strain contains both homogeneous and inhomogeneous parts. $\eta_l(\mathbf{R}_i) = \eta_{H,l}(\mathbf{R}_i) + \eta_{I,l}(\mathbf{R}_i)$. The latter are expressed in terms of the local displacement vectors $\mathbf{v}$ as follows. We first define the six average differential displacements associated with site $\mathbf{R}_i$ as

$$
\Delta v_{xx} = \sum_{\mathbf{d}=0,\mathbf{y},\mathbf{z},\mathbf{y}+\mathbf{z}} [v_x(\mathbf{R}_i - \mathbf{d} - \mathbf{x}) - v_x(\mathbf{R}_i - \mathbf{d})] ,
$$

$$
\Delta v_{xy} = \sum_{\mathbf{d}=0,\mathbf{y},\mathbf{z},\mathbf{y}+\mathbf{z}} [v_y(\mathbf{R}_i - \mathbf{d} - \mathbf{x}) - v_y(\mathbf{R}_i - \mathbf{d})] ,
$$

and their cyclic permutations, recalling that $\mathbf{v}(\mathbf{R}_i)$ is associated with position $\mathbf{R}_i + (a/2, a/2, a/2)$. Then $\eta_{I,1}(\mathbf{R}_i) = \Delta v_{xx}/4$, $\eta_{I,4}(\mathbf{R}_i) = (\Delta v_{yz} + \Delta v_{zy})/4$, etc.

III. FIRST-PRINCIPLES CALCULATIONS

We have shown that, with the two approximations we made, the total-energy functional of the perovskite system is fully specified by a set of parameters. These parameters can be obtained from first-principles calculations. We use density-functional theory within the local density approximation (LDA). The technical details and convergence tests of the calculations can be found in Refs. 9, 10. The most important feature of the calculations is the Vanderbilt ultrasoft pseudopotential,[15] which allows a low-energy cutoff to be used for first-row elements. This makes high-accuracy large-scale calculations of materials involving oxygen and $3d$ transition metal elements affordable. The ultrasoft pseudopotential also allows for exceptionally transferable pseudopotentials. It ensures that all-electron atom and pseudoatom scattering properties agree over a very large energy range and preserves the chemical hardness of the atom. A generalized Kohn-Sham functional is directly minimized using a preconditioned conjugate gradient method.[10,21,22] We use a (6,6,6) Monkhorst-Pack k-point mesh[23] for single-cell calculations, i.e., 216 k points in the full Brillouin zone (FBZ). For supercell calculations, the k mesh is kept the same to minimize errors due to the k-point sampling. Therefore, a smaller number of k points is used because of the smaller FBZ.

We start with the construction of the local-mode vectors. All the eigenvalues and eigenvectors of the force-constant matrix at $k = 0$ for the cubic $BaTiO_3$ structure are calculated from frozen-phonon calculations, as in Ref. 10. The mode with imaginary frequency is identified as the soft mode. The soft-mode eigenvector has been reported previously[10] as $\xi_{\text{Ba}} = 0.20$, $\xi_{\text{Ti}} = 0.76$, $\xi_{\text{O}\|} = -0.53$, and $\xi_{\text{O}\perp} = -0.21$. The local mode is then constructed from it using the scheme proposed in Sec. II A.

Determination of many of the parameters in the effective Hamiltonian involves only calculations for zone-center distortions. These parameters have been reported previously.[10,12] They include the fourth-order terms of on-site energy α and γ; the elastic constants B_{11}, B_{12}, B_{44}; and the on-site elastic-mode interaction parameters $B_{1xx}, B_{1yy}, B_{4yz}$. The mode effective charge Z^* of Eq. (4) is calculated from the values $Z_A^*=2.75$, $Z_B^*=7.16$, $Z_{\text{O}\|}^*=-5.69$, and $Z_{\text{O}\perp}^*=-2.11$ published in Ref. 12. (The resulting value $Z^*=9.96$ is slightly different from the one given in Ref. 12; there, the eigenvector of the *dynamical* matrix, not the *force-constant* matrix, was used.) We use the experimental value $\epsilon_\infty = 5.24$ of the optical dielectric constant, since for this quantity, the LDA seems not to be a well-justified approximation, while exact density-functional theory results are not accessible. We find, however, that the effect of a small inaccuracy in the dielectric constant affects thermodynamic properties such as transition temperatures only slightly.

The second-order energy parameter κ for zone-center distortions is a linear combination of the local-mode self-energy parameter κ_2, the intersite interactions j_i, and the dipole-dipole interaction. The calculations of intersite interaction parameters involve determination of the
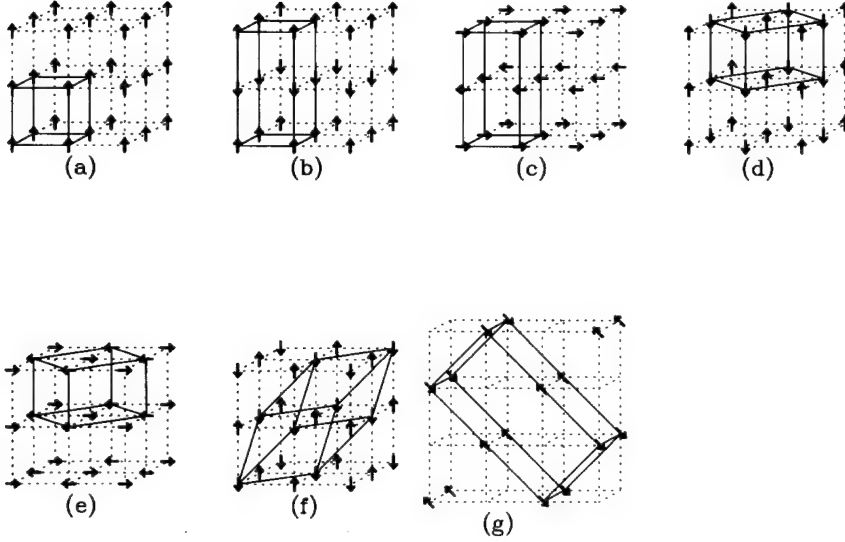
FIG. 2. The local-mode arrangements for which first-principles total-energy calculations were performed to determine the intersite interaction parameters. The arrangements can be labeled by the wave vector $\mathbf{k}$ and a polarization vector ($\hat{\mathbf{p}}$). The arrows represent local-mode vectors. The dotted lines indicate the unit cells of the simple cubic lattice. The solid lines show the supercells used in the calculations. (a) Γ, $\hat{\mathbf{p}} = \hat{\mathbf{z}}$; (b) X, $\hat{\mathbf{p}} = \hat{\mathbf{z}}$; (c) X, $\hat{\mathbf{p}} = \hat{\mathbf{x}}$; (d) M, $\hat{\mathbf{p}} = \hat{\mathbf{z}}$; (e) M, $\hat{\mathbf{p}} = \hat{\mathbf{x}}$; (f) R, $\hat{\mathbf{p}} = \hat{\mathbf{z}}$; (g) four-cell calculation.

energy for distortions at the zone-boundary k points $X = (\pi/a,0,0)$, $M = (\pi/a,\pi/a,0)$, and $R = (\pi/a,\pi/a,\pi/a)$, where a is the lattice constant. Five frozen-phonon calculations on doubled unit cells are sufficient to extract all the information available from these k points. The arrangements of the local-mode vectors for each case, as well as for the zone-center distortion at $\Gamma=(0,0,0)$, are shown in Fig. 2. The actual ionic configurations are constructed by superpositions of displacements associated with adjacent local modes. For example, letting u be the amplitude of the Ti-centered local mode defined in Sec. II A, the displacement of the Ti atoms is just $u\xi_{\text{Ti}}$ in Fig. 2(a) and $\pm u\xi_{\text{Ti}}$ in Fig. 2(b), while Ba is affected by eight neighboring local modes so that its displacement is $8u\xi_{\text{Ba}}/8 = u\xi_{\text{Ba}}$ in Fig. 2(a) and 0 in Fig. 2(b).

The above five doubled-cell calculations can be used to determine the parameters j_1, j_2, j_3, j_4, and j_6. The determination of $j_5 + 2j_7$ requires a four-cell calculation involving 20 atoms with low symmetry [Fig. 2(g)]. Table I lists the energy expressions for all the configurations calculated in terms of the quadratic expansion parameters.

A further decomposition of j_5 and j_7 would require an expensive eight-cell calculation. Furthermore, the interaction parameter j_7 is the third nearest-neighbor interaction and is thus presumably not very important. This argument is justified by our Monte Carlo simulations which

show that the calculated transition temperature is insensitive to different decompositions of j_5 and j_7. This prompts us to make an approximate decomposition based on a simple physical argument: We expect the interaction to be smallest for two interacting local modes oriented such that reversing the relative sign of the vectors produces the least change of bond lengths. Applied to third nearest neighbors, this argument implies $j_6 - 2j_7 = 0$, thus fixing the value of j_7.

The resulting interaction parameters are shown in Table II, together with other parameters published previously. It may be surprising to see that the on-site κ_2 is positive, while the cubic structure is known to be unstable against $k = 0$ distortion. The cubic structure is thus stable against forming an isolated local mode; instability actually comes from the intersite interactions between local modes. To be more precise, we find that it is the long-range Coulomb (dipole-dipole) interaction which makes the ferroelectric state favorable. If we turn off the dipole-dipole interaction by setting the effective charge $Z^* = 0$, we find that the ferroelectric instability disappears. This is consistent with the previous point of view that long-range Coulomb forces favor the ferroelectric state, while short-range repulsions favor the nonpolar cubic state.

From Table II, we see that the intersite interaction parameters decay very fast with increasing distance, indicating the short-range nature of the intersite interactions after the long-range Coulomb interactions have been separated out. The ratio of the magnitudes of the strongest

TABLE I. The energy per five-atom unit cell (excluding the dipole energy) in terms of intersite interaction parameters of Fig. 2, for configurations shown in Fig. 3.

Configuration	Expression
(a)	$\kappa_2 + 2j_1 + j_2 + 4j_3 + 2j_4 + 4j_6$
(b)	$\kappa_2 + 2j_1 - j_2 - 4j_3 + 2j_4 - 4j_6$
(c)	$\kappa_2 + j_2 - 2j_4 - 4j_6$
(d)	$\kappa_2 - 2j_1 + j_2 - 4j_3 + 2j_4 + 4j_6$
(e)	$\kappa_2 + j_2 - 2j_4 + 4j_6$
(f)	$\kappa_2 - 2j_1 - j_2 + 4j_3 + 2j_4 - 4j_6$
(g)	$\kappa_2/2 + j_1 - 2j_5 - 4j_7$

TABLE II. Expansion parameters of the Hamiltonian for BaTiO$_3$. Energies are in hartrees.

On-site	κ_2	0.0568	α	0.320	γ	-0.473
Intersite	j_1	-0.02734	j_2	0.04020		
	j_3	0.00927	j_4	-0.00815	j_5	0.00580
	j_6	0.00370	j_7	0.00185		
Elastic	B_{11}	4.64	B_{12}	1.65	B_{44}	1.85
Coupling	B_{1xx}	-2.18	B_{1yy}	-0.20	B_{4yz}	-0.08
Dipole	Z^*	9.956	ϵ_∞	5.24		

first-, second-, and third-neighbor interactions turns out to be approximately 1 : 0.23 : 0.09. This decays even faster than the dipole-dipole interactions, for which the corresponding ratio ($\propto 1/R^3$) is 1 : 0.35 : 0.19. These results help justify our approximation of including only up to third nearest neighbors for the short-range interactions.

IV. MONTE CARLO SIMULATIONS

For the quantitative study of the nonuniversal finite-temperature behavior of a given model, Monte Carlo simulation[19,24] has emerged as the most reliable and powerful technique. It is especially appropriate for a model such as ours, with two continuous vector degrees of freedom per unit cell and both short- and long-range interactions, for which analytical approaches such as renormalization group or high-temperature expansions would be cumbersome and involve additional approximations. In comparison, the Monte Carlo approach requires only the ability to compute changes in total-energy as the configuration is changed. Furthermore, with suitable analysis of statistical errors and finite-size effects, the results of Monte Carlo simulation can be made arbitrarily accurate. Finally, with little additional effort, a number of physical quantities can be computed to aid in characterization of the transition.

We solve the effective Hamiltonian [Eqs. (2), (7), (9), (11), and (14)] using Monte Carlo simulations with the Metropolis algorithm[25] on an $L \times L \times L$ cubic lattice with periodic boundary conditions. Since most energy contributions (except E^{dpl}) are local, we choose the single-flip algorithm. That is, a trial move consists of an attempted update of a single variable, after which the total energy change is calculated to determine whether to accept the move. The step sizes are adjusted to ensure an acceptance ratio of approximately 0.2. In one Monte Carlo sweep (MCS), we first make a trial move on each $\mathbf{u}_i$ in sequence, then each $\mathbf{v}_i$ in sequence, then iterate several times (typically $2L$ times) on the homogeneous strain variables. For $L = 12$, each MCS takes about one second on an HP 735 workstation. The typical correlation time for the total energy is found to be several hundred MCS's close to the phase transition; this long correlation time makes certain new MC techniques using energy distribution functions[26] unfavorable. The correlation times for the local-mode amplitudes are one order of magnitude shorter, and thus 10 000 MCS's are usually enough to equilibrate and to obtain averages of local-mode variables with a statistical error of < 10%.

In our simulation, we concentrate on identifying the succession of low-temperature phases, determining the phase transition temperatures and extracting qualitative features of the transitions. This analysis will allow us to identify the features of the effective Hamiltonian which most strongly affect the transition properties. For these purposes, it is most convenient to monitor directly the behavior of the homogeneous strain and the vector order parameter. In the case of the ferroelectric phase transition, the latter is just the average local-mode vector

$\mathbf{u} = \sum_i \mathbf{u}_i/N$, which is proportional to the polarization. Here, $\mathbf{u}_i$ is the local-mode vector at site i and N is the total number of sites. As a reference, the average local mode amplitude $u = \sum_i |\mathbf{u}_i|/N$ is also monitored. To avoid effects of symmetry-equivalent rotations of the order parameter and to identify the different phases clearly, we accumulate the absolute values of the largest, middle, and smallest components of the averaged local-mode vector for each step, denoted by u_1, u_2, and u_3, respectively ($u_1 > u_2 > u_3$). The cubic (C), tetragonal (T), orthorhombic (O), and rhombohedral (R) phases are then characterized by zero, one, two, and three nonzero order-parameter components, respectively. The effect of symmetry-equivalent rotations on the homogeneous strain is handled analogously, with the largest, the medium, and the smallest linear strain components denoted by η_1, η_2, and η_3, respectively, and shear strain components by η_4, η_5, and η_6.

The ferroelectric phase transition is very sensitive to hydrostatic pressure or, equivalently, to the lattice constant. The LDA-calculated lattice constants are typically 1% too small, and even this small error can lead to large errors in the zero-pressure transition temperatures. One approach, which largely compensates for the effect of this systematic error, is to exert a negative pressure that expands the lattice constant to the experimental value. We determine the value of the pressure by calculating volumes for four different phases and comparing with experimental measurements.[27] We find $P = -4.8$ GPa gives the best overall agreement (although the application of pressure does lead to a slight change in the low-temperature structure). Except for the simulations for the construction of the temperature-pressure phase diagram, the following simulations and analysis are for this pressure.

V. RESULTS AND DISCUSSION

In this section, the finite-temperature behavior of the model is presented and analyzed. First, we examine the order parameters as a function of temperature in a typical simulation to obtain a measure of the transition temperatures. From the results of simulations for a range of pressures, we construct the temperature-pressure phase diagram. For the system at ambient pressure, more detailed simulations are performed. The order of the transitions, the nature of the paraelectric phase, and the properties of the low-temperature phases are investigated and compared with experimental observations. Finally, the roles played by different terms in the effective Hamiltonian and the sensitivity of the results to various approximations are examined.

A. Order parameters and phase diagram

We start the simulations at a high temperature ($T > 400$ K) and equilibrate for 10 000 MCS's. The temperature is then reduced in small steps, typically 10 K. After each step, the system is allowed to equilibrate for 10 000

MCS's. The order parameter averages are then accumulated over a period of 7 000 MCS's, yielding a typical standard deviation of less than 10%. The temperature step size is reduced and the number of MCS's is doubled for temperatures close to the phase transition.

We describe a typical simulation for an $L = 12$ lattice at $P = -4.8$ GPa. At high temperatures, the averaged local mode amplitudes u_1, u_2, and u_3 are all very close to zero. As the system is cooled down below 295 K, u_1 increases and becomes significantly larger than u_2 or u_3. This indicates the transition to the tetragonal phase. Two additional phase transitions occur as the temperature is reduced further. The T-O transition (sudden increase of u_2) occurs at 230 K and the O-R transition (sudden increase of u_3) occurs at 190 K. This behavior is plotted in Fig. 2 of Ref. 16. The sequence of transitions exhibited by the simulation is the same as that observed experimentally.

The averaged homogeneous strain variables obtained from the above simulation are shown in Fig. 3. These strains are measured relative to the LDA-calculated equilibrium cubic structure, and so the linear strains are significantly nonzero at higher temperatures due to the negative pressure applied. As expected, the simulation cell changes shape at the same temperatures at which the jumps of the order-parameter components are observed. At high temperatures, we have approximately $\eta_1 = \eta_2 = \eta_3$ and $\eta_4 = \eta_5 = \eta_6 = 0$, corresponding to the cubic structure. As the system is cooled down, the shape of the simulation cell changes to T, O, and R phases. The orthorhombic (O) structure has a nonzero shear strain, in agreement with the centered orthorhombic structure observed experimentally. Quantitatively, our calculated distortions are also in good agreement with the experiment, with the calculated distortions tending to be slightly smaller. For example, η_1-η_3 for the tetragonal phase is 1.1% as measured from experiment[27] and 0.9% from our calculation.

The simulations are repeated for a range of applied pressures to obtain the temperatures at which the order-parameter components and homogeneous strain jump on cooling down. The resulting temperature-pressure phase diagram is shown in Fig. 4. (This measure of the transi-
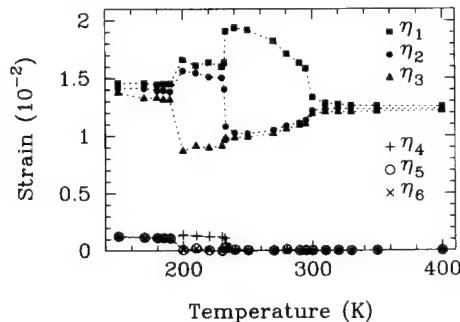

FIG. 4. The calculated pressure-temperature phase diagram. The cubic-tetragonal (C-T), tetragonal-orthorhombic (T-O), and orthorhombic-rhombohedral (O-R) transitions are labeled by solid triangles, circles, and squares, respectively. The vertical dash-dotted line at $P=-4.8$ GPa, corresponds to zero pressure in the experiment to compensate for the LDA volume error.

tion temperature is actually a lower bound, due to hysteresis around 5% for T-O and O-R transitions and negligible for the C-T transition, to be discussed further below.) All three transition temperatures decrease almost linearly with increasing pressure. At the experimental lattice constant, the values for dT_c/dP are found to be -28, -22, and -15 K/GPa for the C-T, T-O, and O-R transitions, respectively. The experimental values for the C-T transition range from -40 K/GPa (Ref. 28) to -66 K/GPa.[29] For the T-O transition the measured value is -28 K/GPa,[29] and for the O-R transition it is -10 to -15 K/GPa.[29] At pressures as high as $P = 5$ GPa, the sequence of phases C-T-O-R is still observed in the simulation. When the pressure is increased further, the phase boundary in the simulation becomes unclear due to fluctuations. Our calculated critical pressure (beyond which the cubic structure is stable at $T=0$ K) is $P_c = 8.4$ GPa. Taking into account the pressure correction for the LDA volume underestimate, this corresponds to a predicted physical $P_c = 13.2$ GPa. We are not aware of any experimental value for P_c with which to compare this value. However, we find that the magnitude of our dT_c/dP is significantly smaller than experimental value, at least for the C-T and T-O transitions. This may partly be due to the neglect of higher-order strain coupling terms in the effective Hamiltonian. We have tested the effect of including a volume dependence for the short-range interaction parameters j_i. This correction does not change the sequence of phases, and it only increases the magnitudes of dT_c/dP slightly. Therefore, our results are reported without this correction. The accuracy of the phase diagram may be further improved by including higher-order terms in the elastic energy or the coupling of j_i to anisotropic strain.

Transition temperatures at $P = -4.8$ GPa for the three system sizes $L = 10$, 12, and 14 are reported and compared with experiment in Table III. (The details of the determination of these values and their error estimates appears in the next subsection.) The calculated transition temperatures are well converged with respect to system size and are in reasonable agreement with ex-

FIG. 3. The averaged homogeneous strain η_H as a function of temperature in the cooling-down simulation of a $12 \times 12 \times 12$ lattice described in Sec. IV. The strains are measured relative to the LDA minimum-energy cubic structure with lattice constant 7.46 a.u. The dotted lines are guides to the eye.
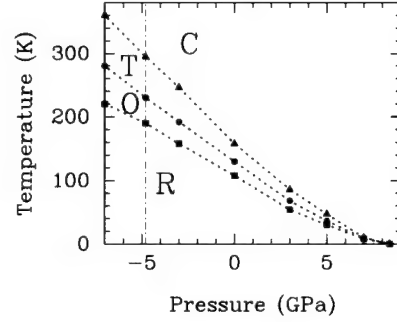
TABLE III. Calculated transition temperatures T_c, saturated spontaneous polarizations p_s, and estimated latent heats l, as a function of simulation cell size.

	Phase	$L = 10$	$L = 12$	$L = 14$	Expt.[a]
	O-R	197 ± 3	200 ± 10	200 ± 5	183
T_c (K)	T-O	230 ± 10	232 ± 2	230 ± 10	278
	C-T	~290	296 ± 1	297 ± 1	403
	R	0.43	0.43	0.43	0.33
p_s (C/m^2)	O	0.35	0.35	0.35	0.36
	T	0.28	0.28	0.28	0.27
	O-R	50	60	60	33–60
l (J/mol)	T-O	90	90	100	65–92
	C-T			150	196–209

[a]Ref. 27.

periment. While discrepancies of up to 30% between theory and experiment may seem large, we believe this level of agreement is quite good for an entirely *ab initio* approach, especially given the extreme sensitivity of the transition temperatures to the lattice constant. Indeed, it can be seen from Fig. 4 that a change of the fictitious applied pressure from -5 to -7 GPa, corresponding to a change of lattice constant of only about 0.4%, would roughly be sufficient to bring the transition temperatures into line with experiment. Thus, we believe that the discrepancies with experiment are closely related to the intrinsic LDA lattice-constant error, which is incompletely compensated for by the artifice of working at a predetermined negative fictitious pressure.

B. Hysteresis and latent heat

For the investigation of the order of the transitions, the nature of the paraelectric phase, and the properties of the low-temperature phases, we performed more detailed simulations at $P = -4.8$ GPa for the three system sizes $L = 10$, 12, and 14. In the cooling-down simulations, the length of each simulation was increased from 10 000 to up to 35 000 MCS's at temperatures close (±10 K) to the phase transition to include a longer equilibration. The size of the temperature step was decreased to 5 K or less in the vicinity of the transition. In addition, a heating simulation was performed, starting from the lower-temperature phase, to detect any possible hysteresis. The calculated transition temperatures, obtained as the average of the cooling and heating transition temperatures, are given in Table III. The error estimates in the table are determined by the width of the hysteresis, which persists even for the longest simulation lengths considered. (The C-T transition temperature for $L = 10$ is difficult to identify because of large fluctuations between phases.)

Table III also gives the saturated spontaneous polarization p_s at $T = 0$ in the R phase, and just above the O-R and T-O transitions in the O and T phases, respectively. These are calculated from the average local-mode vector $\mathbf{u}$ and the local mode Z^*. We find almost no finite-size dependence for this quantity, as long as it is determined at a temperature which does not lie in one of

the hysteresis regions near the transition temperatures. The agreement with experiment is very good for the O and T phases. The disagreement for the R phase may result in part from twinning effects in the experimental sample.[30]

From the jumps in structural parameters and the observed hysteresis in heating and cooling, we conclude that the phase transitions are first order. An accurate determination of the latent heats would require considerable effort;[31] here, we only try to provide estimates sufficiently accurate for meaningful comparison with experiment. We approach each transition from both high-temperature and low-temperature sides until the point is reached where both phases appear equally stable. (That is, the typical time for the system to fluctuate into the opposite phase is roughly independent of which phase the simulation is started in.) The difference of the average total energy is then the latent heat.[32] This approach is practical as long as some hysteresis is present. The calculated latent heats (Table III) show non-negligible finite-size dependence. Taking this into account, we find that the latent heats for all three transitions are significantly nonzero and in rough agreement with the rather scattered experimental data. For the T-O and O-R transitions, the first-order character of the transition is predicted by Landau theory, since in these two cases the symmetry group of the low-temperature structure is not a subgroup of that of the high-temperature structure. For the C-T transition, the first-order character is not a consequence of symmetry, but rather of the values of the effective Hamiltonian parameters. Although it has the largest latent heat of the three transitions, the C-T transition also exhibits large finite-size effects in the latent heat and in the smearing of order-parameter components and strain discontinuities in the simulation (Fig. 2 of Ref. 16 and Fig. 3). This suggests the presence of long-wavelength fluctuations characteristic of second-order phase transitions and critical phenomena, and the classification of the C-T transition as a weak first-order transition.

C. Displacive vs order-disorder

Using the microscopic information available in the simulations, we are able to investigate the extent to which the cubic-tetragonal transition can be characterized as an order-disorder or displacive transition. These possibilities can be distinguished by inspecting the distribution of the real-space local-mode vector $\mathbf{u}_i$ in the cubic phase just above the transition. A displacive (microscopically nonpolar) or order-disorder (microscopically polar) transition should be characterized by a single-peaked or double-peaked structure, respectively. The distribution of u_x at $T = 400$ K is shown in Fig. 5. It exhibits a rather weak tendency to a double-peaked structure, indicating a transition which has some degree of order-disorder character. We also see indications of this in the u-T relation in Fig. 2 of Ref. 16. Even in the cubic phase, the average of the local-mode magnitude u is significantly nonzero and close to that of the rhombohedral phase, while the magnitudes of the average local-mode compo-
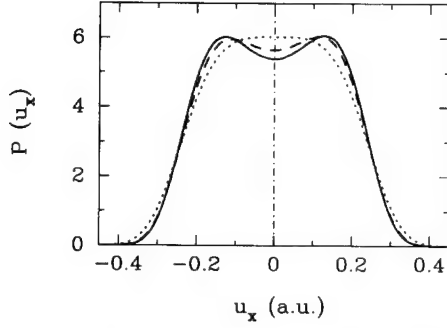
FIG. 5. The probability distribution of the Cartesian component of the local-mode variable u_x in the cubic phase at $T = 320$ K (solid line), 350 K (dashed line), and 500 K (dotted line).

nents change dramatically during the phase transitions.

In reciprocal space, a system close to a displacive transition should show large and strongly temperature-dependent fluctuations of certain modes associated with a small portion of the Brillouin zone (BZ) (for a ferroelectric transition, near Γ). For an extreme order-disorder transition, on the other hand, the fluctuations are expected to be distributed over the whole BZ. For BaTiO$_3$, we calculated the average Fourier modulus $F(\mathbf{k}, T) = \langle |u(\mathbf{k})|^2 \rangle$ for eigenmodes at several high-symmetry k points (along Γ-X, Γ-M, and Γ-R) for a range of temperatures above the C-T transition. These eigenmodes are identified by their symmetry properties as one longitudinal optical (LO) branch and two transverse optical (TO) branches at each point. For a purely harmonic system, $T/F(\mathbf{k}, T)$ can be shown to be a temperature-independent constant proportional to the square of the eigenfrequency $\omega^2(\mathbf{k})$ of the corresponding eigenmode. A strong decrease of $T/F(\mathbf{k}, T)$ as $T \to T_c$ from high temperature can be interpreted as mode softening due to anharmonicity.

The results at the k point $(\pi/4a, \pi/4a, 0)$ illustrate the main features of this analysis. From symmetry, three nondegenerate eigenmodes LO, TO1, TO2 are identified. The polarization of LO, TO1, and TO2 are in the direction of $\hat{\mathbf{x}} + \hat{\mathbf{y}}$, $\hat{\mathbf{x}} - \hat{\mathbf{y}}$, and $\hat{\mathbf{z}}$, respectively. For each

eigenmode, the temperature dependence of the calculated $\omega^2(\mathbf{k}, T)$ is shown in Fig. 6. The almost linear behavior of $\omega^2(\mathbf{k}, T)$ vs T (the Curie-Weiss form) is observed for the other k points as well. Both the LO and TO1 branches are almost temperature independent. The TO2 branch is strongly temperature dependent and is thus a "soft" mode. According to the soft-mode theory of structural phase transitions, T_c is the lowest temperature at which all $\omega^2(\mathbf{k}, T) \geq 0$. Linear extrapolation indicates that the TO2 mode frequency goes to zero at $T \approx 200$ K, which is a lower bound for T_c, consistent with the value obtained in Monte Carlo simulations. A similar calculation of $\omega^2(\mathbf{k}, T)$ for the TO modes at $\Gamma = (0,0,0)$ extrapolates to zero at the higher temperature $T \approx 300$ K, in excellent agreement with the Monte Carlo value of 295 K.

Within this formalism, the microscopic character of the paraelectric phase is determined by the extent of the soft mode in the BZ. We define a quantity

$$\rho(\mathbf{k}) = \frac{2F(\mathbf{k}, 350 \text{ K})}{F(\mathbf{k}, 700 \text{ K})} \qquad (15)$$

to indicate the hardness of the modes. In Fig. 7, $\rho(\mathbf{k})$ is shown for the various k points along some special directions in the BZ. If $\rho(\mathbf{k}) < 1$, the corresponding eigenfrequency extrapolates to zero at some positive temperature, and the mode is regarded as soft. If $\omega^2(\mathbf{k})$ is independent of temperature, $\rho(\mathbf{k}) = 2$, corresponding to the hardest mode.

For all the k points considered, all the LO modes are almost temperature independent $[\rho(\mathbf{k}) = 2]$ and are not included in the figure. Along the Γ-X direction, the doubly degenerate TO modes are soft all the way to the zone boundary. In contrast, along the Γ-R direction, both TO modes become hard immediately after leaving the Γ point. Along the Γ-M direction, the TO1 mode becomes hard quickly, while the TO2 branch remains soft at least halfway to the zone boundary. This behavior, especially along Γ-X, does not conform completely to the displacive limit. This supports the interpretation of the C-T transition as intermediate between a displacive and order-disorder transition, with a slightly stronger order-disorder character. Thus, from the example of BaTiO$_3$, it seems that a positive on-site quadratic coefficient does not automatically imply a displacive character for the transition. Rather, the relevant criterion is the extent to which the unstable modes extend throughout the BZ.
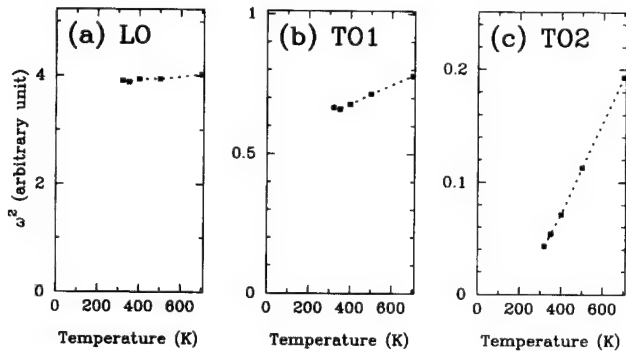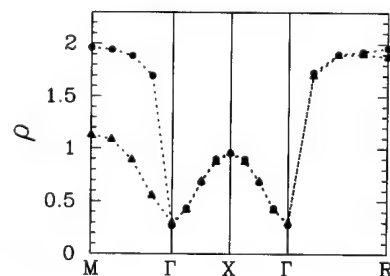

FIG. 6. Temperature dependence of squared eigenfrequency ω^2 at $\mathbf{k} = (\pi/4a, \pi/4a, 0)$ for (a) LO, (b) TO1, and (c) TO2 modes.

FIG. 7. Calculated mode hardness quantity $\rho(\mathbf{k})$, Eq. (15), along special directions in the Brillouin zone.

D. Roles of different interactions

Our theoretical approach allows us to investigate the roles played by different types of interaction in the phase transition. First, we study the effect of strain. Recall that the strain degrees of freedom were separated into local and homogeneous parts, representing finite- and infinite-wavelength acoustic modes, respectively. Both parts were included in the simulations. If we eliminate the local strain (while still allowing homogeneous strain), we find almost no change in the transition temperatures. This indicates that the effect of the short-wavelength acoustic modes may not be important for the ferroelectric phase transition. If the homogeneous strain is frozen at zero, however, we find a direct cubic-rhombohedral phase transition, instead of the correct series of three transitions. This demonstrates the important role of homogeneous strain.

Second, we studied the significance of the long-range Coulomb interaction in the simulation. To do this, we changed the effective charge of the local mode (and thus the dipole-dipole interaction strength), while modifying the second-order self-energy parameter κ_2, so that the frequencies of the zone-center and zone-boundary modes remain in agreement with the LDA values. We found only a slight change (10%) of the transition temperatures when the dipole-dipole interaction strength was doubled. However, elimination of the dipole-dipole interaction altogether changed the results dramatically; the ground state becomes a complex antiferroelectric structure similar to the room-temperature structure of $PbZrO_3$. This result shows that it is essential to include the long-range interaction, although small inaccuracies in the calculated values of the effective charges or dielectric constants may not be very critical.

Third, we investigated the sensitivity of our results to variations of the short-range interaction parameters. We find the accuracy of the first-neighbor interaction parameters (j_1, j_2) is very important, and a mere 10% deviation can change the calculated transition temperatures dramatically, and can sometimes even change the ground state structure. Second nearest-neighbor interactions are less important, and for the third-neighbor interactions, even a 100% change does not seem to have a strong effect on the values of T_c. This result is to be expected, and partly justifies our choice of including only up to third neighbors for the short-range interactions. We have also tested the effect of our assumption $j_6 - 2j_7 = 0$. We find that any reasonable choice leads to a barely noticeable change in T_c.

In short, highly accurate LDA calculations do appear to be a prerequisite for an accurate determination of the transition temperatures, but as long as certain features of the energy surface are correctly described, other approximations can be made without significantly affecting the results.

VI. CONCLUSIONS

We have developed a first-principles approach to the study of structural phase transitions and finite-temperature properties in perovskite compounds. We construct an effective Hamiltonian based on Taylor expansion of the energy surface around the cubic structure, including soft optical modes and strain components as the possible distortions. The expansion parameters are determined by first-principles density-functional calculations using Vanderbilt's ultrasoft pseudopotential.

We have applied this scheme to $BaTiO_3$ and calculated the pressure-temperature phase diagram. We have obtained the sequence of low-temperature phases, the transition temperatures, and the spontaneous polarizations, and found them to be in good agreement with experiment. We find that long-wavelength acoustic modes and long-range dipolar interactions both play an important role in the phase transition, while short-wavelength acoustic modes are not as significant. Accurate LDA calculations are required for accurate determination of the transition temperatures. The C-T phase transition is not found to be well described as a simple displacive transition; on the contrary, if anything it has more order-disorder character.

With slight modifications, our approach should be applicable to other perovskite compounds, as long as their structure is close to cubic and there are some low-energy distortions responsible for the phase transitions. It can be easily applied to ferroelectric materials like $PbTiO_3$ (under study by another group[14]) and $KNbO_3$. It can also be applied to antiferroelectric materials like $PbZrO_3$. The application to antiferrodistortive materials like $SrTiO_3$ is slightly more involved, though also successful.[33]

[1] M. E. Lines and A. M. Glass, *Principles and Applications of Ferroelectrics and Related Materials* (Clarendon, Oxford, 1977).

[2] M. T. Dove, A. P. Giddy, and V. Heine, Ferroelectrics **136**, 33 (1992).

[3] E. Pytte, Phys. Rev. B **5**, 3758 (1972).

[4] A. D. Bruce and R. A. Cowley, *Structural Phase Transitions* (Taylor & Francis, London, 1981).

[5] H. Bilz, G. Benedek, and A. Bussmann-Holder, Phys. Rev. B **87**, 4840 (1987) and references therein.

[6] G. Gordon and Y. S. Kim, J. Chem. Phys. **56**, 3122 (1972); L. L. Boyer *et al.*, Phys. Rev. Lett. **54**, 1940 (1985); P. J. Edwardson *et al.*, Phys. Rev. B **39**, 9738 (1989).

[7] R. E. Cohen and H. Krakauer, Phys. Rev. B **42**, 6416 (1990); Ferroelectrics **136**, 65 (1992); R. E. Cohen, Nature **358**, 136 (1992).

[8] D. J. Singh and L. L. Boyer, Ferroelectrics **136**, 95 (1992).

[9] R. D. King-Smith and D. Vanderbilt, Ferroelectrics **136**, 85 (1992).

[10] R. D. King-Smith and D. Vanderbilt, Phys. Rev. B **49**, 5828 (1994).

[11] R. D. King-Smith and D. Vanderbilt, Phys. Rev. B **47**, 1651 (1993); D. Vanderbilt and R. D. King-Smith, *ibid.* **48**, 4442 (1993).

[12] W. Zhong, R. D. King-Smith, and D. Vanderbilt, Phys. Rev. Lett. **72**, 3618 (1994).

[13] K. M. Rabe and J. D. Joannopoulos, Phys. Rev. Lett. **59**, 570 (1987); Phys. Rev. B **36**, 6631 (1987).

[14] K. M. Rabe and U. V. Waghmare, Ferroelectrics **164**, 15 (1995); (unpublished).

[15] D. Vanderbilt, Phys. Rev. B **41**, 7892 (1990).

[16] W. Zhong, D. Vanderbilt, and K. M. Rabe, Phys. Rev. Lett. **73**, 1861 (1994).

[17] K. M. Rabe and U. V. Waghmare (unpublished).

[18] D. Vanderbilt, S. H. Taole, and S. Narasimhan, Phys. Rev. B **40**, 5657 (1989); **42**, 11 373(E) (1990).

[19] M. P. Allen and D. J. Tildesley, *Computer Simulation of Liquids* (Oxford, New York, 1990).

[20] P. N. Keating, Phys. Rev. **145**, 637 (1966).

[21] M. C. Payne, M. P. Teter, D. C. Allan, T. A. Arias, and J. D. Joannopoulos, Rev. Mod. Phys. **64**, 1045 (1992).

[22] T. A. Arias, M. C. Payne, and J. D. Joannopoulos, Phys. Rev. Lett. **69**, 1077 (1992).

[23] H. J. Monkhorst and J. D. Pack, Phys. Rev. B **13**, 5188 (1976).

[24] K. Binder and D. W. Heermann, *Monte Carlo Simulation in Statistical Physics* (Springer-Verlag, Berlin, 1988); *The Monte Carlo Method in Condensed Matter Physics*, edited by K. Binder (Springer-Verlag, Berlin, 1992); *Application of the Monte Carlo Method in Statistical Physics*, edited by K. Binder (Springer-Verlag, Berlin, 1984).

[25] N. Metropolis *et al.*, J. Chem. Phys. **21**, 1087 (1953).

[26] A. M. Ferrenberg and R. H. Swendsen, Phys. Rev. Lett. **61**, 2635 (1988); **63**, 1195 (1989); J. Lee and J. M. Kosterlitz, *ibid.* **65**, 137 (1990); Phys. Rev. B **43**, 3265 (1991).

[27] *Landolt-Bornstein Numerical Data and Functional Relationships in Science and Technology*, edited by T. Mitsui *et al.* (Springer-Verlag, Berlin, 1981), NS, Group III, Vol. 16; *ibid.*, edited by E. Nakamura *et al.*, NS, Group III, Vol. 28.

[28] R. Clarke and L. Benguigui, J. Phys. C **10**, 1963 (1977).

[29] G. Samara, Phys. Rev. **151**, 378 (1966).

[30] H. H. Wieder, Phys. Rev. **99**, 1161 (1955).

[31] W. Janke, Phys. Rev. B **47**, 14 757 (1993).

[32] Under a *physical* applied pressure, the latent heat would be the change of enthalpy, not energy. If this were applied to our case of a *fictitious* pressure, the calculated latent heats would be approximately twice as large.

[33] W. Zhong and D. Vanderbilt, Phys. Rev. Lett. **74**, 2587 (1995).

Competing Structural Instabilities in Cubic Perovskites

W. Zhong and David Vanderbilt

Department of Physics and Astronomy, Rutgers University, Piscataway, New Jersey 08855-0849
(Received 17 November 1994)

We study the antiferrodistortive instability and its interaction with ferroelectricity in cubic perovskite compounds. Our first-principles calculations show that coexistence of both instabilities is very common. We develop a first-principles scheme to study the thermodynamics of these compounds when both instabilities are present, and apply it to $SrTiO_3$. We find that increased pressure enhances the antiferrodistortive instability while suppressing the ferroelectric one. Moreover, the presence of one instability tends to suppress the other. A very rich P-T phase diagram results.

The great fascination of the cubic perovskite structure is that it can readily display a variety of structural phase transitions, ranging from nonpolar antiferrodistortive (AFD) to ferroelectric (FE) and antiferroelectric in nature [1]. The competition between these different instabilities evidently plays itself out in a variety of ways, depending on the chemical species involved, leading to the unusual variety and richness of the observed structural phase diagrams. Moreover, all the phase transitions involve only small distortions from the ideal cubic structure, and are therefore appealing objects for experimental and theoretical study. However, our microscopic understanding of the chemical origins of these instabilities and of their interactions is still very limited.

Thus, there is a pressing need for accurate, chemically specific investigations of the structural energetics of these compounds, leading to a detailed understanding of the phase transition behavior. Previous phenomenological model Hamiltonian approaches [2–5] have been limited by oversimplification and ambiguities in interpretation of experiment, while empirical [6] and nonempirical pair-potential methods [7] have not offered high enough accuracy. First-principles density-functional calculations have been shown to provide accurate total-energy surfaces for perovskites as regards FE distortions [8–10]. However, to our knowledge, there have been no previous first-principles studies of AFD distortions, and therefore no detailed microscopic theories of the phase transformation behavior.

Here, we build upon previous work in which a fully first-principles scheme was used to study the FE transitions in $BaTiO_3$, leading to an accurate microscopic understanding of the phase transition sequence [11]. In the present work, we develop a similar approach which is capable of treating simultaneously the FE and AFD degrees of freedom, allowing for the first time a detailed *ab initio* study of the phase behavior for perovskites in which both instabilities are present. We present systematic calculations of the susceptibility against R-point zone-boundary AFD modes for a set of eight compounds, demonstrating that the AFD instability is very common. Then, we briefly describe our first-principles scheme for studying finite-temperature properties, and apply it to $SrTiO_3$. We

study the evolution of the phonon instabilities with temperature, and calculate the P-T phase diagram. In so doing, we compute the interactions between the AFD and FE instabilities, and expose their implications for the thermodynamic properties.

The high-symmetry ABO_3 perovskite structure is simple cubic with O atoms at the face centers and metal atoms A and B at the cube corner and body center, respectively. The two most common instabilities result from a softening of either a zone-center polar phonon mode (FE) or a nonpolar zone-boundary mode (AFD) involving rigid rotations of oxygen octahedra. These modes are illustrated in the left and right insets, respectively, in Fig. 1. $BaTiO_3$ is a classical example of the first type, while the best-known example of the second kind is the $T = 105$ K transition in $SrTiO_3$ [5], which results from a softening of a Γ_{25} phonon at R [$(111)\pi/a$].

The stability of perovskite compounds against R-point phonon distortions can be expressed in terms of a stiffness $\kappa^R = \frac{1}{2} \partial^2 E/\partial \phi^2$, where ϕ is the rotation angle of the oxygen octahedra. To obtain κ^R, we perform frozen
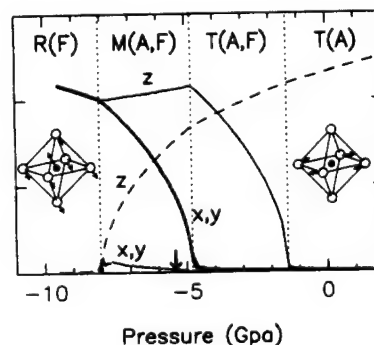

FIG. 1. $T = 0$ order parameters vs pressure for $SrTiO_3$. Solid and dashed lines denote Cartesian components of $\mathbf{f}(\Gamma)$ and $\mathbf{a}(R)$, respectively. Phases are labeled by lattice symmetry (R = rhombohedral, M = monoclinic, T = tetragonal, O = orthorhombic) and by instabilities present (A =antiferrodistortive, F = ferroelectric). Dotted lines denote phase boundaries. Vertical arrow indicates theoretical pressure P_0 at which the lattice constant matches the experimental $P = 0$ one. Left inset: sketch of displacements leading to $R(F)$ phase (Sr is omitted for clarity). Right inset: same for $T(A)$ phase.

TABLE I. Calculated stiffness κ^R of R-point AFD phonon mode (in Hartree), and tolerance factor t, for several perovskite compounds.

	κ^R	t		κ^R	t
$BaTiO_3$	0.295	1.07	$SrTiO_3$	−0.042	1.01
$KNbO_3$	0.242	1.06	$NaNbO_3$	−0.133	0.97
$BaZrO_3$	−0.021	1.01	$PbZrO_3$	−0.324	0.97
$PbTiO_3$	−0.037	1.03	$CaTiO_3$	−0.375	0.97

phonon calculations using density-functional theory within the local-density approximation (LDA) and Vanderbilt ultrasoft pseudopotentials [12]. In Table I, we list values of κ^R for a set of eight compounds, calculated at the experimental lattice constants [13] as listed in Ref. [10]. Negative values indicate instability to R-point phonon distortions.

Table I shows that the tendency towards AFD instability is strongly correlated with trends in ionic radii. Such trends in an ABO_3 compound are conventionally described by a tolerance factor $t = (r_A + r_O)/\sqrt{2}(r_B + r_O)$. Values for t are given in Table I, using the ionic radii of Ref. [14]. We find that κ_R is almost monotonic with t; i.e., a larger A or a smaller B atom tends to stabilize the cubic structure. This simple behavior contrasts with the case of the ferroelectric instability, where covalent interactions play an important role [15].

Inspecting Table I, we see that the two compounds $BaTiO_3$ and $KNbO_3$ are clearly stable with respect to AFD distortions, consistent with experimental observations. (Both materials undergo a similar series of FE transitions.) On the other extreme, we find that $CaTiO_3$, $PbZrO_3$, and $NaNbO_3$ have a strong AFD instability. All three compounds are also predicted to have FE instabilities [10], consistent with the observation of complex phase diagrams and high transition temperatures in all three cases. Finally, our calculations for $SrTiO_3$, $PbTiO_3$, and $BaZrO_3$ show a weak AFD instability. $PbTiO_3$ is observed to go through a weak unidentified transition at $T = 180$ K [16] which could be AFD related. $BaZrO_3$ is observed to remain cubic down to $T = 0$; the weak instability predicted by our calculation could be suppressed by quantum zero-point fluctuations. For $SrTiO_3$, we predict a weak AFD instability consistent with a low T_c of 105 K observed for its cubic-to-AFD transition.

The above calculations indicate that coexistence of FE and AFD instabilities is very common in perovskites. To study the consequence of such a situation, we have chosen to study the case of $SrTiO_3$ in depth. Our first-principles scheme can be explained briefly as follows. The energy is Taylor expanded in low-energy distortions, with expansion parameters determined from LDA calculations. The resulting Hamiltonian is studied using Monte Carlo (MC) simulations. The low-energy distortions we included are those connected with zone-center FE-like modes, zone-boundary AFD-like modes, and strain. To do this we con-

struct a FE "local mode" such that a uniform arrangement of local mode amplitudes f_l reproduces the softest zone-center Γ_{15} (FE) modes (l is a cell index). Similarly, we construct an AFD local mode (a local rotation of an oxygen octahedron) so that a staggered arrangement of amplitudes a_l reproduces the $\Gamma_{25}(R)$ mode. Finally, the local strains are represented in terms of a displacement vector u_l.

Thus, we have three vector degrees of freedom f_l, a_l, and u_l per cell. The energy terms retained in our Taylor expansion of the potential energy are as follows: (i) on-site self-energy, up to quartic anharmonic order for f_l and a_l, and up to harmonic order for u_l (elastic energy); (ii) harmonic intersite interactions between f_l (including long-range dipole-dipole interactions) and a_l (short-range only); and (iii) on-site coupling energy to the lowest order between a_l and u_l, between f_l and u_l, and between f_l and a_l. The determination of the expansion parameters involves LDA calculations for supercells containing up to 20 atoms with low symmetry, using ultrasoft pseudopotentials [12]. The details of the Hamiltonian, the first-principles calculations, and the values of the expansion parameters will be presented elsewhere [17].

To obtain the structural and thermodynamic properties, we perform MC simulations on an $L \times L \times L$ cubic lattice with periodic boundary conditions [18]. The identification of different phases can be made by monitoring the FE order parameter $f(\Gamma)$ (the Fourier transform of f_l at $k = \Gamma$), and similarly the AFD order parameters $a(R)$ and $a(M)$ [$M = (110)\pi/a$]. $a(M)$ is found to remain small for $SrTiO_3$, and will not be discussed further.

We first investigate the ground-state structure for $SrTiO_3$ as a function of hydrostatic pressure. We find it convenient to run the MC calculations at $L = 4$ at $T = 0.1$ K (finite-size and hysteresis effects are not important at low T). The calculated order parameters $a(R)$ and $f(\Gamma)$ are shown in Fig. 1. Zero pressure in the figure corresponds to the LDA-calculated equilibrium lattice constant, which is about 1% too small. Since both the FE and AFD instabilities are sensitive to lattice constant, comparison with the experimental phase diagram is best made with the zero of the pressure axis shifted by $P_0 = -5.4$ GPa (see arrow in Fig. 1), the value which restores the experimental lattice constant. From Fig. 1, we see that pressure has opposite effects on $a(R)$ and $f(\Gamma)$, and that as a function of pressure the ground state of $SrTiO_3$ can have four phases. The cubic phase, which is stable at high temperature, is not present. At high pressure, only one component of $a(R)$ is nonzero, indicating an AFD tetragonal structure ($I4/mcm$). As P is lowered, the corresponding (z) component of $f(\Gamma)$ becomes nonzero, and the structure transforms to tetragonal with FE and AFD ($I4cm$). A further decrease of pressure creates a low-symmetry monoclinic structure (Pb), in which all components of $f(\Gamma)$ and $a(R)$ are nonzero. Finally, below −8 GPa the structure becomes FE rhombohedral ($R3m$). We see that the coexistence of zone-center and zone-boundary instabilities creates many different phases and complicated structures, even at $T = 0$.

At finite temperature, the behavior becomes even more interesting. We first show our MC simulation for $P = P_0$ (-5.4 GPa) and $L = 12$. We start at high temperature and decrease T in small steps, allowing the system to reach equilibrium at each step. The hysteresis and finite-size effects on the transition temperatures are found to be negligible. In Fig. 2, we show the order parameters $\mathbf{f}(\Gamma)$ and $\mathbf{a}(R)$ as a function of T. (Since the order parameter vectors may rotate, what we actually show are the averaged maximum, intermediate, and minimum components of each vector.) Naturally, the system is found to adopt the cubic structure at high temperature. As T is reduced, a transition to an AFD tetragonal structure occurs at 130 K, as indicated by a strong increase of $a_z(R)$. A second transition occurs at $T = 70$ K to a FE tetragonal structure, below which $f_z(\Gamma) > 0$. At very low temperature (10 K), the system transforms to the low-symmetry monoclinic structure.

Comparing with experiment, we see that our cubic-to-AFD(T) transition at 130 K corresponds very well to the observed one at 105 K [19]. Our observations of additional transitions to AFD + FE phases at 70 and 10 K are not, however, in direct accord with experiment. Instead, they agree with the observed softening of the FE polar phonons, which would extrapolate to a FE transition close to 40 K [20] or 20 K [21]. It has been speculated that the absence of a true FE phase at $T = 0$ is a result of quantum fluctuations of atomic positions, leading to crossover into a "quantum paraelectric phase" at very low temperature [20–22]. Our inability to obtain agreement between the classical MC theory and experiment at $T = 0$ lends additional support to this conclusion.

To construct a P-T phase diagram, we have carried out a series of similar cooling-down simulations at different pressures. As shown in Fig. 3, there are at least seven different phases present. At strong negative pressure, $SrTiO_3$ behaves rather like $BaTiO_3$, with a cubic $\rightarrow$ tetragonal $\rightarrow$
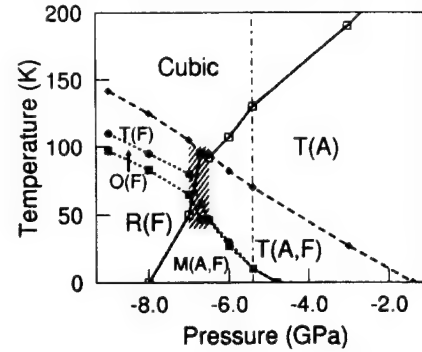
FIG. 3. P-T phase diagram of $SrTiO_3$. Hatching indicates the critical region where dramatic changes occur. Vertical dash-dotted line indicates the pressure P_0 corresponding to experimental $P = 0$. Phase labels are the same as in Fig. 1.

orthorhombic $\rightarrow$ rhombohedral sequence of transitions on cooling. Increasing the hydrostatic pressure tends to stabilize the AFD state and destabilize the FE one. The pressure coefficient $dT_c/dP = 28$ K/GPa at P_0 agrees well with the experimental value of 25 K/GPa [23]. At very high pressure, the system undergoes a single transition to a tetragonal AFD structure. In the intermediate regime, the presence of both kinds of instabilities creates a variety of phases, including the complicated monoclinic structure. The ordering of the FE and AFD transition temperatures reverses ~1.5 GPa below P_0 (hatched area in Fig. 3). In this critical region the AFD and FE transition temperature change dramatically, and the system may possess some interesting characteristics (e.g., extreme dielectric properties).

The dramatic reversal of the AFD and FE transition temperatures in the hashed region of the P-T phase diagram suggests the presence of a competition between the two instabilities. Our first-principles theory confirms this and provides microscopic insight into the competition. The FE and AFD instabilities affect each other mainly through the on-site anharmonic coupling, and through their mutual coupling to the elasticity. In $SrTiO_3$, the on-site coupling is found to lead the FE and AFD modes to suppress one another, while the coupling through strain tends to stabilize tetragonal phases relative to other phases. Our calculations show that the former effect dominates.

One way of quantifying the importance of this competition is to compare with what would happen if the FE or AFD degrees of freedom were artificially frozen out. We find that at P_0, the AFD transition temperature would be 25% higher if all $\mathbf{f}_l$ were frozen to zero; conversely, the FE C-T transition would be 20% higher if all $\mathbf{a}_l = 0$. At $T = 0$, freezing $\mathbf{f}_l = 0$ reduces the cubic-to-AFD transition pressure from -8 to -11.8 GPa, while freezing $\mathbf{a}_l = 0$ increases the cubic-to-FE transition from -1.5 to 0.8 GPa. Thus, we see clearly that the FE and AFD instabilities compete with and tend to suppress one another. Because of this competition, the $T(A,F)$ phase at P_0 is only slightly more stable than the $T(A)$ phase,
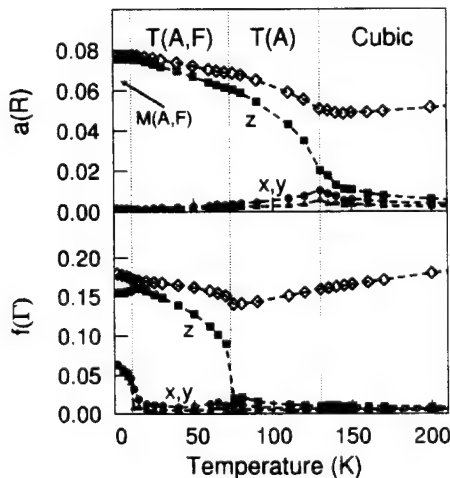

FIG. 2. Order parameters of $SrTiO_3$ vs T at $P_0 = -5.4$ GPa. Upper panel: averaged largest, middle, and smallest Cartesian components of $\mathbf{a}(R)$. Lower panel: corresponding quantities for $\mathbf{f}(\Gamma)$. Phase labels are the same as in Fig. 1.

even at $T = 0$; the energy surface relative to the FE distortion takes the form of a very long and shallow double well. This may help explain the observed suppression of the ferroelectric phase by quantum fluctuations [20–22].

Much of the interesting portion of our phase diagram appears to the left of P_0, i.e., at negative (inaccessible) physical pressures. It would be interesting, therefore, to consider compounds such as $CaTiO_3$ or $NaNbO_3$ which are FE at P_0, and study AFD instabilities at elevated P. While the exact details of our phase diagram for $SrTiO_3$ should not be expected to carry over to other perovskites, we expect the general features to persist, especially the tendency of the FE and AFD instabilities to suppress each other and the presence of complicated phase diagrams with numerous phases.

In conclusion, we have performed a fully first-principles study of the finite-temperature properties of perovskite compounds with both FE- and AFD-type instabilities. We find that AFD instabilities are almost as common as FE ones in cubic perovskite compounds. For $SrTiO_3$, our calculated P-T phase diagram shows that the FE and AFD instabilities have opposite trends with pressure. The anharmonic on-site coupling between order parameters causes the AFD and FE instabilities to tend to suppress one another.

[1] M. E. Lines and A. M. Glass, *Principles and Applications of Ferroelectrics and Related Materials* (Clarendon Press, Oxford, 1977).

[2] M. T. Dove, A. P. Giddy, and V. Heine, Ferroelectrics **136**, 33 (1992).

[3] E. Pytte, Phys. Rev. B **5**, 3758 (1972).

[4] A. D. Bruce and R. A. Cowley, *Structural Phase Transitions* (Taylor & Francis, London, 1981).

[5] E. Pytte and J. Feder, Phys. Rev. **187**, 1077 (1969); J. Feder and E. Pytte, Phys. Rev. B **1**, 4803 (1970).

[6] H. Bilz, G. Benedek, and A. Bussmann-Holder, Phys. Rev. B **37**, 4840 (1987), and references therein.

[7] G. Gordon and Y. S. Kim, J. Chem. Phys. **56**, 3122 (1972); L. L. Boyer *et al.*, Phys. Rev. Lett. **54**, 1940 (1985); P. J. Edwardson *et al.*, Phys. Rev. B **39**, 9738 (1989).

[8] R. E. Cohen and H. Krakauer, Phys. Rev. B **42**, 6416 (1990); R. E. Cohen and H. Krakauer, Ferroelectrics **136**, 65 (1992); R. E. Cohen, Nature (London) **358**, 136 (1992).

[9] D. J. Singh and L. L. Boyer, Ferroelectrics **136**, 95 (1992).

[10] R. D. King-Smith and D. Vanderbilt, Phys. Rev. B **49**, 5828 (1994); Ferroelectrics **136**, 85 (1992).

[11] W. Zhong, D. Vanderbilt, and K. M. Rabe, Phys. Rev. Lett. **73**, 1861 (1994); (unpublished).

[12] D. Vanderbilt, Phys. Rev. B **41**, 7892 (1990).

[13] Since κ^R is pressure sensitive, using experimental lattice constants avoids the error due to $\sim 1\%$ underestimate of the LDA lattice constants.

[14] R. Shannon, Acta Crystallogr. Sect. A **32**, 751 (1976).

[15] W. Zhong, R. D. King-Smith, and D. Vanderbilt, Phys. Rev. Lett. **72**, 3618 (1994).

[16] J. Kobayashi, Y. Uesu, and Y. Sakemi, Phys. Rev. B **28**, 3866 (1983).

[17] W. Zhong and D. Vanderbilt (unpublished).

[18] M. P. Allen and D. J. Tildesley, *Computer Simulation of Liquids* (Oxford, New York, 1990); *The Monte Carlo Method in Condensed Matter Physics*, edited by K. Binder (Springer-Verlag, Berlin, 1992).

[19] G. Shirane and Y. Yamada, Phys. Rev. **177**, 858 (1969); W. Buyers and R. Cowley, Solid State Commun. **7**, 181 (1969).

[20] K. A. Müller and H. Burkard, Phys. Rev. B **19**, 3593 (1979); K. A. Müller, W. Berlinger, and E. Tosatti, Z. Phys. B **84**, 277 (1991).

[21] R. Viana *et al.*, Phys. Rev. B **50**, 601 (1994).

[22] R. Martonak and E. Tosatti, Phys. Rev. B **49**, 12596 (1994).

[23] B. Okai and J. Yoshimoto, J. Phys. Soc. Jpn. **39**, 162 (1975).

Effect of quantum fluctuations on structural phase transitions in $SrTiO_3$ and $BaTiO_3$

W. Zhong and David Vanderbilt

Department of Physics and Astronomy, Rutgers University, Piscataway, New Jersey 08855-0849
(Received 20 September 1995)

Using path-integral Monte Carlo simulations and an *ab initio* effective Hamiltonian, we study the effects of quantum fluctuations on structural phase transitions in the cubic perovskite compounds $SrTiO_3$ and $BaTiO_3$. We find quantum fluctuations affect ferroelectric (FE) transitions more strongly than antiferrodistortive (AFD) ones, even though the effective mass of a single FE local mode is larger. For $SrTiO_3$ we find that the quantum fluctuations suppress the FE transition completely, and reduce the AFD transition temperature from 130 to 110 K. For $BaTiO_3$, quantum fluctuations do not affect the order of the transition, but do reduce the transition temperature by 35–50 K. The implications of the calculations are discussed.

Quantum fluctuations typically have a very important effect on the structural and thermodynamic properties of materials consisting of light atoms like hydrogen and helium. For example, quantum effects introduce large corrections to the calculated hydrogen density distribution in the Nb:H system.[1] For materials with heavier atoms, however, the quantum fluctuation can have only a small effect on the distribution of atomic displacements, and thus typically do not have a noticeable effect on the structural and thermodynamic properties of the material. However, exceptions may occur. As we shall see, the cubic perovskites can exhibit decisive quantum-fluctuation effects, despite the fact that the lightest constituent is oxygen. This can occur because these materials have several competing structures with very small structural and energetic differences.[2]

A good example is $SrTiO_3$. While it has the simple cubic perovskite structure at high temperature, $SrTiO_3$ goes through an antiferrodistortive (AFD) transition at 105 K to a tetragonal phase in which the oxygen octahedra have rotated in opposite senses in neighboring unit cells. The observed softening of the ferroelectric (FE) polar phonons with further reduction of temperature in the range 50–100 K would appear to extrapolate to a FE transition close to 20 K, but instead the softening saturates and no such transition is observed.[3] The absence of a true FE transition is suggested to be suppressed by quantum fluctuations, giving rise to a "quantum paraelectric" phase at very low temperature.[4] Some experiments appear to suggest a sharp transition to this low-temperature phase at about 40 K, perhaps indicating the formation of some kind quantum coherent state.[5,6] However, until a plausible candidate for the order parameter of the low-temperature phase is put forward, these ideas must remain highly speculative.

These developments have stimulated many theoretical efforts to understand the quantum effects in $SrTiO_3$.[4,7–9] However, the previous work has all been qualitative or empirical in approach. Although it was shown that quantum zero-point motion is capable of suppressing phase transitions,[9] a detailed microscopic approach is needed to gain a quantitative and detailed understanding of the quantum effects at finite temperature. Recently, an *ab initio* effective-Hamiltonian scheme has been developed to study structural phase transitions of cubic perovskites. It has been successfully applied to

$BaTiO_3$ (Refs. 10 and 11) and $SrTiO_3$,[12,13] giving good agreement with experimental observations. Treating atomic motion classically, it predicted FE phase transitions for $SrTiO_3$ at low temperature, thus giving indirect support for the notion that quantum fluctuations (not included in the theory) must be responsible for the observed absence of a low-temperature FE phase.

In the present work, we have extended the previous treatment of the first-principles based effective Hamiltonian to include quantum fluctuations. In particular, we use path-integral (PI) quantum Monte Carlo simulations to study the effect of quantum fluctuations on the structural phase transitions in $SrTiO_3$ and $BaTiO_3$. For $SrTiO_3$, we find that the quantum fluctuations have only a modest effect on the AFD transition temperature, while the FE transition is suppressed entirely. We discuss the relative importance of AFD and FE quantum fluctuations in some detail, and examine the potential implications of our results for understanding the low-temperature behavior of the material. For $BaTiO_3$, in which the FE transitions occur at higher temperature, we find that the quantum effects are less dramatic.

We start by reviewing the effective Hamiltonian and its construction. Two approximations are involved. First, since both the FE and AFD transitions involve only small structural distortions, we represent the energy surface by a Taylor expansion around the high-symmetry cubic perovskite structure, including up to fourth-order anharmonic terms. Second, because only low-energy distortions are important to the structural properties, we include only three such distortions in our expansion: the soft FE mode, the AFD mode, and an elastic mode. These are represented, respectively, by local-mode amplitudes $\mathbf{f}_i$, $\mathbf{a}_i$, and $\mathbf{u}_i$, where i is a cell index. The local modes are constructed in such a way that a uniform (or, for AFD, a uniformly staggered) arrangement of the mode vectors represents the desired low-energy excitation.[11] Thus, we work with local-mode vectors instead of atomic displacements. This reduces the number of degrees of freedom from 15 to 9 per cell and greatly reduces the complexity of the Taylor expansion. The Hamiltonian is specified by a set of expansion parameters determined using highly accurate first-principles calculations with Vanderbilt ultrasoft pseudopotentials.[14] The details of the Hamiltonian, the first-

principles calculations, and the values of the expansion parameters have been reported elsewhere.[10–13]

In our previous work, we have used this effective Hamiltonian by applying Monte Carlo simulation techniques to study the thermodynamics of the system in the classical limit. Assuming the ionic motions are classical is usually a good approximation for systems such as cubic perovskites containing atoms no less massive than oxygen. However, the structural differences and energy barriers between the cubic structure and the possible (rhombohedral or tetragonal) distorted structures are very small. A rough estimate of the importance of quantum fluctuations can be obtained from the Heisenberg uncertainty principle $\Delta p \cdot \Delta q \geq \hbar/2$, or equivalently,

$$\Delta E \geq \hbar^2/(8m\Delta q^2). \tag{1}$$

Here, Δq denotes the uncertainty in the structural coordinate, which is related to the structural difference between phases. ΔE is the energy uncertainty, or zero-point energy, which may prevent the occurrence of the distorted phase if it is larger than the classical free-energy reduction. So if the structural and energetic differences between phases are small enough, quantum suppression may occur even for fairly massive ions. For a quantitative understanding, we need to perform statistical simulations that treat the ionic motion quantum mechanically.

Here, we adopt the path-integral (PI) technique[15] of quantum simulations, which has proven to be a very successful method for studying H- and He-related systems.[1,16] The method is based on Feynman's PI formulation of quantum mechanics.[17] This formulation states that the partition function of the original quantum-statistical systems of particles can be approximated by the partition function of P subsystems of classical particles with each quantum particle replaced by a cyclic chain of P beads coupled by harmonic springs. Each subsystem (comprising one bead from each chain) has internal interactions identical to the reference classical system, except for a reduction in strength by a factor $1/P$. The spring constant of the harmonic springs coupling the beads inside a certain cyclic chain is $mP/\hbar^2\beta^2$, where m is the mass of the quantum particle and β the inverse temperature $(k_B T)^{-1}$. This approximation becomes exact when the number of beads $P \to \infty$, but in practice almost exact results can be obtained with a finite P depending on the system of interest. This way, thermodynamic properties of the N-particle quantum system can be obtained from the study of a $(P \times N)$-particle classical system.

The only extra inputs we need are the masses of all the "particles" in our system. The degrees of freedom in our Hamiltonian are the three local-mode amplitude vectors $\mathbf{f}_i$, $\mathbf{a}_i$, and $\mathbf{u}_i$ associated with each unit cell i. Each local mode involves displacements of several ions. If we regard each local vector as representing the displacement of some "pseudoparticle," the mass of each such pseudoparticle can be determined from all the ionic displacements involved. Since two local-mode vectors may involve the same ion, we actually have a nondiagonal mass matrix. For example, the mass matrix elements between local modes $\mathbf{f}_i$ and $\mathbf{f}_j$, or equivalently, $f_{i\alpha}$ and $f_{j\beta}$, can be constructed through

$$m_{i\alpha,j\beta} = \xi(i\alpha) \cdot M \cdot \xi(j\beta). \tag{2}$$

Here, i and j are the cell indices, while α and β denote Cartesian components. $\xi(i\alpha)$ is the eigenvector describing atomic displacements associated with local mode $f_{i\alpha}$, and M is a (diagonal) mass matrix in the $15L^3$-dimensional space of atomic displacements of our $L \times L \times L$ supercell. Similarly, mass matrix elements connecting different kinds of local vectors, such as those between $\mathbf{f}_i$ and $\mathbf{a}_i$, are also included. The entire mass matrix can be calculated once and for all, and the extension of the PI technique to handle a nondiagonal mass matrix is straightforward.

The study of the thermodynamic properties of the classical system is performed using Monte Carlo (MC) simulations.[18] The original simulation cell is an $L \times L \times L$ cube, with three vectors $\mathbf{f}_i$, $\mathbf{a}_i$, and $\mathbf{u}_i$ at each lattice point i. Periodic boundary conditions are used, and homogeneous strains of the entire supercell are included. Each local vector is converted to a string of P beads, so that we have $9PL^3$ degrees of freedom per simulation supercell. We use a single-flip algorithm, making trial moves of the vectors at each site in turn and testing acceptance after each move. We say that one Monte Carlo sweep (MCS) has been completed when all vectors on all sites have been tried once. Because of the 1% lattice-constant error in our local-density approximation (LDA) calculations and the strong sensitivity of the structural transitions to the lattice constant, all our simulations are performed at a negative pressure to restore the experiment lattice constant, as in our previous work.[10–13]

The Trotter number P should be large enough to ensure that the quantum effects are correctly accounted for. On the other hand, the computational load increases rapidly with increasing P, because of both larger system size and longer correlation time with larger P. In our simulation, the proper Trotter number for each temperature is chosen empirically. For a certain temperature, we simulate systems with increasing Trotter number $P = 1, 2, 4, 8, 16, \ldots$. We equilibrate systems with each P and monitor their order parameters. We determine that the P is large enough if the monitored quantities converge. If a certain quantity is sensitive to P, its value at $P = \infty$ can be extrapolated following the formula $a_0 + a_1/P + a_2/P^2$ (Ref. 19).

We concentrate on $SrTiO_3$ and study the effect of quantum fluctuation on both FE and AFD phase transitions. In Fig. 1, we show the FE and AFD order parameters $\mathbf{f}(\Gamma)$ and $\mathbf{a}(R)$ as a function of temperature for a $12 \times 12 \times 12$ simulation cell. The classical data (previously published in Ref. 12) are produced by a cooling-down simulation, starting at 250 K and cooling down gradually, equilibrating and then simulating to obtain the order parameters.[12] The quantum simulations are performed with $P = 4$, which is found to give converged results for $T > 60$ K and qualitatively correct results for $T > 20$ K. We use the equilibrium configuration from the classical simulations ($P = 1$) as the starting configuration. We find the system reaches equilibrium faster this way than it does if gradually cooled and the results are less affected by hysteresis. The system is equilibrated for 10 000 MCS's, and then another 30 000–70 000 MCS's are used to obtain the reported thermodynamic averages.

Figure 1 shows that the quantum fluctuations do affect both the AFD and FE phase transitions. The AFD phase transition temperature decreases from 130 K to 110 K when the quantum fluctuations are turned on, bringing the results into
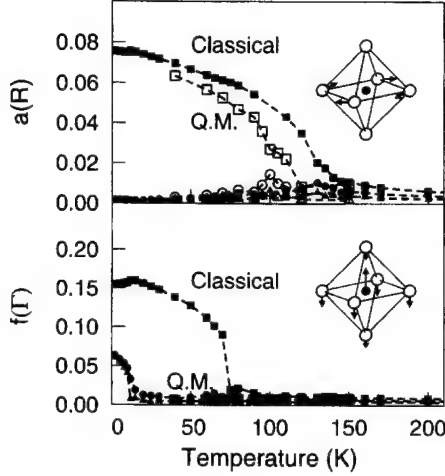
FIG. 1. AFD and FE order parameters $\mathbf{a}(R)$ and $\mathbf{f}(\Gamma)$ as a function of temperature for a $12 \times 12 \times 12$ SrTiO$_3$ simulation cell. Squares, circles, and triangles indicate the largest, intermediate, and smallest components of the order parameter, respectively. Filled symbols are from classical simulations, while open symbols are from path-integral simulations with $P=4$ (the latter for the FE case are nearly zero and are thus not very visible). Insets indicate schematically the nature of the AFD and FE distortions.

better agreement with the experimental result of 105 K. On the other hand, the quantum fluctuations can be seen to have completely suppressed the FE phase transitions, at least down to 40 K. Further simulations going as high as $P=20$ place an upper bound of about 5 K on any possible FE phase transition temperature. Thus, we conclude that quantum fluctuations almost certainly suppress the FE phase transitions completely, resulting in a paraelectric phase down to $T=0$.

Since the effect of quantum fluctuations is more dramatic on the FE transitions, we analyze this case in more detail. In the paraelectric phase, the fluctuation of the FE local-mode vector $\mathbf{f}$ has both quantum and thermal contributions. We identify the thermal fluctuations as those associated with the fluctuations of the center of gravity of the cyclic chain. More specifically, letting $\mathbf{f}(i,s,t)$ represent $\mathbf{f}$ on lattice site i, Trotter slice s, and MCS t, the thermal fluctuation can be obtained from our simulation using

$$(\Delta f^{\text{thermal}})^2 = \langle \langle f \rangle_s^2 \rangle_{i,t}, \qquad (3)$$

while the total fluctuation is

$$(\Delta f^{\text{total}})^2 = \langle f^2 \rangle_{i,s,t}. \qquad (4)$$

Here the brackets represent the indicated average. The part of fluctuation due solely to the quantum effects can be obtained from $(\Delta f^{\text{QM}})^2 = (\Delta f^{\text{total}})^2 - (\Delta f^{\text{thermal}})^2$. The result for a $10 \times 10 \times 10$ lattice is shown in Fig. 2. The results are obtained from simulations at several small Trotter numbers and then extrapolated to $P=\infty$ using the formula $a_0 + a_1/P + a_2/P^2$. As expected, the thermal fluctuation decrease with decreasing temperature, while the quantum fluctuations increase. Below 70 K, the quantum fluctuations dominate.

Recent experiments suggest there may be a weak signature of a phase transition in SrTiO$_3$ around 40 K.[5] This was
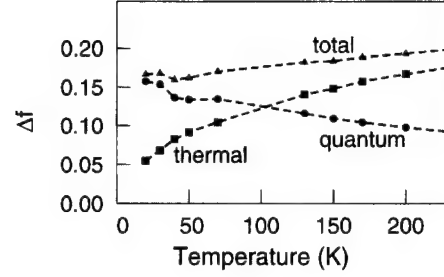

FIG. 2. Classical (squares), quantum (circles), and total (triangles) RMS fluctuation of the FE local-mode vectors [Eqs. (3) and (4)] in SrTiO$_3$ as a function of temperature.

tentatively suggested to be a phase transition to a coherent quantum state in which small FE domains propagate through the crystal. Because the size of our simulation cell is much smaller than the domain size suggested, we expect that such a state would appear as a real FE phase in our simulation. This is not observed. However, our simulation does reveal some changes in the character of the FE fluctuations at low temperature. A typical FE fluctuation at high temperature resembles the soft eigenvector of the force-constant matrix, which is independent of the masses, since the classical thermodynamic properties are related only to the potential energy. However, the quantum fluctuations are quite sensitive to the ionic masses, and at low temperature the fluctuations of light (primarily oxygen-related) degrees of freedom are accentuated. This crossover in the character of the fluctuations occurs gradually below 100 K, and we suspect that it might possibly be responsible for the experimentally observed anomalies which were interpreted in terms of a phase transition. If this is the case, the "quantum paraelectric" phase at very low temperature is probably not separated by a true phase transition from the classical paraelectric phase at higher temperature.

To better characterize the impact of the quantum effects on FE transitions, we also apply the PI simulations to BaTiO$_3$. The results are summarized in Table I. The simulation procedure is the same as for SrTiO$_3$, except that the AFD degrees of freedom are neglected in BaTiO$_3$ because of their high energy. Experimentally, BaTiO$_3$ has four phases in the sequence cubic (C), tetragonal (T), orthorhombic (O), and rhombohedral (R) with decreasing temperature. Our classical simulations correctly reproduce this transition sequence, and give transition temperatures that are in reasonable agreement with ($\sim$ 15–30% below) the experimental ones. We have argued previously that the quantitative discrepancy can probably be traced to the LDA lattice-constant

TABLE I. The effect of quantum fluctuations on the FE transition temperatures in BaTiO$_3$, for a $12 \times 12 \times 12$ supercell. R, O, T, and C indicate rhombohedral, orthorhombic, tetragonal, and cubic phases, respectively.

Phase	Classical	Quantum	Expt.
$O-R$	200 ± 10	150 ± 10	183
$T-O$	232 ± 2	195 ± 5	278
$C-T$	296 ± 1	265 ± 5	403

error.[10,11] Here, we find that, with quantum effects included, the calculated transition sequence is still the same, while the transition temperatures are reduced further by 35 to 50 K. Although the absolute transition temperatures are thus in slightly worse agreement with experiment, the spacing between phases is more reasonable. In any case, it is clear that the quantum effects can have a substantial effect on the FE transition temperatures even up to several hundreds of degrees K, a result which was not obvious from the outset.

It may appear counterintuitive that quantum effects on the FE instability are much stronger than on the AFD instability in $SrTiO_3$. After all, the AFD instability involves only the motion of oxygen atoms, while the FE instability involves mainly Ti atoms which are three times heavier than the oxygen atoms. A partial explanation can be drawn from the fact that the structural change involved in the FE distortion (0.1 a.u. for Ti in $SrTiO_3$) is much smaller than for the AFD distortion (0.3 a.u. for O). As a result, $m\Delta q^2$ turns out to be three times larger for the AFD case, even though the effective mass is smaller. Thus, according to Eq. (1), the effect of the quantum fluctuations will be less significant for the AFD case.

We think a more fundamental explanation may be found in the stronger spatial correlations between AFD distortions. In the cubic phase, the spatial correlations for the FE local vectors are chainlike or quasi-one-dimensional (1D): $f_z(\mathbf{R}_i)$ correlates strongly only with $f_z(\mathbf{R}_i \pm na\hat{\mathbf{z}})$, where n is a small integer number and a is the lattice constant.[20,13] This correlation is due to the strong Coulomb interactions between FE local modes,[21] which strongly suppress longitudinal excitations relative to transverse ones. With the correla-

tion length estimated at $10a$,[13] we can roughly say that about ten local-mode vectors are "bound together" and the effective mass becomes ten times larger. On the other hand, the AFD modes, associated with rotation of the oxygen octahedral, correlate strongly with each other because of the rigidity of the octahedral unit. The correlation region is 2D disclike: $a_z(\mathbf{R}_i)$ correlates strongly with $a_z(\mathbf{R}_i \pm na\hat{\mathbf{x}} + ma\hat{\mathbf{y}})$, where m is again a small integer. The AFD correlation length is comparable with the FE one,[13] but now the 2D nature implies that roughly 100 mode vectors are tied together, for a mass enhancement of 100 instead of just 10. Thus, this effect weakens the quantum fluctuations much more for the AFD than for the FE case, and one should generally expect quantum suppression of phase transitions to be stronger in the FE case.

In summary, we have applied the PI technique to study the effect of quantum fluctuations on FE and AFD phase transitions in $SrTiO_3$ and $BaTiO_3$. We find that the quantum fluctuations have a weaker effect on the AFD transition than on the FE one, because the AFD modes are more strongly correlated with each other. In the case of $SrTiO_3$, we find that the FE phase is suppressed entirely, thereby supporting the notion of "quantum paraelectric" behavior (though not necessarily a distinct phase) at very low temperature. The AFD transition temperature is found to be only slightly reduced. For $BaTiO_3$, we find that the quantum effects preserve the transition sequence and reduce the transition temperatures modestly.

[1] M. J. Gillan, Phys. Rev. Lett. **58**, 563 (1987).

[2] M. E. Lines and A. M. Glass, *Principles and Applications of Ferroelectrics and Related Materials* (Clarendon, Oxford, 1977).

[3] R. Viana *et al.*, Phys. Rev. B **50**, 601 (1994).

[4] K.A. Müller and H. Burkard, Phys. Rev. B **19**, 3593 (1979).

[5] K.A. Müller, W. Berlinger, and E. Tosatti, Z. Phys. B **84**, 277 (1991).

[6] R. Vacher *et al.*, Europhys. Lett. **17**, 45 (1992); O. M. Nes, K. A. Müller, T. Suzuki, and F. Fossheim, *ibid.* **19**, 397 (1992); E. V. Balashova *et al.*, Solid State Commun. **94**, 17 (1995).

[7] R. Martonak and E. Tosatti, Phys. Rev. B **49**, 12 596 (1994).

[8] J. H. Barrett, Phys. Rev. **86**, 118 (1952).

[9] T. Schneider, H. Beck, and E. Stoll, Phys. Rev. B **13**, 1123 (1976).

[10] W. Zhong, D. Vanderbilt, and K. M. Rabe, Phys. Rev. Lett. **73**, 1861 (1994).

[11] W. Zhong, D. Vanderbilt, and K. M. Rabe, Phys. Rev. B **52**, 6301 (1995).

[12] W. Zhong and D. Vanderbilt, Phys. Rev. Lett. **74**, 2587 (1995).

[13] W. Zhong and D. Vanderbilt (unpublished).

[14] D. Vanderbilt, Phys. Rev. B **41**, 7892 (1990).

[15] J. Barker, J. Chem. Phys. **70**, 2914 (1979); D. Chandler and P. G. Wolynes, *ibid.* **74**, 7 (1981); *Monte Carlo Methods in Quantum Problems*, edited by M. H. Kalos (Reidel, Dordrecht, 1984).

[16] D. Ceperley, Rev. Mod. Phys. **67**, 279 (1995); E. Kaxiras and Z. Guo, Phys. Rev. B **49**, 11 822 (1994).

[17] R. P. Feynman, *Statistical Mechanics* (Benjamin, Reading, MA, 1972).

[18] M. P. Allen and D. J. Tildesley, *Computer Simulation of Liquids* (Oxford, New York, 1990); *The Monte Carlo Method in Condensed Matter Physics*, edited by K. Binder (Springer-Verlag, Berlin, 1992).

[19] A. Cuccoli *et al.*, Phys. Rev. B **51**, 12 369 (1995).

[20] R. Yu and H. Krakauer, Phys. Rev. Lett. **74**, 4067 (1995).

[21] W. Zhong, R. D. King-Smith, and D. Vanderbilt, Phys. Rev. Lett. **72**, 3618 (1994).

First-principles study of stability and vibrational properties of tetragonal PbTiO$_3$

Alberto García*

Departamento de Física Aplicada II, Universidad del País Vasco, Apartado 644, 48080 Bilbao, Spain

David Vanderbilt

Department of Physics and Astronomy, Rutgers University, Piscataway, New Jersey 08855-0849

A first-principles study of the vibrational modes of PbTiO$_3$ in the ferroelectric tetragonal phase has been performed at all the main symmetry points of the Brillouin zone (BZ). The calculations use the local-density approximation and ultrasoft pseudopotentials with a plane-wave basis, and reproduce well the available experimental information on the modes at the Γ point, including the LO-TO splittings. The work was motivated in part by a previously reported transition to an orthorhombic phase at low temperatures [(J. Kobayashi, Y. Uesu, and Y. Sakemi, Phys. Rev. B **28**, 3866 (1983).] We show that a linear coupling of orthorhombic strain to one of the modes at Γ plays a role in the discussion of the possibility of this phase transition. However, no mechanical instabilities (soft modes) are found, either at Γ or at any of the other high-symmetry points of the BZ. [S0163-1829(96)04529-8]

I. INTRODUCTION

Due to their relatively simple structure and the variety of phenomena they exhibit, the perovskite oxides have become important subjects of study. Despite sharing a common formula ABO_3 and a highly symmetric high-temperature structure (Fig. 1), this family of compounds presents a rich and varied low-temperature phenomenology. Among the perovskites one finds ferroelectric crystals such as BaTiO$_3$ and PbTiO$_3$, antiferroelectrics such as PbZrO$_3$ and NaNbO$_3$, and materials such as SrTiO$_3$ that exhibit other, nonpolar instabilities.

Much progress has been made in the last 50 years in the experimental characterization of the properties of these compounds. One of the main conclusions to emerge from these studies is the fascinating dependence of the structural and dynamical behavior on details of chemical composition. Indeed, even within a given subgroup of materials one finds significantly different phase diagrams. For example, BaTiO$_3$ exhibits a complicated sequence of phase transitions, from cubic to tetragonal to orthorhombic to rhombohedral, while PbTiO$_3$ shows just one clearly established transition with $T_c = 493°C$ from the cubic paraelectric phase to a tetragonal ferroelectric structure. Moreover, the replacement of Pb for Ba also has important consequences for the dynamical processes leading to the transition. It is acknowledged that the soft mode in BaTiO$_3$ is highly overdamped, and therefore that the transition has some order-disorder flavor, whereas PbTiO$_3$ has been called a "textbook example of displacive transition."[1]

Until recently, however, theoretical models of perovskite properties could not properly take into account the fine chemical details that distinguish the behavior of the different materials in this family. Semi-empirical methods are not accurate enough to model the sort of delicate balance between effects (long-range dipole interactions vs short-range covalent and repulsion forces, for example), and schemes based on model Hamiltonians are usually too simple and too fo-

cused on a given material to be of much use in the unraveling of the chemical trends within the perovskites.

This situation has improved in the last few years with the use of accurate first-principles density-functional calculations to study the energy surfaces[2-4] and even the temperature-dependent phase diagrams[5-7] of various perovskite oxides. These works have achieved a high degree of success in reproducing qualitatively and even quantitatively the experimental observations, giving us confidence that one can now carry out accurate calculations to elucidate microscopic behavior (importance of hybridization, competition between long-range and short-range interactions, etc). A

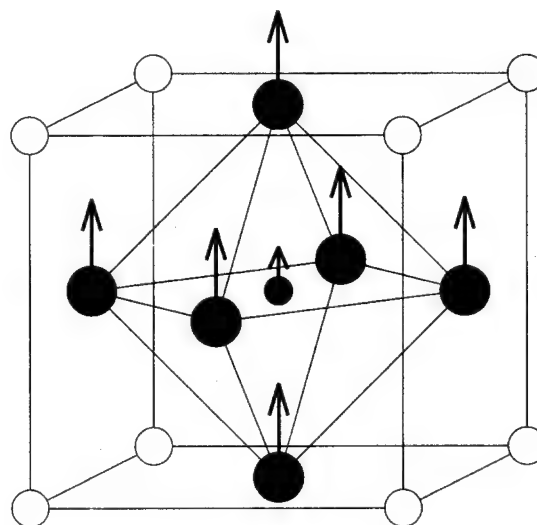FIG. 1. Structure of ferroelectric (tetragonal) PbTiO$_3$. The arrows represent the displacements of the atoms with respect to their positions in the cubic high-temperature phase. Pb atoms are depicted by open circles, the Ti atom by the black dot in the center of the cell, and the O atoms (O$_1$, O$_2$, and O$_3$, displaced from the Ti atom along x, y, and z, respectively) by shaded circles.

good example is the recent work of Rabe and Waghmare,[7] which has helped revise the conventional wisdom relative to the behavior of $PbTiO_3$. Indications of a problem with the simple displacive picture were first seen experimentally in extended x-ray absorption fine-structure measurements,[8] but the theoretical work[7] has provided the microscopic underpinnings of a partial order-disorder character of the cubic-tetragonal transition in which the atomic distortions in the high-temperature phase are proposed to arise from a local instability.

Another issue, with which we will be mainly concerned in this paper, is the possible existence of a low-temperature transition. In the 1950s, Kobayashi et al.[9] reported the observation of what appeared to be a distorted ("multiple") tetragonal phase of $PbTiO_3$ below approximately $-100°C$. After several negative attempts by other researchers to reproduce the observations,[10] x-ray and optical measurements were presented[11] as corroborating the existence of a low-temperature phase with an orthorhombic structure. The transition, at $-90°C$, would be second order, and bring about a very slight distortion of the tetragonal phase (with the orthorhombic cell parameters a and b differing by just 4.5×10^{-4} Å at $-194°C$) and the direction of the lattice vectors kept unchanged. The absence of superlattice reflections would imply a symmetry distortion without multiplication of the size of the unit cell.

From the point of view of the microscopic dynamics of the tetragonal structure, such a transition could be explained by a mechanical instability of a zone-center phonon whose associated atomic distortions break the tetragonal symmetry and thus relax the requirement that a and b be equal. At $T=0$ the energy surface should then present a saddle point at the configuration corresponding to the tetragonal phase, with the energy decreasing along a coordinate representing the amplitude of the soft mode and the coupled orthorhombic strain.

In this paper we have used first-principles calculations to study possible mechanical instabilities in the ferroelectric tetragonal phase of $PbTiO_3$. Our focus has been primarily on homogeneous (zone-center) distortions of the tetragonal symmetry, aimed at a detailed theoretical assessment of the possibility of the phase transition suggested by Kobayashi et al.[11] However, in the interest of completeness, we have also carried out an analysis of the normal modes at all the main symmetry points on the surface of the Brillouin zone (BZ). Thus we also present a fairly complete collection of normal-mode frequencies and eigenvectors for ferroelectric $PbTiO_3$ computed from first principles.

The paper is organized as follows. In Sec. II we undertake a classification of the types of possible distortions of the tetragonal phase of $PbTiO_3$ according to their symmetry. Section III briefly describes some technical aspects of our calculations, whose results are presented in Sec. IV. Section V discusses the implications of our work for the likelihood of a low-temperature transition in $PbTiO_3$. The Appendix is devoted to some issues related to the coupling of atomic displacements to strain degrees of freedom.

II. THEORETICAL ANALYSIS OF POSSIBLE INSTABILITIES

In the harmonic approximation, the calculation of phonon frequencies and mode displacement patterns involves the di-

TABLE I. Character table and decomposition of the vector and second-order symmetric tensor representations for point group $4mm$.

	E	C_4, C_4^{-1}	C_2	m_x, m_y	$m_d, m_{d'}$	V	$Sym[V \times V]$
A_1	1	1	1	1	1	z	x^2+y^2, z^2
A_2	1	1	1	-1	-1		
B_1	1	-1	1	1	-1		x^2-y^2
B_2	1	-1	1	-1	1		xy
E	2	0	-2	0	0	(x,y)	(zx, yz)

agonalization of the dynamical matrix, itself obtained in a straightforward manner from the force constants $\Phi_{ij}^{\alpha\beta}$ which enter the expansion of the energy to second order in the atomic displacements,

$$E = E_0 + \sum_{ij\alpha\beta} \Phi_{ij}^{\alpha\beta} u_\alpha^i u_\beta^j. \tag{1}$$

The force constants can easily be calculated by computing all the forces caused by a given sublattice displacement.

It is well-known that the normal modes of vibration of a crystal at a given k point of the BZ transform according to irreducible representations of the group of the wave vector. Thus a judicious use of the symmetry information available simplifies the analysis and saves computational work. Symmetry arguments can also profitably be used to determine the form of the series expansion of the total energy of the crystal around a given configuration, including the correct couplings among various degrees of freedom (such as atomic displacements and strains). This is precisely what is needed for a detailed study of the energy surface and the possible appearance of mechanical instabilities.

In this section we present a brief account of the use of symmetry considerations to characterize the possible instabilities of the tetragonal ferroelectric phase of $PbTiO_3$. Experimentally,[11] it has been claimed that the low-temperature structure has orthorhombic symmetry and there is no sign of cell doubling. Accordingly, we devote a subsection to the study of zone-center instabilities of orthorhombic character, and to the investigation of the form of the energy as a function of the relevant degrees of freedom. A second subsection considers distortions that might conceivably lead to a low-temperature phase transition but involve a nonorthorhombic symmetry or a doubling of the unit cell.

A. Orthorhombic instabilities with no cell doubling

The ferroelectric phase of $PbTiO_3$ (Fig. 1) is tetragonal, with space group $P4mm$. At the Γ point, the group of the wave vector is the point group of the crystal, $4mm$, characterized by a fourfold rotation axis and four symmetry planes which contain it. Table I displays the character table for $4mm$. There are five symmetry classes and thus five irreducible representations (irreps), of which one (E) is two-dimensional.

The decomposition of the vibrational representation at Γ can be shown by standard techniques to be

$$Vib(\Gamma) = 4A_1 \oplus B_1 \oplus 5E. \tag{2}$$

TABLE II. Symmetry analysis of the normal modes at different points of the BZ.

$\mathbf{k}$, (Group)	Irrep	No. of copies	Basis
Γ,Z (4mm)			
	A_1	4	$Pb_z, Ti_z, O_{1z}+O_{2z}, O_{3z}$
	B_1	1	$O_{1z}-O_{2z}$
	E	5 (2D)	$Pb_x, Ti_x, O_{1x}, O_{2x}, O_{3x}$
			$Pb_y, Ti_y, O_{1y}, O_{2y}, O_{3y}$
X,M' (mm2)			
	A_1	5	$Pb_z, Ti_x, O_{1z}, O_{2z}, O_{3x}$
	A_2	3	Ti_y, O_{2y}, O_{3y}
	B_1	2	Pb_y, O_{1y}
	B_2	5	$Pb_x, Ti_z, O_{1x}, O_{2z}, O_{3z}$
M,R (4mm)			
	A_1	2	$Pb_z, O_{1y}+O_{2x}$
	A_2	1	$O_{1x}-O_{2y}$
	B_1	1	$O_{1y}-O_{2x}$
	B_2	3	$Ti_z, O_{1x}+O_{2y}, O_{3z}$
	E	4 (2D)	$Pb_x, Ti_y, O_{2z}, O_{3y}$
			$Pb_y, Ti_x, O_{1z}, O_{3x}$

Physically, this means that the problem of diagonalizing the 15×15 dynamical matrix reduces to three simpler tasks: the diagonalization of a 4×4 matrix to decouple the four copies of the A_1 irrep, a similar 5×5 diagonalization for E, and a simple calculation of a force constant to obtain the frequency of the B_1 mode (its displacement pattern being completely determined by symmetry). The atomic motions are, therefore, coupled only within subspaces of the original 15-dimensional configuration space. The four-dimensional A_1 subspace corresponds to coupled motions with basis $[Pb_z, Ti_z, O_{1z}+O_{2z}, O_{3z}]$ and the one-dimensional B_1 subspace represents a normal mode with a displacement pattern of the form $[O_{1z}-O_{2z}]$. Of course, at Γ there are three zero-frequency acoustic modes. Two are degenerate (movements along x or y) and transform according to E, and the third is polarized along z and belongs to A_1. The complete symmetry specification of all the normal modes at Γ and at other high-symmetry k points appears in Table II.[13]

It is simple to use this symmetry information to analyze the possible mechanisms leading to the experimentally suggested phase transition from the tetragonal to an orthorhombic structure. By looking at the Γ entry in Table II and considering the characters in Table I, it can be immediately concluded that the B_1 mode has the right transformation properties. In this mode the O_1 and O_2 atoms move in opposite directions along the z axis, thus breaking the fourfold symmetry.

A calculation of the frequency of this mode is not enough to determine the existence of an instability, since one should take into account possible couplings of the atomic displacements to changes in the size and shape of the unit cell (strain variables). The possible strains that can be applied to the cell are represented by the components of a second-order symmetric tensor (η), and can be classified according to irreducible representations of the point group of the crystal as shown in the last column in Table I. In what follows we use the notation

$$r = \eta_{zz},$$

$$s = (\eta_{xx}+\eta_{yy})/2,$$

$$t = (\eta_{xx}-\eta_{yy})/2.$$

Portions of η transforming according to the identity representation A_1 leave the tetragonal symmetry unchanged. Such is the case for r and s, which refer to symmetric axial and in-plane strains, respectively. The other strain irreps are associated with lower lattice symmetries: monoclinic for E, and orthorhombic for B_1 and B_2. While a B_2 (η_{xy}) distortion leads to an orthorhombic structure with axes rotated by 45° with respect to the tetragonal basis, a pure B_1 (t) strain transforms the cell into an orthorhombic one without a change in the orientation of the axes. The latter is precisely the kind of low-temperature phase suggested for PbTiO$_3$.[11]

Apart from the change in the orientation of the axes, there is an important difference between B_2 (η_{xy}) and B_1 (t) cell distortions. Since the orthorhombic strain t transforms according to the B_1 irrep, it can couple *linearly* to the B_1 normal coordinate.[14] Therefore, the crystal energy expansion considering only the B_1 mode and strain is of the form

$$E = E_0 + \tfrac{1}{2}ku^2 + \tfrac{1}{2}Ct^2 + \gamma ut + \cdots . \quad (3)$$

It is shown in the Appendix that the linear coupling in Eq. (3) implies a renormalization $C_{\text{eff}}=C-\gamma^2/k$. Thus strain coupling could create instabilities against B_1 (orthorhombic) distortions even if the "bare" second-order coefficients k and C are positive.

In contrast, any coupling of the B_2 strain to a given atomic displacement u must be at least of second order,

$$E = E_0 + \tfrac{1}{2}ku^2 + \tfrac{1}{2}C\eta_{xy}^2 + + \gamma u^2 \eta_{xy}^2 + \alpha u^4 + \beta \eta_{xy}^4 + \cdots , \quad (4)$$

with no renormalization of the elastic constant C (see the Appendix).

In summary, if the purported low-temperature phase transition in PbTiO$_3$ is indeed to an orthorhombic phase with no cell doubling, and with the basis parallel to the tetragonal one, it should be linked to a negative effective elastic constant C_{eff} for a t strain. If one allows for the possibility of a rotation of the axes, the transition could be associated with a negative "bare" elastic constant for a B_2 strain.

B. Other instabilities

Apart from the experimentally suggested instability of the tetragonal phase in favor of an orthorhombic structure with no cell doubling, there are, in principle, other distortions that might conceivably lead to phase transitions. To begin with, and by reference to Table I, one could think of an instability leading to a phase with monoclinic symmetry (but still without multiplying the size of the unit cell) associated with distortions transforming according to the E irreducible representation. The analysis of this case is conceptually very similar to the one carried out for the B_1 distortions, with the difference that there are eight optical E modes capable of coupling to strain (four for each of the rows of the two-dimensional irrep E). Thus x- and y-polarized normal modes
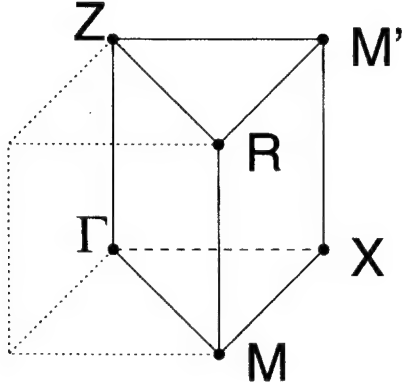
FIG. 2. Sketch showing the irreducible wedge of the Brillouin zone associated with the $P4mm$ space group, and the positions of the symmetry points considered in this work.

will couple linearly to xz and yz strains, respectively, resulting in a renormalized elastic constant C_{eff} for E distortions.

Next to consider is the possibility of structural phase transitions associated with a multiplication of the size of the unit cell. These would come about through the instability of non-Γ modes. Since there is no possibility of coupling of these modes to homogeneous strain at first order, one needs only to compute the eigenvalues of the force-constant matrix to check for any saddle points in the energy surface. It is not feasible to study the modes at all the wave vectors in the BZ, so we focus on a few high-symmetry k-points on the zone surface (see Fig. 2) which represent cell-doubling distortions.

The symmetry analysis of zone-boundary modes proceeds along the same lines as those for Γ. Operations that leave the wave vector invariant will, in general, form subgroups of $4mm$. For the purposes of our work it suffices to consider just one more point group, $mm2$, whose character table is given in Table III.[12] We show the symmetry decomposition of atomic displacements at the zone-boundary points in Table II.

III. DETAILS OF CALCULATIONS

The determination of the force constants involves the consideration of appropriately distorted crystal configurations. Symmetry arguments are used to reduce to the minimum the number of different calculations that need to be carried out, and to obtain the relevant information in the most direct form. For z-polarized modes at the Γ point, for example, it is only necessary to consider the four linearly independent atomic distortions $(1,0,0,0,0)$, $(0,1,0,0,0)$, $(0,0,1,-1,0)/\sqrt{2}$, and $(0,0,1,1,-2)/\sqrt{6}$, where the basis is formed by unit

TABLE III. Character table for the point group $mm2$. The symbols m_1, m_2 stand for m_x, m_y or m_d, $m_{d'}$, depending on the orientation of the axes.

	E	C_2	m_1	m_y
A_1	1	1	1	1
A_2	1	1	-1	-1
B_1	1	-1	1	-1
B_2	1	-1	-1	1

z displacements of Pb, Ti, O_1, O_2, and O_3.

Strain parameters are determined by subjecting the crystal to pure strains and fitting the energy to a polynomial form. The strain-phonon couplings are computed by finding the forces on the atoms caused by a suitable strain, since, from Eq. (3),

$$\left(\frac{\partial E}{\partial u}\right)_{u=0} = \gamma t. \tag{5}$$

We use ultrasoft pseudopotentials, a plane-wave basis set, and a conjugate-gradients algorithm to compute total energies and forces for a variety of crystal configurations. The method and the details of the pseudopotentials employed have been described elsewhere.[4] For this work we find that a $(4,4,4)$ Monkhorst-Pack[15] sampling of the BZ is enough to provide good precision in the calculated coefficients (see next section). Force constants are computed using the Hellmann-Feynman theorem, with atomic displacements of 0.002 in lattice units.

A final methodological note concerns the calculation of the frequencies of longitudinal optic (LO) modes at the Γ point. Since our calculations use periodic boundary conditions, we are not able to introduce a macroscopic electric field, such as it would arise in an ionic crystal in the presence of a $q \rightarrow 0$ longitudinal vibration. This field creates a splitting of the frequencies of infrared-active phonons, with the coupling constants being the ionic effective charges Z^*. The force-constant matrix has to be augmented by the effect of a screened (by electronic effects only) Coulomb interaction among those effective charges,

$$\Phi_{ij}^{\alpha\beta} \rightarrow \Phi_{ij}^{\alpha\beta} + \frac{4\pi e^2}{\Omega \epsilon_\infty} Z_i^* Z_j^* . \tag{6}$$

The effective charges can be obtained from first-principles calculations. Here we use those computed for cubic $PbTiO_3$ by Zhong and Vanderbilt.[16]

IV. RESULTS

A first concern is the determination of the structural parameters of the ferroelectric tetragonal phase of $PbTiO_3$. First-principles LDA calculations typically underestimate the lattice constants of perovskite oxides by around 1%. Our final objective is the study of dynamical properties of the crystal, and it would be debatable whether it is better to compute phonon frequencies and other dynamical parameters at the experimental or at the theoretical lattice constant. Past experience with perovskites has shown that the displacement patterns associated with some soft modes, and even the existence of the latter, depend on lattice constant and strain.[2,3] In the case of ferroelectric $PbTiO_3$ there is an additional complication, namely the existence of internal atomic displacements, which are of course coupled to the cell dimensions. Our first strategy was to use the experimental lattice constants $a = 7.380$ a.u., $c/a = 1.0635$ and optimize the internal atomic positions to obtain a base reference configuration with zero forces with which to compute phonon frequencies and strain coefficients. We call this "Theory I." Later we determined an optimized structure (cell shape and atomic positions coupled) via a special minimization proce-

TABLE IV. Structural parameters of $PbTiO_3$. Theory I and II refer to a relaxation with constrained lattice constants, and a free relaxation, respectively. z atomic coordinates are given in lattice units. Experimental values are taken from Ref. 21.

	Theory I	Theory II	Experiment
a (a.u.)	7.380	7.298	7.380
c/a	1.063	1.054	1.063
$z(Ti)$	0.549	0.537	0.540
$z(O_1,O_2)$	0.630	0.611	0.612
$z(O_3)$	0.125	0.100	0.112

dure (see the Appendix); we call this "Theory II." Table IV summarizes the structural information. While, as we shall see, we obtain substantially the same phonon frequencies in either case, the second approach, using as a reference the structure which gives a theoretical energy minimum with respect to strain, is, in principle, more appropriate for the calculation of elastic properties and strain-phonon couplings.

As part of the investigation of the possible mechanical instabilities,[17] we have obtained a complete set of calculated phonon frequencies for $PbTiO_3$. These are given, along with experimental results when available, in Tables V and VI.[18] The agreement of our theoretical results with experiment for the zone-center modes (both TO and LO) is quite good. We are thus confident that our computational approach can be trusted in its predictions of zone-edge vibrational frequencies that have not yet been determined experimentally. To our knowledge, the only other calculation of vibrational frequencies and modes for tetragonal $PbTiO_3$ was carried out by Freire and Katiyar.[19] An important difference with our work is that those authors used an empirical fitting procedure to adjust the parameters of a rigid-ion model. We use no empirical parameters of any kind, just the atomic numbers and masses of the atoms involved. Table V can be used also to

TABLE V. Frequencies of optical modes at Γ in cm^{-1}. Infrared-active modes exhibit LO-TO splitting. See text and Table IV for the meaning of Theory I and Theory II. Experimental values as compiled in Ref. 19.

	Theory I	Theory II	Experiment
A_1(TO)	151	146	147
A_1(TO)	355	337	359
A_1(TO)	645	623	646
E(TO)	81	82	88
E(TO)	183	195	220
E(TO)	268	237	289
E(TO)	464	501	505
B_1	285	280	289
A_1(LO)	187	186	189
A_1(LO)	449	447	465
A_1(LO)	826	799	796
E(LO)	114	125	128
E(LO)	267	273	289
E(LO)	435	418	436
E(LO)	625	675	723

TABLE VI. Computed frequencies of zone-edge phonons, classified by symmetry label. The base structure used in the calculations is Theory I of Table IV. Experimental values are given when available (Ref. 19).

k	Irrep	Frequencies (cm^{-1})	Expt.
Z	A_1	102, 189, 447, 831	
	B_1	292	
	E (2)	46, 151, 184, 270, 454	59, 168
X	A_1	66, 237, 285, 309, 486	72
	A_2	131, 233, 426	
	B_1	54, 321	
	B_2	99, 177, 337, 608, 672	
M	A_1	74, 452	
	A_2	412	
	B_1	138	
	B_2	247, 635, 716	
	E (2)	57, 203, 294, 398	
M'	A_1	67, 110, 272, 406, 415	
	A_2	152, 270, 401	
	B_1	57, 329	
	B_2	58, 188, 312, 579, 794	
R	A_1	90, 411	
	A_2	401	
	B_1	135	
	B_2	200, 626, 803	
	E (2)	65, 136, 322, 386	

estimate the degree of dependence of the phonon frequencies upon the details of the base structure used in the calculations ("Theory I" or "Theory II" above). Phonons at zone-boundary points are computed using the "Theory I" structure.

To test the convergence of our results with respect to the density of the k-point grid for BZ integrations, we recomputed the frequencies of z-polarized Γ modes using a (6,6,6) Monkhorst-Pack grid. The results, displayed in Table VII, indicate a high level of convergence.

As for the question of the existence of a phase transition at low temperature, we find that all the vibrational frequencies are real, as can be seen from the positive sign of all the mode force constants k. Thus there are no mechanical instabilities in the "bare" vibrational degrees of freedom, either at Γ or at the edges of the BZ. However, there still remains

TABLE VII. Test of the convergence of mode frequencies with k-point grid. (4,4,4) and (6,6,6) grids are used for the "Theory I" choice of Table IV. The frequencies (in cm^{-1}) are those of transverse z-polarized modes at Γ.

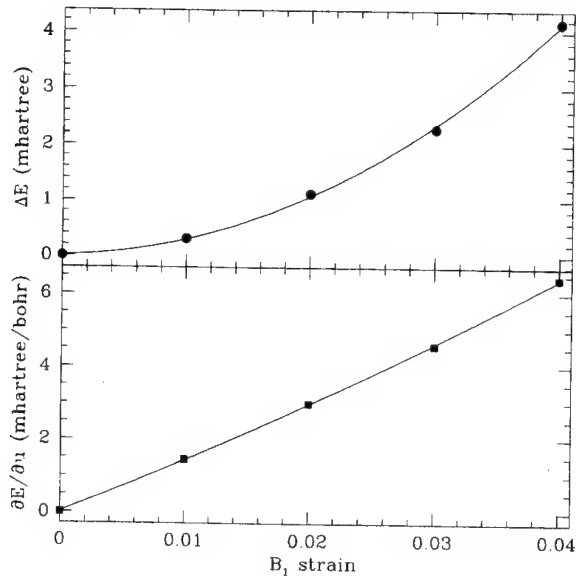| k-point grid	(4,4,4)	(6,6,6)
A_1(TO)	151	153
B_1	285	289
A_1(TO)	355	359
A_1(TO)	645	648

FIG. 3. Upper panel: Change in crystal energy (per cell) as a function of the orthorhombicity parameter t (B_1 strain). The curve is a fit to a parabola. Lower panel: Derivative of the crystal energy with respect to the B_1 normal mode amplitude at zero amplitude, as a function of B_1 strain. According to Eq. (5), it measures the degree of coupling between the normal mode and the strain.

the question of whether the linear coupling to strain degrees of freedom could result in any instability.

We deal first with the renormalization of the elastic constant corresponding to a B_1 orthorhombic strain. By applying pure B_1 strains of different magnitudes (for which we set $b - a \neq 0$ while keeping the sum $a + b$ constant) and computing the resulting values of the total energy, we obtain the data plotted in Fig. 3. A fit to a simple parabola is very good up to sizable strains. The elastic constant C [see Eq. (3)] turns out to be 5.0 hartree.[20] As mentioned above, we use the optimized structure ("Theory II") for this and the rest of the calculations involving elastic constants and strain-phonon couplings.

From the same set of calculations, but extracting this time the forces on the atoms and taking the scalar product (in configuration space) with the eigenvector of the B_1 mode, we obtain from Eq. (5) (see also Fig. 3) $\gamma = 0.15$ hartree/bohr. The force constant for the B_1 mode is 0.048 hartree/bohr^2, so the renormalized C is $C_{\text{eff}} = 4.5$ hartree. We see that even though there is a 10% change in the value of the elastic constant, the renormalization due to the coupling to the phonons is not enough to cause a B_1 instability of the tetragonal cell.

We performed a similar set of calculations for the analysis of the monoclinic distortion with E symmetry. The forces along the x axis appearing upon application of an η_{xz} strain translated into coupling constants of 0.17, 0.05, 0.06, and 0.00 hartree for the optical x-polarized E modes of respective force constants 0.014, 0.042, 0.077, and 0.155 hartree/bohr^2. The bare elastic constant for η_{xz} strain is 5.4 hartree. Adding up the contributions to the renormalization from the four modes we obtained an effective elastic constant C_{eff} of 3.3 hartree. In this case the renormalization amounts to 40%

of the bare value, but still is not enough to drive an E instability.

As discussed above, there is no linear coupling of B_2 orthorhombic strains to atomic displacements. The calculated elastic constant for this type of strain is positive (6.0 hartree), so there should be no instabilities of B_2 symmetry either.

Finally, recall that there is no first-order coupling of zone-boundary modes to homogeneous strain. Thus we need only check the bare force constants, which are all found to be positive (see Table VI). This means that we do not expect any mechanical instabilities associated with a cell doubling.

V. CONCLUSIONS

The low-temperature transition proposed by Kobayashi et al.[11] on the basis of x-ray and optical measurements is supposed to involve a slight orthorhombic distortion of the tetragonal phase, maintaining the orientation of the cell axes with no cell doubling. Our analysis of the energetics of B_1 distortions shows that a low-temperature transition of this kind is possible, in principle, but not likely in ferroelectric PbTiO$_3$. In this connection, it should be noted that, to our knowledge, the experimental observations of Ref. 11 have not been reproduced since 1983.

We also checked more generally for other kinds of low-temperature structural transitions. However, we find that all unit-cell-preserving distortions exhibit positive elastic constants, thus apparently ruling out transitions to a monoclinic structure (E distortions) or to a 45°-rotated orthorhombic structure (B_2 strain). Furthermore, we show that there are no mechanical instabilities associated with zone-boundary normal modes that could cause a phase transition with cell doubling.

Since we have not exhaustively explored the vibrational spectrum of the crystal, it is conceivable that a mechanical instability at a k point not on the BZ boundary may have been missed. However, our work shows fairly clearly that a simple transition is not likely in ferroelectric PbTiO$_3$ at low temperatures.

Note added in proof. After this paper had been submitted for publication, we learned of a set of high-resolution x-ray and neutron diffraction experiments on powder PbTiO$_3$ samples which appear to indicate that PbTiO$_3$ remains tetragonal down to 10 K [J. M. Kiat (private communication)].

APPENDIX

1. Renormalization of energy-surface coefficients

We show first how the linear coupling of u to t in the energy expansion of Eq. (3) implies a renormalization of C (or, equivalently, of k). After a transformation of the quadratic form to "principal axes" by a linear change of vari-

ables, the first partial derivatives of the energy will be zero. We can achieve the transformation implicitly by setting the derivative of E with respect to u to zero, and solving for u, to get $u = -\gamma t/k$. When this condition is inserted back into Eq. (3), we obtain an expression for E as a function of the free variable t,

$$E(t) = \frac{1}{2}\left(C - \frac{\gamma^2}{k}\right)t^2 = \frac{1}{2}C_{\mathrm{eff}}t^2, \qquad \text{(A1)}$$

from which it follows that the effective elastic constant is $C_{\mathrm{eff}} = C - \gamma^2/k$. (If instead u is chosen as a free variable, one obtains a renormalized spring constant $k_{\mathrm{eff}} = k - \gamma^2/C$. However, the physical mode frequency is not renormalized, because of the "infinite mass" associated with the strain degrees of freedom.)

In the case of the B_2 distortion with quadratic coupling, Eq. (4), one needs $\beta > 0$ and $\alpha > 0$ or else there would be unphysical divergences to $-\infty$ in the energy. But then, setting the u derivative of the energy to zero, one gets either $u = 0$ (trivial) or $u^2 = -(k + 2\gamma t^2)/4\alpha$ (meaningless since u would be imaginary). Thus there is no renormalization of the elastic constant.

2. Optimization of structural parameters

Using the symmetry constraints of the $4mm$ point group, one can write down the expression (to second order in the strain and atomic displacements) for the energy of a general tetragonal phase of that symmetry as

$$E = E_0 + E_{\mathrm{strain}} + E_{\mathrm{internal}} + E_{\mathrm{strain-ph}}, \qquad \text{(A2)}$$

where

$$E_{\mathrm{strain}} = \alpha_1 s + \beta_1 r + \alpha_2 s^2 + \beta_2 r^2 + \delta s r \qquad \text{(A3)}$$

is the part that depends only on the s and r strains,

$$E_{\mathrm{internal}} = \sum_{i=1}^{3} \tfrac{1}{2} k_i u_i^2 \qquad \text{(A4)}$$

is the change in energy due to internal atomic displacements compatible with the symmetry (and thus expanded as combinations of the three A_1 phonons polarized along the z axis), and

$$E_{\mathrm{strain-ph}} = \sum_{i=1}^{3} (\gamma_s^i u_i s + \gamma_r^i u_i r) \qquad \text{(A5)}$$

are the symmetry-allowed couplings of s and r to the A_1 phonons (both s and r transform according to A_1).

The 14 coefficients in this expansion are easily computed for a given base configuration. In our case, the starting point is a tetragonal cell with a and c given by experiment and the internal atomic positions along the z axis optimized theoretically to eliminate residual forces (column labeled "Theory I" in Table IV). Computed A_1 phonon frequencies directly give the force constants k_i, and the strain and strain-coupling coefficients are obtained in a manner analogous to that described in the main body of the paper. Once the quadratic form for E is known, it is a simple matter to find the structural parameters which correspond to the minimum energy (column labeled "Theory II" in Table IV). As is typical of first-principles calculations, the calculated lattice parameters are smaller than the experimental values by around 1%.

---

*Electronic address: wdpgaara@lg.ehu.es; FAX: +34-4-464-8500.

[1] For a good discussion of the experimental work on perovskites, see M.E. Lines and A.M. Glass, *Principles and Applications of Ferroelectric and Related Materials* (Clarendon, Oxford, 1977).

[2] R.E. Cohen and H. Krakauer, Phys. Rev. B **42**, 6416 (1990); Ferroelectrics **136**, 65 (1992); R.E. Cohen, Nature (London) **358**, 136 (1992).

[3] D.J. Singh and L.L. Boyer, Ferroelectrics **136**, 95 (1992).

[4] R.D. King-Smith and D. Vanderbilt, Phys. Rev. B **49**, 5828 (1994); Ferroelectrics **136**, 85 (1992).

[5] W. Zhong, D. Vanderbilt, and K.M. Rabe, Phys. Rev. Lett. **73**, 1861 (1994); Phys. Rev. B **52**, 6301 (1995).

[6] W. Zhong and D. Vanderbilt, Phys. Rev. Lett. **74**, 2587 (1995).

[7] K.M. Rabe and U.V. Waghmare, J. Phys. Chem. Solids (to be published).

[8] N. Sicron, B. Ravel, Y. Yacoby, E.A. Stern, F. Dogan, and J.J. Rehr, Phys. Rev. B **50**, 13 168 (1994).

[9] J. Kobayashi and R. Ueda, Phys. Rev. **99**, 1900 (1955); J. Kobayashi, S. Okamoto, and R. Ueda, Phys. Rev. **103**, 830 (1956).

[10] See, for example, S.A. Mabud and A.M. Glazer, J. Appl. Crystallogr. **12**, 49 (1979).

[11] J. Kobayashi, Y. Uesu, and Y. Sakemi, Phys. Rev. B **28**, 3866 (1983).

[12] Since the notation for irreducible representations at different points of the BZ is not standardized, we prefer to use the customary irrep labeling for point groups (A, B, E, etc.) and refer to specific representations by mentioning the k point explicitly.

[13] Note that some k points have the same irrep classification. In fact, whole lines of the BZ belong to the same "symmetry class." The term *Wintgen position* has been coined for such symmetry-equivalent points in reciprocal space, in analogy with the standard *Wyckoff positions* of the real-space description. See M.I. Aroyo and H. Wondratschek, Z. Kristallogr. **210**, 243 (1995).

[14] The crystal energy, being invariant against all the symmetry operations, must transform according to the identity (A_1) representation. It is a well-known result of group theory that the identity can always be obtained by the product of a given irrep with itself. For a discussion of the influence of these couplings in the elastic and piezoelectric response of a crystal, see P.B. Miller and J.D. Axe, Phys. Rev. **163**, 924 (1967).

[15] H.J. Monkhorst and J.D. Pack, Phys. Rev. B **13**, 5188 (1976).

[16] See for example, W. Zhong and D. Vanderbilt, Phys. Rev. Lett. **72**, 3618 (1994).

[17] For the purpose of discussing mechanical instabilities, one does not need to take into account the masses of the atoms; it suffices to analyze the eigenvectors and eigenvalues of the force-constant matrix. However, once this matrix is determined, it is straightforward to include the relevant mass factors to obtain the dynamical matrix and phonon frequencies (and to augment the dynamical matrix with the long-range Coulomb coupling terms to get the LO-TO splitting).

[18] The mode eigenvectors are not listed, but can be obtained from the authors upon request.

[19] J. D. Freire and R. S. Katiyar, Phys. Rev. B **37**, 2074 (1988).

[20] Our energies in Eqs. (3) and (4) are referred to a fixed cell vol- ume. It is customary to give elastic constants in units of energy/ volume; we are implicitly using units of energy/cell.

[21] F. Jona and G. Shirane, *Ferroelectric Crystals* (Dover, New York, 1993).

RAPID COMMUNICATIONS

Rapid Communications are intended for the accelerated publication of important new results and are therefore g̲ iv̲e̲n̲ to th̲ in̲ rev̲ie̲w̲ a̲r̲ both in the editorial office and in production. A Rapid Communication in **Physical Review B** *may be no longer th̲ n̲ fo̲ r̲ p̲r̲in̲t̲e̲ p̲a̲ r̲ and must be accompanied by an abstract. Page proofs are sent to authors.*

First-principles investigation of 180° domain walls in BaTiO$_3$

J. Padilla, W. Zhong, and David Vanderbilt

Department of Physics and Astronomy, Rutgers University, Piscataway, New Jersey 08855-084⁹

(Received 22 September 1995; revised manuscript received 21 December 1995)

We present a first-principles study of 180° ferroelectric domain walls in tetragonal barium titanate. The theory is based on an effective Hamiltonian that has previously been determined from first-principles ultrasoft-pseudopotential calculations. Statistical properties are investigated using Monte Carlo simulations. We compute the domain-wall energy, free energy, and thickness, analyze the behavior of the ferroelectric order parameter in the interior of the domain wall, and study its spatial fluctuations. An abrupt reversal of the polarization is found, unlike the gradual rotation typical of the ferromagnetic case.

The cubic perovskites are among the most important examples of ferroelectric materials.[1] Many undergo not just one, but a series, of structural phase transitions as the temperature is reduced. These transitions occur as a result of a delicate balance between long-range dipole-dipole interactions that favor the ferroelectric state, and short-range forces that favor the high-symmetry cubic perovskite phase. Because of the anomalously large Born effective charge of the atoms, the ferroelectric transitions in the perovskites are very sensitive to electrostatic boundary conditions.[2,3] As a consequence, domain structure plays an important role in the ferroelectric transitions, and a theoretical understanding of the domain walls is of great interest.

Theoretical investigation of ferroelectric domain walls has been much less extensive than for their ferromagnetic counterparts. The strong coupling of ferroelectricity to structural and elastic properties is problematic. Previous theoretical investigations have concentrated on a phenomenological level of description, using Landau theory to study domain-wall thickness and energy.[4,5] Simple microscopic models such as local-field theory have also been used to identify the domain-wall structure and character.[6] Due to the limited experimental data available, this empirical work has tended to be qualitative and oversimplified and has thus not been able to offer the accuracy needed for a deeper theoretical understanding.

In this paper, we undertake a first-principles study of ferroelectric domain walls in BaTiO$_3$. While several *ab initio* studies of bulk BaTiO$_3$ and related materials have appeared in the literature,[7–9] to our knowledge the present work is the first such study of the domain walls. Using an *ab initio* effective Hamiltonian developed previously to study the phase transitions of BaTiO$_3$,[7] we set up Monte Carlo (MC) simulations to investigate the structure and energetics of 180° domain walls of (100) orientation. In particular, the energy, free energy, and thickness of the wall are calculated. We also analyze the behavior of the ferroelectric order parameter in the interior of the domain wall and study the fluctuations in the domain-wall shape. Where we can compare with previous work, we find our results in general agreement with experimental[10–12] and theoretical reports.

Because only low-energy distortions are important to the structural properties, we work with an effective Hamiltonian written in terms of a reduced number of degrees of freedom.[7] The most important degrees of freedom included are the $3N$ "local-mode amplitudes" $u_{i\alpha}$ for site i and Cartesian direction α. A "site" is a primitive unit cell centered on a Ti atom, and the "local mode" on this site consists of displacements of the given Ti atom, its six nearest oxygen neighbors, and its eight nearest Ba neighbors, in such a way that a superposition of a uniform set of local-mode vectors $\mathbf{u}_i = \mathbf{e}$ (independent of i) generates the soft zone-center ferroelectric mode polarized along $\hat{e}$. We also include six degrees of freedom to represent homogeneous strain of the entire system and $3N$ displacement local-mode amplitudes $v_{i\alpha}$ that serve to introduce inhomogeneous strains. We thus reduce

be number of degrees of freedom per unit cell from 15 to 6, simplifying its expansion considerably.

Since the ferroelectric transition involves only small structural distortions, we represent the energy surface by a Taylor expansion around the high-symmetry cubic perovskite structure, including up to fourth-order anharmonic terms where appropriate. The energy consists of five parts: an on-site local-mode self-energy, a dipole-dipole interaction, a short-range interaction between local modes, an elastic energy, and a coupling between the elastic deformations and the local modes. The Hamiltonian is then specified by a set of expansion parameters, which are determined using highly accurate local-density approximation (LDA) calculations with Vanderbilt ultrasoft pseudopotentials.[13] The details of the Hamiltonian, the first-principles calculations, and the values of the expansion parameters have been reported elsewhere.[7] This scheme has been successfully applied to single-domain $BaTiO_3$ to predict the phase-transition sequence, transition temperatures, and other thermodynamic properties with good accuracy.

The phase-transition sequence for $BaTiO_3$ is cubic to tetragonal to orthorhombic to rhombohedral as temperature is reduced. We focus on the tetragonal phase, since it is the room-temperature phase, and the best studied experimentally. We adopt the convention that the polarization, and thus the tetragonal c axis, are along $\hat{z}$. In this phase, two kinds of domain walls, 90° and 180°, are possible.[14] The notation refers to the angle between polarization vectors in adjacent domains. We choose the 180° domain wall for this study because of preliminary indications of a simple structure and narrow width.[7] Because it is energetically unfavorable to form domain walls carrying net bound charge, 180° domain walls are restricted to lie parallel to the polarization. Earlier work has indicated that the 180° domain wall of (100) orientation has much lower energy than for other, e.g., (110), orientations.[6] Thus, we focus on the (100) domain wall, which we take to lie in the y-z plane.

Ideally, we would like to study a single 180° domain wall in isolation. In order to make the simulation tractable, we apply artificial periodic boundary conditions. (While a study of a finite sample would also be interesting, the presence of surfaces would greatly complicate the analysis.) We use a $4L \times L \times L$ supercell (typically $L = 10$) containing up and down domains alternating in the x direction. Thus, there are two 180° domain walls per supercell, with a spacing between walls of about 20 lattice constants. We find that this separation is more than enough to give converged results, based on tests of convergence with respect to L. In fact, previous work has indicated that the width of the 180° domain wall is very narrow, of the same order of magnitude as the lattice constant.[4,6,10] Thus, in retrospect this should not be surprising.

For a very narrow domain wall, our choice of local mode (Ti centered as opposed to Ba centered) may introduce some bias. The point is that the sharpest domain wall that can be constructed is one for which the local-mode vectors $\mathbf{u}_i$ are constant except for a sudden sign reversal from one plane of sites to the next. For the Ti centered choice of local modes, this represents a Ba-centered domain wall, for which the atomic displacements have odd symmetry across (and vanish on) the central Ba plane. Conversely, for a Ba-centered

choice of local mode, the sharpest domain wall is Ti centered, vanishing on a central plane of Ti atoms. In order to determine which of these scenarios is the more realistic, we constructed $4 \times 1 \times 1$ supercells (containing 20 atoms and 2 domain walls) corresponding to each of the above scenarios, using a mode amplitude taken from the average equilibrium structure of the MC simulations (very close to the experimental structure). We then performed LDA calculations to compare the energies of the two structures. We find the Ba-centered and Ti-centered walls constructed in this way have energies of 6.2 and 62.0 erg/cm^2, respectively. Thus, a sharp Ti-centered domain wall appears very unfavorable and it is clearly best to use a Ti-centered local mode as we have done. We note that the effective Hamiltonian reproduces the energy of this sharpest Ti-centered wall to within 1% of the LDA result (not surprisingly, since configurations of a similar kind were included in the fitting[7]).

We study the structure and energetics of the domain walls using Metropolis MC simulations.[15] The degrees of freedom are the vectors $\mathbf{u}_i$ and $\mathbf{v}_i$ for each site i of the $4L \times L \times L$ supercell, and the six homogeneous strain components. As mentioned above, the supercell is arranged to contain two domains, each roughly of size $2L \times L \times L$, with domain walls normal to $\hat{x}$ and with periodic boundary conditions. Since all energy contributions (except for the dipole-dipole coupling) are local, we choose the single-flip MC algorithm. We make a trial move of variables at one site, check acceptance, make the change if accepted, and go on to the next site. One Monte Carlo sweep (MCS) constitutes one entire pass through the system in this manner.

To generate a reasonable starting configuration for the $4L \times L \times L$ supercell, we equilibrate an $L \times L \times L$ supercell at a high temperature ($T > 400$ K) in the cubic phase and then cool it down slowly, allowing it to relax for 20 000 MCS's at each temperature step. We stop the cooling when the tetragonal phase is reached, in which the polarization vector averaged over the simulation cell points along one Cartesian axis. (As reported in Ref. 7, this phase corresponds to the temperature range from 230–290 K in our calculation, while the actual experimental range is 278–403 K.[16]) If the polarization is not along $+\hat{z}$, we rotate the structure to make it so. We then copy the structure four times along the x axis, with the polarization reversed to $-\hat{z}$ for two of them. The starting configuration thus contains two periodic 180° domain walls perpendicular to the (100) direction.

This structure is initially equilibrated for 2000 MCS's, in order to reach a good approximation to the "local equilibrium" associated with the presence of alternating domains. Thermodynamic averages are then constructed from runs of 40 000 MCS's. Of course the global equilibrium for our supercell would consist of a single-domain (bulk) structure; indeed, we find that fluctuations in the positions of the domain walls can occasionally cause two neighboring walls to touch, which leads rapidly to the mutual annihilation of the pair of walls. While this occurrence is fairly rare, we nevertheless decided to prevent it by fixing the z components of the $\mathbf{u}$ vectors in the central two layers in each domain during the simulations, thus providing "barriers" to the motion of the domain walls. Since the domain walls are typically far from these barriers and the constrained structure is very close to the bulk equilibrium, we think the effect on our results is
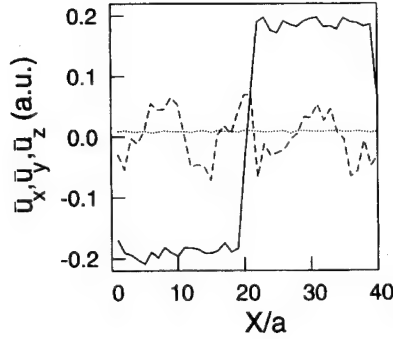
FIG. 1. Snapshot of the y-z layer-averaged polarization-vector components $\bar{u}_x$ (dotted line), $\bar{u}_y$ (dashed line), and $\bar{u}_z$ (solid line), as a function of x/a (a is the lattice constant), for the $40\times10\times10$ lattice at 260 K.
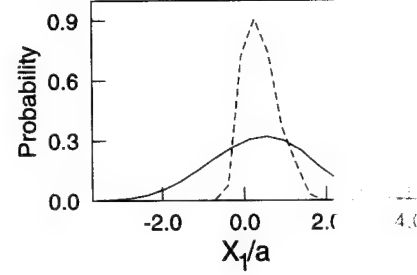

FIG. 2. Histograms of domain-wall positions for the $40\times10\times10$ lattice at 260 K. Solid line, histogram of $X_1(y,z,\tau)/a$ values (a is the lattice constant, τ labels a MCS); dashed line histogram of y-z planar-average values $\bar{X}_1(\tau)/a$.

negligible. Indeed, results taken from entirely unconstrained runs in which no annihilation event occurs appear very similar to those given below.

Figure 1 shows a snapshot of the polarization vector components averaged over y-z layers, $\bar{u}_x$, $\bar{u}_y$, and $\bar{u}_z$, as a function of x, for $L=10$. Several qualitative features are immediately apparent. First, the sharp reversal of u_z indicates that the domain boundary is indeed very sharp, its width being on the order of a lattice constant. Second, the other components u_x and u_y remain small throughout the whole supercell and their random fluctuations do not appear to be correlated with the domain-wall position. (The qualitative difference between the fluctuations of $\bar{u}_x$ and $\bar{u}_y$ with x is an artifact of the averaging and of the presence of strong longitudinal correlations.[17]) Thus, we find that the domain boundary entails a simple *reversal*, rather than a *rotation*, of the ferroelectric order parameter.

These behaviors are to be contrasted with the case of ferromagnetic domain walls, where the magnetization vector typically rotates gradually (on the atomic scale), keeping a roughly constant magnitude. This difference in behavior can probably be attributed largely to the much stronger strain coupling in the ferroelectric case. For our $BaTiO_3$ geometry, for example, the entire sample, including the interface, develops a tetragonal strain along $\hat{z}$, imposed by the presence of domains polarized along $\pm\hat{z}$. This gives rise to a strong anisotropy which will tend to keep the ferroelectric order parameter from developing components along x or y in the interface region. Thus, instead of rotating, the polarization simply decreases in magnitude and reverses as we pass through the domain wall. This absence of rotation of the polarization has been experimentally verified for the case of the 90° domain wall in $BaTiO_3$.[18]

We now turn to a quantitative analysis of our simulation results, focusing on the domain-wall width, smoothness, and energy. We first estimate the domain-wall thickness t as follows. For a string of sites along x at a given value of (y,z) and on a given MCS, we identify the pair of sites between which u_z changes sign. We then define t via the linear extrapolation $t/a = 2u^{\text{spont}}/\Delta u_z$, where a is the lattice constant, u^{spont} is the spontaneous polarization deep in a domain, and Δu_z is the change of u_z between the two interface sites. Finally, we average over (y,z) points and over MCS's to get

an average value of t. The value of t estimated in this way is 1.4 unit cells, or 5.6 Å. This is in reasonable agreement with empirical theoretical estimates of 6.7 Å (Ref. 5) and experiments which place an estimated upper bound of 50 Å.[10]

To analyze the smoothness of the domain wall, we Fourier transform the polarization u_z as a function of the x coordinate for each (y,z) point and retain only the first three terms in the expansion. This is an effective way to smooth the data while keeping the most useful information. The positions of the two domain walls in the supercell, denoted by X_1 and X_2, are identified with the values of x at which the Fourier-smoothed u_z changes sign. In this way we obtain $X_1(y,z,\tau)$ and $X_2(y,z,\tau)$, where τ labels the MCS.

In Fig. 2, we show the probability distribution of X_1 for $L=10$ and for a run of 40 000 MCS's at 260 K. The solid line is a histogram of the values of $X_1(y,z,\tau)$, while the dashed line is a histogram of y-z planar averages $\bar{X}_1(\tau)$. A comparison of the two curves shows that the spatial fluctuations of the domain-wall position are much smaller than its ensemble fluctuations. From the solid line, we see that the X_1 values have a typical standard deviation of between one and two lattice constants. Other runs indicate that this result is not very sensitive to system size. So, we can conclude that the domain walls are relatively smooth. We can further separate the contributions to these fluctuations coming from the y and z directions. It is found that the fluctuations along the z direction (i.e., along the polar direction) are about 40% smaller than along the y direction. The sign of this result was to be expected, since the shape of the domain wall should be such as to minimize the surface charge $\Delta\mathbf{P}\cdot\mathbf{n}$ that develops on it. Here, $\Delta\mathbf{P}$ is the change of the polarization vector across the domain wall and $\mathbf{n}$ is the unit vector normal to the wall.

Finally, we turn to an estimate of the domain-wall formation energy. Because of the periodic boundary conditions imposed on our system, there are no surfaces to give rise to a depolarization energy. Thus, the domain-wall energy E_w can be calculated from the difference between the energy of the $4L\times L\times L$ supercell with and without domain walls. This difference is small, but because the correlation time of the system (far from the transition) is quite short (20 MCS's), a sufficiently long simulation is capable of reducing the statistical errors in E_w to an acceptable level. The calculated domain-wall energies are shown in Table I. The reported values have a statistical uncertainty of about 4%. Simulations

domain-wall energies E_w and free energies ... simulation cell size L and temperature T. Sta- ... about 4% for E_w and 10% for F_w.

		E_w (erg/cm^2)	F_w (erg/cm^2)
		15.8	4.6
		17.1	4.0
		15.6	5.0
		17.0	4.4

for two lattice sizes and temperatures are reported. We can see that our results are well converged with respect to system size. Because of the large increase of the correlation time near the transitions, it has proven difficult to give accurate values for E_w at other temperatures.

Our calculated value of $E_w = 16$ erg/cm^2 for the domain-wall energy is, however, probably not the proper quantity to compare with experimentally derived values. Instead, we should compute a *free energy*, F_w, which includes entropic contributions from fluctuations of the ferroelectric order parameter in the vicinity of the domain wall. A glance at Fig. 1, which shows considerable fluctuations, suggests that such contributions are likely to be important.

We have estimated the domain-wall free energies F_w using an adiabatic switching technique, as follows. First, we start with an equilibrated $4L \times L \times L$ supercell containing two domain walls, and for which the z components of the u vectors in the central two layers in each domain are constrained to preset values, as before. We slowly reverse the values of the constraint variables in the center of one of the domains over the course of a 20 000-MCS simulation, making a small change in the constraint variables every 10 MCS's, and compute the total work done on the constraint variables. If the simulation succeeds in removing the two domain walls adiabatically, we can equate the work done to twice the domain-wall free energy F_w. By comparing runs of from 20 000 to 30 000 MCS's, we find differences in computed F_w values of only about 10%, which suggests that the switching is indeed adiabatic. The resulting computed values of F_w are about 4–5 erg/cm^2, or about 3–4 times smaller than the E_w values (and slightly smaller than the 6.2 erg/cm^2 reported above for the energy of the ideal Ba-centered wall).

Our result is consistent with previously published estimates of the "energy" of the (100) 180° domain wall, although such previous values are rather scattered and inconclusive. Previous experimental results of 10 and 3 erg/cm^2 (close to the phase transition) were given by Merz[11] and Fousek and Safrankova,[12] respectively. On the theoretical side, Bulaevskii[5] reported a value of 10.5 erg/cm^2 using a continuum Landau p^6 model, while Lawless[6] calculated an energy of 1.52 erg/cm^2 based on a microscopic phenomenological model. (Since the above estimates involve use of empirical models fit to finite-temperature data, the "energy" values are probably best interpreted as free energies.)

This investigation has opened several avenues for further study. One important goal is to apply the model to more realistic geometries that include surfaces; after all, in real samples the domain structure generally arises because of the depolarization energy associated with surfaces. A natural first step would be to consider a slab geometry, to make contact with experimental thin-film studies. This would require first-principles calculations of very thin slabs ($\sim$3–5 unit cells thick) to determine the necessary modifications to the effective Hamiltonian at the surface, followed by Monte Carlo simulations on thicker slabs containing ferroelectric domains. We are now beginning to undertake first-principles calculations of the type needed. Other interesting avenues would be to study other types of domain walls [e.g., (110) 180° or 90° domain walls] in tetragonal BaTiO$_3$ and to consider other phases of BaTiO$_3$ or other perovskite materials.

In summary, we have studied the properties of 180° domain walls in BaTiO$_3$ using a first-principles based approach, by applying Monte Carlo simulations to a microscopic effective Hamiltonian that was fitted to *ab initio* total-energy calculations. The simulations were carried out in the middle of the temperature region of the tetragonal phase, relatively far from the C-T and T-O transitions. We confirm that the domain walls are atomically thin and that the order parameter does not rotate within the wall. We quantify the width, smoothness, and energetics of these domain walls. Our theoretical values of the wall width and free energy are in reasonable agreement with previously reported values, where available.

[1] M. E. Lines and A. M. Glass, *Principles and Applications of Ferroelectrics and Related Materials* (Clarendon, Oxford, 1977).

[2] R. Resta, M. Posternak, and A. Baldereschi, Phys. Rev. Lett. **70**, 1010 (1993).

[3] W. Zhong, R. D. King-Smith, and D. Vanderbilt, Phys. Rev. Lett. **72**, 3618 (1994).

[4] V. A. Zhirnov, Sov. Phys. JETP **35**, 822 (1959).

[5] L. N. Bulaevskii, Sov. Phys. Solid State **5**, 2329 (1964).

[6] W. N. Lawless, Phys. Rev. **175**, 619 (1968).

[7] W. Zhong, D. Vanderbilt, and K. M. Rabe, Phys. Rev. Lett. **73**, 1861 (1994); Phys. Rev. B **52**, 6301 (1995).

[8] R. E. Cohen and H. Krakauer, Phys. Rev. B **42**, 6416 (1990); Ferroelectrics **136**, 65 (1992); R. E. Cohen, Nature **358**, 136 (1992).

[9] D. J. Singh, Ferroelectrics **164**, 143 (1995).

[10] M. Tanaka and G. Honjo, J. Phys. Soc. Jpn. **19**, 954 (1964).

[11] W. J. Merz, Phys. Rev. **95**, 690 (1954).

[12] J. Fousek and M. Safrankova, Jpn. J. Appl. Phys. **4**, 403 (1965).

[13] D. Vanderbilt, Phys. Rev. B **41**, 7892 (1990).

[14] J. Fousek and V. Janovec, J. Appl. Phys. **40**, 135 (1969).

[15] *The Monte Carlo Method in Condensed Matter Physics*, edited by K. Binder (Springer-Verlag, Berlin, 1992).

[16] T. Mitsui *et al.*, in *Ferroelectrics and Related Substances. Oxides*, edited by O. Madelung, Landolt-Börnstein, New Series, Group 3, Vol. 16, Pt. a (Springer-Verlag, Berlin, 1981).

[17] The strong dipolar interactions give rise to a strong longitudinal correlation of the $\mathbf{u}_i$. That is, u_x is strongly correlated along x, while u_y is strongly correlated along y. The averages over y-z planes involved in the definition of $\bar{u}$ has amplified the fluctuations of $\bar{u}_y$ while suppressing those of $\bar{u}$.

[18] S. I. Yakunin, V. V. Shakmanov, G. V. Spivak, and N. M. Vasil'eva, Sov. Phys. Solid State **14**, 310 (1972).

Ab initio study of BaTiO$_3$ surfaces

J. Padilla and David Vanderbilt

Department of Physics and Astronomy, Rutgers University, Piscataway, New Jersey 08855-0849

(Received 18 February 1997)

We have carried out first-principles total-energy calculations of (001) surfaces of the tetragonal and cubic phases of BaTiO$_3$. Both BaO-terminated (type I) and TiO$_2$-terminated (type II) surfaces are considered, and the atomic configurations have been fully relaxed. We found no deep-gap surface states for any of the surfaces, in agreement with previous theoretical studies. However, the gap is reduced for the type-II surface, especially in the cubic phase. The surface relaxation energies are found to be substantial, i.e., many times larger than the bulk ferroelectric well depth. Nevertheless, the influence of the surface upon the ferroelectric order parameter is modest; we find only a small enhancement of the ferroelectricity near the surface. [S0163-1829(97)04927-8]

I. INTRODUCTION

Recently there has been a surge of interest in the application of first-principles density-functional calculations to the study of the rich phenomenology of the perovskite oxides, with special attention to ferroelectric (FE) properties.[1] From these investigations, it has been found that the FE instability in these materials occurs as a result of a delicate balance between long-range Coulomb interactions that favor the FE state, and short-range forces that favor the cubic perovskite phase.[2,3] Moreover, the ferroelectric properties are well known to degrade in thin-film[4] and particulate[5] geometries, suggesting that the FE state could be very sensitive to surface effects.

The cubic perovskites have the chemical formula ABO$_3$. For II-IV perovskites (e.g., BaTiO$_3$) A is a divalent cation and B is a tetravalent transition metal, while for I-V perovskites (e.g., KNbO$_3$) they are mono- and pentavalent, respectively. The (001) and (111) surfaces of these materials have been the most investigated experimentally.[6] There are two possible terminations of the (001) surface: the AO-terminated surface (type-I) and the BO$_2$-terminated surface (type-II). In II-IV perovskites, the AO and BO$_2$ layers are charge neutral, so that both type-I and type-II surfaces are nonpolar. For I-V perovskites, the corresponding surfaces are instead polar. As for (111) surfaces, the atomic planes in this direction are of the form AO$_3$ and B, and are charged in either case, so that the (111) surfaces are polar. Since polar surfaces are expected to be relatively unstable, we have chosen to focus here on the (001) surfaces of a II-IV perovskite, BaTiO$_3$.

Due in part to the catalytic properties of SrTiO$_3$ and BaTiO$_3$,[7] there has been a continuous interest in the surface properties of these materials. There have been previous theoretical studies especially for the case of the paraelectric SrTiO$_3$ surface, but also for BaTiO$_3$. Wolfram and co-workers,[8] using a linear combination of atomic orbitals cluster method, predicted mid-gap surface states for SrTiO$_3$, in disagreement with experimental investigations.[9,10] Only after *ad hoc* modifications to this model could the experimental results be accounted for.[11] Tsukada *et al.*[12] employed the DV $X\alpha$ cluster method to study SrTiO$_3$ surfaces, finding no mid-gap surface states.

However, cluster methods are not very suitable for high-accuracy calculations of relaxations and electronic states on infinite surfaces, underlining the need for the application of more accurate, self-consistent techniques. While such techniques have recently yielded a great deal of insight into bulk perovskites,[3,13–15] their application to the study of perovskite surfaces has not been very extensive. In fact, we only know of two such studies. Cohen[16,17] presented linearized augmented plane wave calculations performed for slabs of tetragonal BaTiO$_3$ with (001) and (111) surfaces, using both symmetrical and asymmetrical terminations. Although some relaxations were allowed, the atomic positions were not fully relaxed. Kimura *et al.*[18] used a plane-wave ultrasoft-pseudopotential[19] approach (as in the present work) to study the TiO$_2$-terminated (001) surface of SrTiO$_3$, with and without oxygen vacancies at the surface. Again, the slabs were not fully relaxed.

In contrast, we study here symmetrically terminated type-I and type-II surfaces of tetragonal and cubic BaTiO$_3$ (001) for which the coordinates have been fully relaxed by minimizing the total energy. This allows us to study the influence of surface relaxation effects upon the FE distortion. For the tetragonal phase, we consider only the case of the tetragonal c axis (i.e., polarization) parallel to the surface. (Polarization normal to the surface is suppressed by depolarization fields,[3] at least for clean surfaces.) We employed the ultrasoft-pseudopotential method[19] within the local-density approximation (LDA). This technique permits us to calculate the Hellmann-Feynman forces on each atom, making it possible to find the relaxed structure much more efficiently than for methods that compute only total energies.

Experimental studies of perovskites surfaces are complicated by the presence of surface defects,[20] making it difficult to verify the surface stoichiometry. Therefore, most experimental investigations have not been very conclusive. On SrTiO$_3$ surfaces, the situation is better: the surface relaxations have been studied,[21,22] and (as mentioned above) the absence of midgap surface state has been demonstrated.[9] For BaTiO$_3$ surfaces, the experimental reports seem less conclusive. For example, evidence both for[23] and against[24] surface gap states in this material have been published.

Regarding the degradation of FE properties for thin films and small particles as mentioned above,[4,5] there does not

seem to be any consensus about the origin of these effects. One possibility is that it is completely intrinsic, i.e., that the very presence of the surface suppresses the FE order in the vicinity of the surface. However, there are many other possible causes. These include the effects of surface-induced strain; perturbations of the chemical composition near the surface related to the presence of impurities, oxygen vacancies, or other defects; and the depolarization fields for the case of particles (or for films with polarization perpendicular to the surface). Here, we take a modest step in the direction of sorting out these effects by characterizing the purely intrinsic coupling between the presence of a surface and the FE order, for the case of a free (vacuum-terminated) surface. As we shall see, we find the surface relaxation energies are large compared to FE distortion energies. However, we find very little effect for type-I surfaces, and only a modest enhancement of the FE order at type-II surfaces, with indications that it will be mainly confined to just the first few atomic layers near the surface. Thus, it appears unlikely that intrinsic surface effects are responsible for the degradation of FE order in thin films and particles.

The remainder of the paper is divided as follows. In Sec. II, we describe the technical aspects of our first-principles calculations. In Sec. III, we report the results of our simulations. Finally, the main conclusions of the paper are reviewed in Sec. IV.

II. THEORETICAL DETAILS

We carried out self-consistent total-energy pseudopotential calculations in which the electronic wave functions were expanded in a plane-wave basis. The core electrons were frozen, and for a given geometry of the ions, the valence electron wave functions were obtained by minimizing the Kohn-Sham total-energy functional using a conjugate-gradient technique.[25] The exchange-correlation potential was treated with the LDA approximation in the Ceperley-Alder form.[26] The forces on each ion were relaxed to less than 0.02 eV/Å using a modified Broyden scheme.[27]

The Vanderbilt ultrasoft-pseudopotential scheme[19] was employed. In this approach, the the norm-conservation constraint is relaxed, allowing one to treat rather localized orbitals with a modest plane-wave cutoff. The pseudopotentials for Ti, Ba, and O are identical to those used previously[25] in a study of bulk perovskites. The semicore Ti $3s$ and $3p$ states and Ba $5s$ and $5p$ states are included as valence levels. A plane-wave cutoff of 25 Ry has been used throughout; previous work has shown that the results are well converged at this cutoff.

$BaTiO_3$ undergoes a series of phase transitions as the temperature is reduced, from the high-symmetry paraelectric cubic phase to FE phases with tetragonal, orthorhombic, and rhombohedral unit cells. The tetragonal structure is of special interest, since it is the room-temperature structure. In this paper, we are thus primarily interested in the surfaces of the room-temperature tetragonal phase, although for comparison we also present results for surface of the elevated-temperature cubic phase. Ideally one would like to do this by carrying out *ab initio* molecular-dynamics simulations at the temperatures at which these phases are stable, but unfortunately this is not practical. Instead, we carry out ground-state

TABLE I. Computed and experimental values of structural parameters for $BaTiO_3$ in bulk cubic and tetragonal phases. a and c are lattice constants; δ_x are displacements associated with the FE instability as a fraction of c. O_I is the oxygen lying along $\hat{x}$ from the Ti atom, and $\delta_x(O_{II}) = \delta_x(O_{III})$ by symmetry.

Phase	Parameter	Expt. [a]	Theory [b]
cubic	a (Å)	3.996	3.948
tetrag.	a (Å)	3.992	3.938
	c (Å)	4.036	3.993
	$\delta_x(Ti)$	0.0135	0.0128
	$\delta_x(O_I)$	-0.0150	-0.0150
	$\delta_x(O_{III})$	-0.0240	-0.0232

[a]Reference 30.
[b]Reference 25.

($T=0$) calculations, but subject to the imposition of the appropriate (tetragonal or cubic) symmetry in order to prevent the system from adopting the true rhombohedral $T=0$ structure. This is clearly an approximation, but we think it is a reasonable one. The computed ground-state structural parameters for the cubic and tetragonal bulk phases are given in Table I, together with experimental values for comparison. (Again, the theoretical values are for $T=0$ structures with the appropriate symmetry imposed.) The computed lattice constants a and c for the cubic and tetragonal phases are $1-2\%$ smaller than the experimental ones; this underestimation is typical of LDA calculations. We use the theoretical unit cell parameters in all calculations presented here.

As shown schematically in Fig. 1, the periodic slab corresponding to the type-I (BaO terminated) surface contains 17 atoms (four BaO layers and three TiO_2 layers). Similarly, the type-II (TiO_2 terminated) slab contains 18 atoms (four TiO_2 layers and three BaO layers). For both cases, the slabs were thus three lattice constants thick; the vacuum region was two lattice constants thick. The z axis is taken as normal to the surface, and the M_z mirror symmetry with respect to
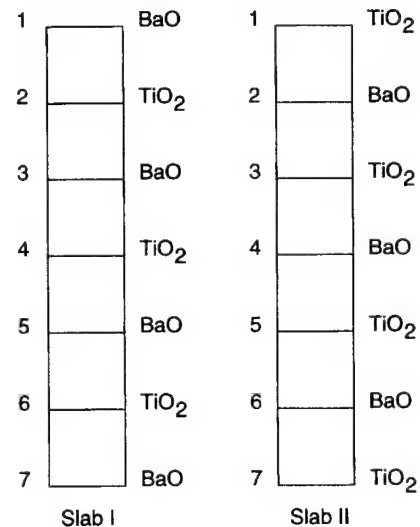

FIG. 1. Schematic arrangement of layers in the BaO-terminated (slab I) and TiO_2-terminated (slab II) supercell geometries. Layers 1 and 7 are surface layers.

the central layer was imposed in all cases. For surfaces of the cubic phase, mirror symmetries M_x and M_y were also preserved. For the tetragonal case, the polarization vector and thus the tetragonal c axis were chosen to lie along x (parallel to the surface); here, M_y symmetry was respected but M_x symmetry was allowed to be broken. As mentioned earlier, the choice of polarization parallel to the surface is motivated by the fact that no charge accumulation results at the surface for this case, and thus no depolarization fields appear.[3] The case of the tetragonal c-axis lying perpendicular to the surface was considered by Cohen.[16,17]

The calculations were done using a (4,4,2) Monkhorst-Pack mesh.[28] This corresponds to three and four k points in the irreducible Brillouin zone (BZ) for the cubic and tetragonal supercells, respectively. To test the convergence with respect to k point sampling, we repeated the calculation for a (6,6,2) mesh, finding that the surface energy differed by less than 3%. When the vacuum region was enlarged to three layers in thickness, the surface energy changed by less than 4%.

In order to study the relative stability of the two kinds of surface terminations, it is necessary to introduced appropriate chemical potentials.[29] To simplify our analysis, we think of the independent constituents of the slab as being BaO and TiO₂ units. We define E_f to be the *formation energy* needed to make bulk BaTiO₃ from BaO and TiO₂, per formula unit. Thus we have

$$-E_f = E_{BaTiO_3} - E_{BaO} - E_{TiO_2} \qquad (1)$$

(by convention, $E_f > 0$). E_{BaTiO_3}, E_{BaO}, and E_{TiO_2} are the energies of the bulk crystals, per formula unit, measured relative to isolated ion cores and electrons. BaTiO₃ was calculated in the relaxed tetragonal structure, and TiO₂ in the relaxed rutile structure.

Now, we define the two chemical potentials μ_{TiO_2} and μ_{BaO} in such a way that $\mu_{TiO_2} = 0$ corresponds to a system in contact with a reservoir of bulk crystalline TiO₂, and similarly for μ_{BaO}. Furthermore, if we insist that the system is always in equilibrium with a reservoir of bulk BaTiO₃, then we have that

$$\mu_{BaO} + \mu_{TiO_2} = -E_f. \qquad (2)$$

Thus, only one of μ_{BaO} and μ_{TiO_2} is an independent degree of freedom. We arbitrarily chose μ_{TiO_2} as the independent one. Then μ_{TiO_2} can be allowed to vary over the range

$$-E_f \leqslant \mu_{TiO_2} \leqslant 0. \qquad (3)$$

At $\mu_{TiO_2} = -E_f$ the system is in equilibrium with BaO and BaTiO₃, and for lower values bulk crystallites of BaO can precipitate. Similarly, above $\mu_{TiO_2} = 0$, bulk crystallites of TiO₂ can form.

Therefore, the grand thermodynamic potential per surface unit cell is given by

$$F = \tfrac{1}{2} [E_{slab} - N_{TiO_2}(\mu_{TiO_2} + E_{TiO_2}) - N_{BaO}(\mu_{BaO} + E_{BaO})] \qquad (4)$$

(the factor of 1/2 appearing because the cell contains two surfaces), where E_{slab} is the energy of the relaxed slab in the tetragonal phase. For example, for the type-I slab, one has

TABLE II. Atomic relaxations of the Ba-terminated surface (slab I) in the cubic (C) and tetragonal (T) phases, given as a fraction of a or c, with respect to ideal positions (i.e., for δ_x, with respect to the M_x symmetry plane).

Atom	δ_z (C)	δ_x (T)	δ_z (T)
Ba(1)	-0.0279	-0.0142	-0.0277
O$_{III}$(1)	-0.0140	-0.0298	-0.0126
Ti(2)	0.0092	-0.0086	0.0098
O$_I$(2)	0.0048	-0.0297	0.0059
O$_{II}$(2)	0.0048	-0.0240	0.0045
Ba(3)	-0.0053	-0.0149	-0.0059
O$_{III}$(3)	-0.0026	-0.0280	-0.0020
Ti(4)	0	-0.0034	0
O$_I$(4)	0	-0.0340	0
O$_{II}$(4)	0	-0.0256	0

$N_{TiO_2} = 3$ and $N_{BaO} = 4$. Equations (2) and (4) give F as a function of μ_{TiO_2} over the range of Eq. (3).

III. RESULTS AND DISCUSSIONS

A. Structural relaxations

First we determined the equilibrium atomic positions for our two types of slabs in the two phases. For the cubic surface, we started from the ideal structure and relaxed. For the tetragonal surface, we obtained a starting guess by superposing the z displacements from the relaxed cubic surface with x displacements from the bulk tetragonal structure.[25] The relaxed geometries are summarized in Tables II and III. In these tables, the atoms are listed in the same order as shown in Fig. 1. (Coordinates are only listed for atoms in the top half of the slab, $z \geqslant 0$; the others are determined by the M_z mirror symmetry.) By symmetry, there are no forces along $\hat{x}$ or $\hat{y}$ for the cubic surfaces, and no forces along $\hat{y}$ for the tetragonal surface. Also due to the crystal termination, the two O atoms associated with the Ti atom (O$_I$ and O$_{II}$) are no longer equivalent in the tetragonal phase (I, II, and III indicate the O that is connected to Ti by a bond along x, y, and z, respectively).

From Tables II and III, we can see that the largest relaxations are on the surface-layer atoms, as expected. They are

TABLE III. Atomic relaxations of the Ti-terminated surface (slab II) in the cubic (C) and tetragonal (T) phases, given as a fraction of a or c, with respect to ideal positions.

Atom	δ_z (C)	δ_x (T)	δ_z (T)
Ti(1)	-0.0389	0.0005	-0.0331
O$_I$(1)	-0.0163	-0.0499	-0.0100
O$_{II}$(1)	-0.0163	-0.0366	-0.0071
Ba(2)	0.0131	-0.0148	0.0186
O$_{III}$(2)	-0.0062	-0.0292	-0.0023
Ti(3)	-0.0075	0.0019	-0.0058
O$_I$(3)	-0.0035	-0.0372	-0.0022
O$_{II}$(3)	-0.0035	-0.0278	-0.0023
Ba(4)	0	-0.0111	0
O$_{III}$(4)	0	-0.0276	0

TABLE IV. Calculated interlayer relaxation (β) and rumpling (η) for the surface layer of the relaxed slabs in the cubic (C) and tetragonal (T) phases (Å).

Slab	β (C)	η (C)	β (T)	η (T)
Slab I	-0.08	0.03	-0.08	0.03
Slab II	-0.11	0.05	-0.08	0.05

TABLE V. Calculated FE distortion δ_{FE} of the relaxed slabs, for each layer (units of lattice constant). The last line gives theoretical bulk values for reference.

Layer	Slab I δ_{FE}(BaO)	Slab I δ_{FE}(TiO$_2$)	Slab II δ_{FE}(BaO)	Slab II δ_{FE}(TiO$_2$)
1	0.0156			0.0438
2		0.0182	0.0144	
3	0.0131			0.0344
4		0.0332	0.0165	
Bulk	0.0232	0.0278	0.0232	0.0278

especially important for the Ti atoms in the Ti-terminated slabs, in the direction perpendicular to the surface. This can plausibly be explained by noting that for bulk BaTiO$_3$, the filled Ba levels lie well below the oxygen-$2p$ valence bands and do not hybridize strongly, so that the Ba atom is a relative spectator in the bonding.[24] In the tetragonal case, we can also see that the asymmetry between the two O atoms lying in a common surface plane is significant. Bond lengths on the surface change by less than 1.5% with respect to the bulk in the same phase (the latter values are the experimental ones, taken from Mitsui et al.[29]).

We computed the average displacements β and the rumpling η for the surface layers; the results are given in Table IV. To fix the notation, let $\delta z(M)$ be the change in the surface-layer metal-atom z position relative to the ideal unrelaxed structure, and $\delta z(O)$ be the same for the surface oxygens (defined as $[\delta z(O_I) + \delta z(O_{II})]/2$ for a TiO$_2$ layer). Then the surface relaxation parameter β is defined as $[\delta z(M) + \delta z(O)]/2$, and the rumpling η is defined as $[\delta z(O) - \delta z(M)]/2$. We find that the surface layers contract substantially inwards towards the bulk, with both the metal and oxygen ions relaxing in the same direction.

Cohen[17] has computed the surface relaxations of surface relaxations of BaTiO$_3$ slabs, both in the cubic phase and with FE polarization normal to the surface.[2] Thus, direct comparison with our work is only possible for the cubic phase. In this case, Cohen calculated the relaxation only for the case of an asymmetrically terminated slab (BaO on one surface and TiO$_2$ on the other). Thus, detailed quantitative agreement is probably not expected, because (i) only the surface-layer atoms were relaxed in Cohen's calculation, and (ii) the asymmetric termination introduces a small electric field which may have influenced the relaxations. Nevertheless, we do find qualitative agreement. Cohen finds that the Ba and O atoms relax inwards by 0.043 and 0.033 lattice constants, respectively, on the type-I surface; and the Ti and O atoms relax inwards by 0.048 and 0.027, respectively, on the type-II surface. These can be compared with the first two entries in the δ_z(C) column of Tables II and III. It can be seen that Cohen's values are 20–100 % larger in magnitude, but of the same sign, as those that we calculate. Similarly, Cohen computes values of -0.15 Å for the average surface layer relaxation, to be compared with the values given by us in the column β(C) of Table IV. The rumpling computed by Cohen is also of the same sign, but different in detail, as that calculated by us.

We are not aware of any experimental surface structure determination for BaTiO$_3$ with which we can compare our theory. However, we note that one low-energy electron diffraction I-V study of the corresponding SrTiO$_3$ surfaces[21] comes to an opposite conclusion, suggesting an outward relaxation of the surface layer on the order of 0.1 Å, while a second such study[22] is in less obvious contradiction with our results. Clearly, there is a need for a parallel calculation on the SrTiO$_3$ surface in order to determine whether the experimental interpretation[21,22] should be reexamined.

B. Influence of the surface upon ferroelectricity

It is important to understand whether the presence of the surface has a strong effect upon the near-surface ferroelectricity. For example, is the FE order enhanced near the surface, or is it suppressed? As we shall see in Sec. III C, the energy scale of the surface relaxations is larger than the energy scale of the FE double-well potential. Thus, a strong effect is possible. To analyze whether it really occurs, we computed an average FE distortion δ_{FE} for each layer of the slab. We define $\delta_{FE} = \delta_x(Ba) - \delta_x(O_{III})$ for a BaO plane, and $\delta_{FE} = \delta_x(Ti) - [\delta_x(O_I) + \delta_x(O_{II})]/2$ for a TiO$_2$ plane.

Our calculated values for δ_{FE} are given in Table V; the last row of the table gives the bulk values for reference. No clear pattern appears to emerge from these results, although we do note a moderate enhancement of the FE instability in the TiO$_2$ layers for the TiO$_2$-terminated surface.

The lack of a clear trend for the influence of surface effects upon the FE distortion can be understood, at least in part, by noting that the FE mode is only one of three zone-center modes having the same symmetry.[24] The FE mode is distinguished as the one that is soft ($\omega^2 < 0$) in the cubic structure, but there is no particular reason why the surface relaxation should couple more strongly to this mode than to the others. We have estimated how strongly the surface relaxations are related to each of the zone-center modes by the following procedure. We calculate the forces for a tetragonal surface slab in which the displacements in the x direction are those of the ideal bulk tetragonal structure, while the displacements in the z direction are taken from the relaxed cubic surface. The forces in the x direction are then projected onto each of the zone-center bulk modes polarized along x. That is, the force for each type of atom (e.g., O$_{III}$) was summed over all such atoms in the slab, and the inner product was then taken between the resulting force vector and the bulk mode eigenvectors.

We found that the FE mode accounts for only about 31% and 26% of this force vector for the type-I and type-II slabs, respectively. Thus, it seems that the distortions induced by the presence of the surface are mostly of non-FE character, helping to explain why the FE order is not as strongly affected as might have been guessed.
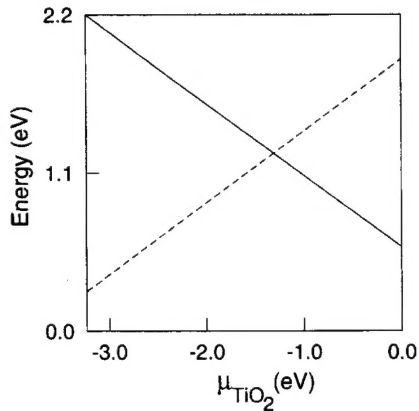
FIG. 2. Grand thermodynamic potential F as a function of the chemical potential μ_{TiO_2}, for the two types of surfaces, in the tetragonal phase. Dashed and solid lines correspond to type-I (BaO-terminated) and type-II (TiO$_2$-terminated) surfaces, respectively.

C. Surface energies

We turn now to a study of the surface energetics. Following the approach outlined in Sec. II, we calculated the grand thermodynamic potential F for our two types of surface as a function of TiO$_2$ chemical potential. The results are shown in Fig. 2. In order to attain optimal cancellation of errors, E_{TiO_2} and E_{BaO} were calculated within the LDA using the same pseudopotentials, and with the same 25 Ry energy cutoff. A similar k-point sampling as for the surfaces of BaTiO$_3$ was also employed. In this way, we obtained $E_f = 3.23$ eV for the formation energy of BaTiO$_3$. This quantity fixes the range of physical values of μ_{TiO_2}; the left and right boundaries of Fig. 2 correspond to a system in thermodynamic contact with bulk BaO and bulk TiO$_2$ respectively. It can be seen that both surfaces have a comparable range of thermodynamic stability, indicating that either type-I or type-II surfaces could be formed depending on whether growth occurs in Ba-rich or Ti-rich conditions.

The *average* surface energy E_{surf} (i.e., the average of F for the two kind of surfaces) is independent of μ_{TiO_2}. Therefore, this quantity is suitable for comparisons. For the cubic phase, we estimated E_{surf} for the (001) surfaces to be 1.241 eV per surface unit cell (1265 erg/cm^2); and for the tetragonal phase, it was estimated to be 1.237 eV per surface unit cell (1260 erg/cm^2). The value of the average E_{surf} calculated in Ref. 17 for the symmetrically terminated cubic (001) surfaces is 920 erg/cm^2. As pointed out in that paper, the large value of E_{surf} may help explain why BaTiO$_3$ does not cleave easily, but fractures instead.

In order to compute the surface relaxation energy E_{relax}, we computed the average surface energy E_{unrel} for the *unrelaxed* cubic slabs (i.e., atoms in the ideal cubic perovskite positions), using the same k-point sampling as for the relaxed systems. We obtained $E_{unrel} = 1.358$ eV. Thus, the relaxations account for 0.127 eV of the surface energy per surface unit cell (or about 130 erg/cm^2).

Note that E_{relax} is many times larger than the bulk ferroelectric well depth, estimated to be of the order of 0.03 eV. This would indicate that the surface is capable of acting as a strong perturbation on the FE order. As explained in Sec.
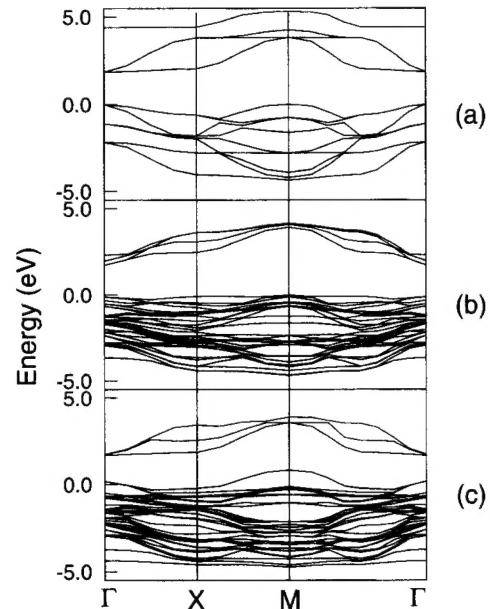

FIG. 3. Calculated band structures for BaTiO$_3$ in the cubic phase. (a) Surface-projected bulk band structure. (b) BaO-terminated surface (slab I). (c) TiO$_2$-terminated surface (slab II). The zero of energy corresponds to the bulk valence-band maximum. Only the lowest few conduction bands are shown.

III B, however, the actual effect is more modest than one would guess based on energetic considerations alone.

D. Surface band structure

As previously done by Cohen,[17] we have carried out LDA calculations of the surface electronic structure for our various surface slabs. While the LDA is well known to be quantitatively unreliable as regards excitation properties such as band gaps, we believe that the results presented here are nevertheless likely to be qualitatively correct. The bulk band gap in our calculation is 1.8 eV, to be compared with the experimental value of 3.2 eV; this level of disagreement is typical for the LDA.

Figure 3 shows the calculated LDA band structure for cubic bulk BaTiO$_3$ projected onto the surface BZ, and the surface band structures for the Ba- and Ti-terminated relaxed surfaces in the cubic phase. (The zero of energy for each surface slab was established by aligning the Ba or Ti semicore s states in the interior layers of the slab with those of the bulk.) Plots for the tetragonal surfaces would look similar, except that the tendency for states to intrude into the gap is stronger for the cubic case. This can be seen in Table VI, where we list the calculated band gaps for both cubic and

TABLE VI. Calculated band gaps for relaxed cubic (C) and tetragonal (T) surface slabs (eV).

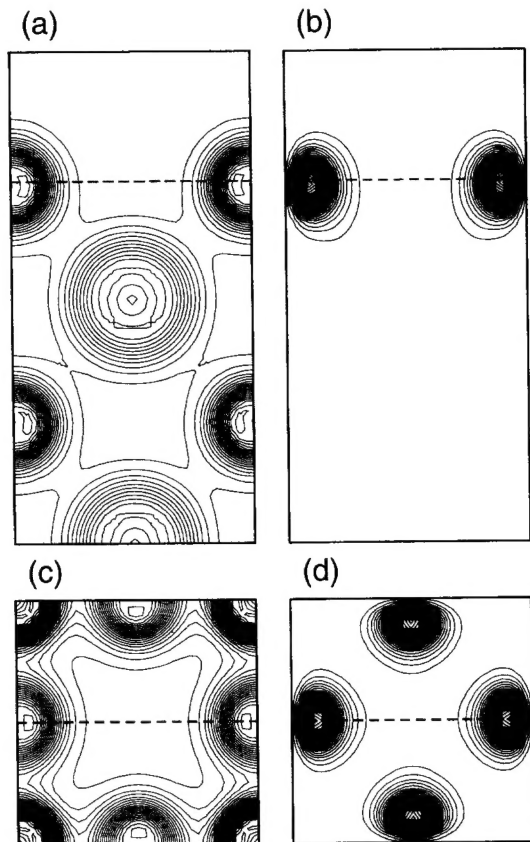| Slab	C	T
Slab I	1.80	2.01
Slab II	0.84	1.18
Bulk	1.79	1.80

FIG. 4. Charge-density plots for relaxed Ti-terminated surface (slab II) in the cubic phase. Panels (a-b) show cuts on a vertical x-z BaO plane; panels (c-d) show cuts on the x-y surface TiO_2 plane. Total charge density, (a) and (c); charge density of highest occupied state at M point of the surface BZ, (b) and (d).

tetragonal slabs. We therefore tend to focus on the cubic surfaces, where it is easier to identify and characterize the surface states.

First, we can see that on the Ba-terminated (type-I) surface, the gap is not reduced and there are no deep gap states. On the Ti-terminated (type-II) surface, however, the gap is reduced, especially for the cubic case. As can be seen from Fig. 3c, there is a tendency for valence-band states to intrude upwards into the lower part of the band gap for this surface, especially near the M point of the surface BZ. (Qualitatively similar results can be seen in Fig. 3 of Ref. 17.) However, the conduction band does not change much with respect to the bulk. Moreover, we do not see signs of any true "deep-gap" states lying near the center of the gap. As noted earlier, the existence of such deep-gap states remains controversial experimentally. Our work suggests that if gap states do exist in connection with nondefective (001) surfaces, it is likely that they would be found in the lower part of the band gap, and that this would be indicative of exposed TiO_2 (as opposed to BaO) surface planes.

Figure 4 illustrates the character of the valence-band state at the M point that is intruding into the lower part of the gap. The total charge density is also shown for reference. It can be seen that this state is composed of O $2p$ lone-pair orbitals lying in the surface plane. Further inspection shows that the

special feature of this state is that the wave function has four nodal planes $[(100), (110), (010),$ and $(\bar{1}10)]$ intersecting at the Ti sites. This precludes the presence of any Ti $3d$ character (in fact, any Ti character of angular momentum $l<4$). In the bulk, the oxygen $2p$ orbitals are all hybridized with Ti $3d$ orbitals to some extent, and the level repulsion associated with this hybridization pushes the energy location of the valence-band states downward in energy. Thus, the energy of the unhybridized O $2p$ lone-pair surface state at the M point is left intruding into the lower part of the gap.

This insight makes it possible to understand other features of the surface band structures as well. For example, on the BaO-terminated surface, every surface oxygen atom is directly above a Ti atom, and is strongly hybridized to it. Thus, there is no such tendency for the formation of surface states in this case. Returning to the TiO_2-terminated surface, there seems to be a weaker tendency for the intrusion of a valence-band derived surface state at Γ. This state turns out to have a single nodal plane passing through the Ti site, so that hybridization with Ti $3d$ orbitals is only weakly allowed (by the breaking of M_z mirror symmetry across the surface plane).

We expect that these results would remain qualitatively valid for other II-VI perovskites such as $SrTiO_3$ or $PbZrO_3$. For I-V perovskites such as $KNbO_3$ and $LiTaO_3$, however, the (001) surface is nonstoichiometric, and the surface electronic structure would be expected to be quite different.

IV. SUMMARY

In summary, we have carried out LDA density-functional calculations of BaO- and TiO_2-terminated (001) surfaces for cubic and tetragonal phases of $BaTiO_3$. By minimizing the forces on the ions, we obtained the relaxed ionic structures. As would have been expected from the bulk electronic levels of $BaTiO_3$, the most important relaxations occur for the TiO_2-terminated surfaces. There appears to be a modest tendency for the surface relaxations to enhance the FE distortion on that surface, although the situation is complicated by the fact that the relaxations excite modes other than the soft zone-center one.

The free energies for the different surfaces were calculated as a function of the TiO_2 chemical potential. In particular, the average surface energy was found to be about 1260 erg/cm^2. The surface relaxation energies were found to be around 10% of the total surface energy.

In accord with previous theoretical reports, no mid-gap surface levels are found. But for the TiO_2-terminated surfaces, there is a substantial reduction of the bulk gap, especially for the cubic-phase surface. This reduction results from the intrusion of states of valence-band character into the lower part of the band gap, especially near the M point of the surface BZ.

ACKNOWLEDGMENTS

[1] M.E. Lines and A.M. Glass, *Principles and Applications of Ferroelectrics and Related Materials* (Clarendon Press, Oxford, 1977); F. Jona and G. Shirane, *Ferroelectric Crystals* (Dover Publications, New York, 1993).

[2] R. Resta, M. Posternak, and A. Baldereschi, Phys. Rev. Lett. **70**, 1010 (1993).

[3] W. Zhong, R.D. King-Smith, and D. Vanderbilt, Phys. Rev. Lett. **72**, 3618 (1994).

[4] F. Tsai and J.M. Cowley, Appl. Phys. Lett. **65**, 1906 (1994).

[5] J.C. Niepce, *Surface and Interfaces of Ceramic Materials,* edited by L.C. Dufour (Kluwer, New York, 1989), p. 521.

[6] V.E. Henrich and P.A. Cox, *The Surface Science of Metal Oxides* (Cambridge University Press, New York, 1994).

[7] M. Tomkiewicz and H. Fay, Appl. Phys. **18**, 1 (1979).

[8] T. Wolfram, E.A. Kraut, and F.J. Morin, Phys. Rev. B **7**, 1677 (1973).

[9] R.A. Powell and W.F. Spicer, Phys. Rev. B **13**, 2601 (1976).

[10] V.E. Henrich, G. Dresselhaus, and H.J. Zeiger, Bull. Am. Phys. Soc. **22**, 364 (1977).

[11] S. Ellialtioglu, T. Wolfram, and V.E. Henrich, Solid State Commun. **27**, 321 (1978).

[12] M. Tsukada, C. Satoko, and H. Adachi, J. Phys. Soc. Jpn. **48**, 200 (1980).

[13] W. Zhong, D. Vanderbilt, and K.M. Rabe, Phys. Rev. Lett **73**, 1861 (1994); Phys. Rev. B **52**, 6301 (1995).

[14] R.E. Cohen and H. Krakauer, Phys. Rev. B **42**, 6416 (1990); Ferroelectrics **136**, 65 (1992); R.E. Cohen, Nature (London) **358**, 136 (1992).

[15] D.J. Singh, Ferroelectrics **164**, 143 (1995).

[16] R.E. Cohen, J. Phys. Chem. Solids **57**, 1393 (1996).

[17] R.E. Cohen, Ferroelectrics (to be published).

[18] S. Kimura *et al.*, Phys. Rev. B **51**, 11 049 (1995).

[19] D. Vanderbilt, Phys. Rev. B **41**, 7892 (1990).

[20] B. Cord and R. Courths, Surf. Sci. **152/153**, 1141 (1985).

[21] T. Hikita, T. Hanada, and M. Kudo, Surf. Sci. **287/288**, 377 (1993).

[22] N. Bickel *et al.*, Vacuum **41**, 46 (1990); Phys. Rev. Lett. **62**, 2009 (1989).

[23] S. Robey, Ferroelectric (to be published).

[24] S.M. Mukhopadhyay and T.C.S. Chen, J. Mater. Res. **10**, 1502 (1995).

[25] R.D. King-Smith and D. Vanderbilt, Phys. Rev. B **49**, 5828 (1994).

[26] D.M. Ceperley and B.J. Alder, Phys. Rev. Lett. **45**, 566 (1980).

[27] D. Vanderbilt and S.G. Louie, Phys. Rev. B **30**, 6118 (1984).

[28] H.J. Monkhorst and J.D. Pack, Phys. Rev. B **13**, 5188 (1976).

[29] G.-X. Qian, R.M. Martin, and D.J. Chadi, Phys. Rev. B **38**, 7649 (1988).

[30] T. Mitsui *et al.*, in *Ferroelectrics and Related Substances. Oxides. Oxide,* edited by K.-H. Hellwege and O. Madelung, Landolt-Börnstein, New Series, Group III, Vol. 16, pt. a (Springer-Verlag, Berlin, 1981).